

SELF-ASSEMBLY OF ANISOTROPIC NANOSTRUCTURES

by

Youngsoo Jung

ME, University of Nevada, Reno, USA, 2010

ME, Inha University, South Korea, 2008

BE, Inha University, South Korea, 2006

Submitted to the Graduate Faculty of
The Swanson School of Engineering in partial fulfillment
of the requirements for the degree of
Doctor of Philosophy

University of Pittsburgh

2014

UNIVERSITY OF PITTSBURGH
SWANSON SCHOOL OF ENGINEERING

This dissertation was presented

by

Youngsoo Jung

It was defended on

June 25th, 2014

and approved by

Jung-Kun Lee, Ph.D., Associate Professor, Department of Mechanical Engineering and
Materials Science

John A. Barnard, Ph. D., Professor, Department of Mechanical Engineering and Materials
Science

Ian Nettleship, Ph.D., Associate Professor, Department of Mechanical Engineering and
Materials Science

Youngjae Chun, Ph.D., Assistant Professor, Department of Industrial Engineering

Dissertation Director: Jung-Kun Lee, Ph.D., Associate Professor,
Department of Mechanical Engineering and Materials Science

Copyright © by Youngsoo Jung

2014

SELF-ASSEMBLY OF ANISOTROPIC NANOSTRUCTURES

Youngsoo Jung, Ph.D.

University of Pittsburgh, 2014

Controlling and manipulating the physical and chemical intrinsic properties of nanomaterials has been a fascinating issue in chemistry and materials science. Two central geometric variables, size and shape, strongly affect the intrinsic properties of nanomaterials. Specifically, the shape of nanocrystals plays a pivotal role in the determining intrinsic properties, including optical, electronic, magnetic, and catalytic behavior. Since nanocrystals with tailored geometries possess unique shape dependent behaviors, considerable efforts to develop shape controlled inorganic materials and to investigate their shape anisotropic effects on functional properties are currently being undertaken. This dissertation will introduce specific shape anisotropic behavior of the shape modified particles achieved through two different synthetic routes: i) structural modification of shape anisotropic particles and ii) 3-dimensional self-assembly via microwave-assisted solvothermal reactions. Each topic section will systematically provide an approach on enhancing each specific intrinsic property originating from self-assembly of anisotropic nanostructure and will discuss the fundamentals behind these phenomena.

TABLE OF CONTENTS

ACKNOWLEDGEMENT	XV
1.0 INTRODUCTION	1
1.1 THE SHAPE CONTROL OF NANOMATERIALS	3
1.1.1 General concept: shape control of nanomaterials	3
1.1.2 Overview of proposed mechanisms for anisotropic growth	5
1.2 MODIFICATION OF SHAPE ANISOTROPIC PARTICLES	17
1.2.1 General concept of nanoparticles embedded clay composite	17
1.2.2 Structural features of clay particles	18
1.2.3 The nanoparticles embedded clay hybrid composite	20
1.3 MAGNETORHEOLOGY CONTROL	22
1.3.1 General concept and characteristics of magnetorheological fluids	22
1.3.2 MR fluids	24
1.3.3 Field induced particle interactions and structure formation	25
1.4 RESEARCH MOTIVATION	29
1.4.1 Fluid rheology control via nanoparticle assembly with 2D clay particle .	29
1.4.2 Facile synthetic route of 3D structured particles via MW irradiation	31
2.0 MODIFICATION OF NANOPARTICLE ASSEMBLY WITH 2D PLATE	33
2.1 INTRODUCTION	33

2.1.1	Surface charge modification of 2D clay particle.....	33
2.1.2	Magnetorheological property of iron oxide decorated clay fluid.....	35
2.2	BACKGROUND	37
2.2.1	Structure of 2D plate clay and interparticle-association	37
2.2.2	Estimating rheological properties of fluid systems.....	40
2.3	EMBEDDED CLAY HYBRID NANOPARTICLES	46
2.3.1	Sample preparation	46
2.3.2	Characterization	48
2.3.3	Results and discussions	49
2.4	IRON OXIDE NANOPARTICLES DECORATED CLAY	66
2.4.1	Sample preparation	66
2.4.2	Results and discussions	68
3.0	MIROWAVE SYNTHESIS OF 3D STRUCTURES PARTICLE	76
3.1	INTRODUCTION	76
3.2	BACKGROUND	79
3.2.1	Principles of microwave irradiation	79
3.2.2	Effects of microwave heating in chemical reaction	84
3.2.3	Mechanisms of shape anisotropic particle growth	92
3.3	3D SELF-ASSEMBLY OF FLOWER-LIKE PARTICLES	105
3.3.1	Sample preparation and characterization.....	105
3.3.2	Results and discussions	107
3.4	MAGNETORHEOLOGY OF MR FLUID WITH FLS IRON OXIDE	122
3.4.1	Results and discussions	122

4.0	CONCLUSIONS AND FUTURE WORK	130
4.1	CONCLUSIONS	130
4.2	FUTURE WORK.....	133
	BIBLIOGRAPHY	137

LIST OF TABLES

Table 2-1 Variation of yield stress of the prepared fluid samples with respect to change of pH.	60
Table 3-1 Loss factors ($\tan\delta$) and dielectric constant of different solvents [229]	84
Table 3-2 Characteristics of microwave and conventional heating [231]	86
Table 3-3 Rheological parameters of FLS- Fe_3O_4 and spherical $\gamma\text{-Fe}_2\text{O}_3$ particle fluids at a constant magnetic field of 0.38 T	129

LIST OF FIGURES

Figure 1-1 Representative examples of various shaped inorganic nanomaterials in TEM observation; (a) 0-D polyhedron, (b) 1-D rods, (c) 2-D plate, and (d) 3-D hierarchical structure [16-19].....	4
Figure 1-2 Microscopic interfacial processes supporting crystal growth [39]. Process (i) reversible adspecies deposition (adsorption). Process (ii) adspecies surface migration.....	7
Figure 1-3 Growth mechanisms for pseudo-1D crystalline morphologies: (a) VLS mechanism proposed by Wagner and Ellis for growth under CVD conditions, (b) SLS mechanism proposed by Buhro and co-workers for analogous growth from solution [44].....	8
Figure 1-4 Various organizing schemes for self-construction of nano structures by oriented attachment.....	9
Figure 1-5 Surface energy of ZnS nanocrystals. The (001) face has the highest surface energy. Since the growth rate is proportional to the surface energy, the fastest growth occurs along the [001] direction [54] (G = growth rate, S = surface energy)	12
Figure 1-6 Surface modulation effects induced by the selective adhesion of surfactant: a) anisotropic rod [57], and b) disc growth [58]	14
Figure 1-7 Temperature-mediated crystalline-phase control of a,b) MnS and c,d) CdS nanocrystals [61,62,65,66].....	16
Figure 1-8 Schematic representation of the porous structured nanoparticles embedded clay hybrid composite.....	18
Figure 1-9 Schematic illustration representing structure of montmorillonite clay	19
Figure 1-10 XRD patterns of pristine clay and nanoparticles (NPs)-intercalated clay [74]. Increase in c-spacing by intercalation of NPs into clay results in XRD peak shift to lower angle	20

Figure 1-11 Schematic illustration of nanoparticles intercalation process	21
Figure 1-12 The surface changes of a MR fluid under applied magnetic field: (a) liquid phase under no magnetic field, (b) solid phase under an applied magnetic field, (c) alignment of the magnetic particles along the direction of a magnetic field [76] ...	23
Figure 2-1 Schematic illustration of clay structure	38
Figure 2-2 Association modes of individual clay platelet	40
Figure 2-3 Consistency curves for four different types of flow systems	41
Figure 2-4 Measurements of viscoelastic behavior in small amplitude oscillatory method	45
Figure 2-5 Low-angle X-ray diffraction patterns of pristine Na ⁺ -montmorillonite and hybrid particles; (a) pristine clay, (b) as-grown ICH, and (c) as-grown ASCH particles.....	50
Figure 2-6 High-angle X-ray diffraction patterns of pristine Na ⁺ -montmorillonite and hybrid particles: (a) pristine clay, (b) 450 °C annealed ICH, and (c) 400 °C annealed ASCH particles (H: Hematite)	51
Figure 2-7 SEM micrographs of freeze-dried solids of (a) 5B, (b) 5B-0.5ASCH, and (c) 5B-0.5ICH	52
Figure 2-8 Viscosity vs. shear rate curves of the fluid samples at 25 oC under atmospheric pressure.....	53
Figure 2-9 Schematic illustration of acquisition of yield point using the tangent in the linear-elastic deformation	54
Figure 2-10 Storage modulus vs. strain amplitude curves of the fluid samples at fixed frequency (10 rad/s).....	55
Figure 2-11 Change in storage (G') and loss modulus (G'') of fluid samples as a function of the shear stress; (a) 5B, (b) 5B-0.5ASCH, and (c) 5B-0.5ICH suspensions	56
Figure 2-12 (a) 5B, 5B-0.5ASCH, 5B-0.5ICH at 25 °C, atmospheric pressure, (b) 5B, 5B-0.5ASCH, 5B-0.5ICH at 25 °C, 100 bar, (c) 5B, at 20-200 °C, 100 bar, (d) 5B-0.5ASCH, at 20-200 °C, 100 bar, (e) 5B-5ASCH, at 20-200 °C, 100 bar, (f) 5B-0.5ICH at 20-200 °C, 100 bar.....	58
Figure 2-13 Viscosity vs. shear rate curves of the fluid samples with respect to change of pH: (a) 5B, (b) 5B-0.5ASCH, (c) 5B-5ASCH, and (c) 5B-0.5ICH suspensions.....	60

Figure 2-14 Variation of zeta potential of bentonite, ASCH, and ICH particles as a function of pH.....	63
Figure 2-15 Schematic illustration of (a) particles association in 5B-0.5ASCH and (b) “house-of-card” structure in 5B-0.5ICH fluid	65
Figure 2-16 XRD patterns of (a) pristine clay, (b) CTAB-treated clay (organo clay) and (c) CTAB-treated clay and OA-treated iron oxide nanoparticles. The inset shows XRD pattern in the range of 30-40 (2theta) from (c)	69
Figure 2-17 TEM images and particle size distribution: (a) OA-treated iron oxide, (b) size distribution of OA-treated iron oxide, (c) pristine clay, and (d) OA-treated iron oxide and CTAB-treated clay.....	70
Figure 2-18 Sample image for fluids containing modified particles in mineral oil and their microstructure from the TEM.....	71
Figure 2-19 Magnetic property of heterostructured sample of OA-treated iron-oxide and CTAB-treated clay	72
Figure 2-20 (a) Viscosity and (b) shear stress vs. shear rate of fluid containing of (●) OA-treated iron-oxide and CTAB treated clay, (■) CTAB-treated clay and (▲) OA-treated iron oxide nanoparticles	74
Figure 2-21 Storage modulus vs. strain amplitude of the fluids containing OA-treated iron oxide nanoparticles (b) OA-treated iron oxide and CTAB-treated clay with different magnetic field. Solid symbol represent storage modulus and open symbol are loss modulus.....	75
Figure 3-1 Commercially available microwave reactor for the chemical synthesis (Mars, CEM)	80
Figure 3-2 Two main heating mechanisms under microwave irradiation: (a) dipolar polarization, (b) ionic conduction mechanism [226].....	82
Figure 3-3 Temperature profile after 60s heated by (a) microwave irradiation, (b) conventional oil-bath treatment [232].....	86
Figure 3-4 a),b) TEM images of Ce ³⁺ /Tb ³⁺ co-doped LaF ₃ fabricated under MW and oil-bath heating, respectively [233]. c),d) Proposed mechanisms for the nucleation stage of the Ce ³⁺ /Tb ³⁺ co-doped LaF ₃ under MW irradiation and oil-bath heating, respectively.....	88

Figure 3-5 a)/d), b)/e), c)/f) TEM images showing the morphology evolution of α -Fe ₂ O ₃ nanostructures achieved by the MW reaction [239,240] at 220 °C after (a,d) 10 s, (b,e) 50 s, and (c,f) 5 min, g) Schematic representation of α -Fe ₂ O ₃ nanoring formation	90
Figure 3-6 TEM images of BiPO ₄ obtained after sonication for (a) 2, (b) 5, (c) 8, (d) 15, (e) 25, and (f) 60 min [254]	93
Figure 3-7 TEM images showing different stages of growth for Te nanorods after an aging time of (a) 0 min, (b) 20min, (c) 15 h, and (d) 20 h, (e) HRTEM images of an individual Te nanorod, (f) SAED pattern of nanorod, which is indexed to be the [110] of t-Te [258]	95
Figure 3-8 Schematic illustration of a plausible mechanism for the formation of Te nanorods via a solid-solution-solid transformation and a surfactant-assisted growth mechanism [258]	95
Figure 3-9 Schematic illustrations of linear complexes that were formed between ethylene glycol (a) Ti, (b) In, and (c) Pb cations [260].....	96
Figure 3-10 1D rod versus 2D disc growth; (a) preferential growth along one direction (z-axis), (b) growth along two directions (xy-plane)	98
Figure 3-11 (a) Cu ₂ S discs [261] and (b) NiS nanoprism [262] through solvent less thermolysis of metal-alkanethiol complexes. Insets show HRTEM images of the Cu ₂ S discs and NiS prisms.....	98
Figure 3-12 TEM images of BiOCl obtained after sonication for (a) 2, (b) 5, (c) 8, (d) 15, (e) 25, and (f) 60 min. The coarse fringes of lamellae became smooth, indicating an aggregation and crystallization process [254]	99
Figure 3-13 SEM images of SnO ₂ nanoflowers: panels (a) and (b) are low-magnification SEM images of the nanoflowers, (c) TEM image of SnO ₂ nanowires: the inset is the corresponding SAED pattern, (d) local high magnification SEM image of panel (b) [265].....	101
Figure 3-14 (a) SEM image of the flower-like α -Fe ₂ O ₃ , (b) high magnification SEM image of a single nanoflower, (c) TEM image of a single nanoflower (inset: SAD patterns), (d) TEM image of a single petal (inset: SAD pattern), (e) HRTEM image of a single petal [266]	102
Figure 3-15 Time-dependent experiments for the precursor after reacting for (a) 1h, (b) 2h, (c) 3h, (d) 6h, and (e) schematic illustration for the nanoflower formation [266]	103

Figure 3-16 FESEM images of the as-prepared β -FeSe by microwave irradiation for 1 h. (a) Low magnification image, (b) high magnification image (inset: a much higher magnification image) [269]	104
Figure 3-17 XRD patterns of fabricated FLS particles; (a) as-grown FLS-precursor, (b) FLS- Fe_3O_4 , and (c) FLS-Fe particles. (■ : α -FeOOH)	108
Figure 3-18 Raman spectra of (a) as-grown FLS particles and (b) N_2 -annealed FLS particles (■ : α -FeOOH, □ : α - Fe_2O_3)	109
Figure 3-19 FTIR spectra of the as-grown FLS particles	110
Figure 3-20 SEM and TEM micrographs of as-grown FLS-precursor particles. (Inset: selected area diffraction (SAD) patterns)	112
Figure 3-21 SEM and TEM micrographs of (a), (b), (c) FLS- Fe_3O_4 and (d), (e) FLS-Fe particles. (Inset: selected area diffraction (SAD) patterns of FLS- Fe_3O_4 particles)	115
Figure 3-22 SEM micrographs of the as-grown particles obtained at different reaction temperatures: (a) 120 °C, (b) 150 °C, (c) 180 °C, and (d) 210 °C.....	115
Figure 3-23 Change in the morphology of the reaction products as a function of the pressure: (a) ~0.2 MPa, (b) 0.3 ~ 1 MPa, and (c) 1MPa.....	116
Figure 3-24 SEM micrographs of as-grown particles as a function of reaction time; (a) 20 s, (b) 60 s, (c) 2 min, and (d) 5 min (a scale bar in the inset is 1 μm)	118
Figure 3-25 Nitrogen adsorption-desorption isotherms and pore size distribution curves of (a) as-grown FLS-precursor, (b) FLS- Fe_3O_4 , and (c) FLS-Fe particles. (Inset: pore size distribution curve).....	120
Figure 3-26 Concentration of residual sulfur ions as a function of reaction time	121
Figure 3-27 M-H curves of FLS- Fe_3O_4 particles (inset: hysteresis loop of FLS- Fe_3O_4).....	123
Figure 3-28 (a) M-H curves of FLS- Fe_3O_4 particles, and (b) storage modulus vs. strain amplitude curves of the fluids containing different amount of FLS- Fe_3O_4 particles when the magnetic field of 0.38 T is applied	124
Figure 3-29 (a) Storage modulus vs. strain amplitude curves of the fluids containing 10 wt% FLS- Fe_3O_4 particles under magnetic field (0-0.38 T), (b) a change in the storage modulus of the fluids containing 10 wt% FLS- Fe_3O_4 or spherical γ - Fe_2O_3 particles	126

Figure 3-30 (a) Storage (G') and Loss (G'') modulus for FLS- Fe_3O_4 ferrofluid and spherical $\gamma\text{-Fe}_2\text{O}_3$ at 0.38 T, (b) Scheme for increasing stress to break the rows of aligned particles by the rugged surface of FLS- Fe_3O_4 128

Figure 4-1 (a) Viscosity vs. shear rate curve of normal liquid electrolyte and nanoclay added electrolyte, and (b) storage modulus vs. strain amplitude curve at a fixed angular frequency of 10rad/s as a function of clay content 134

Figure 4-2 Schematic illustration representing proposed mechanism on the Grotthuss like charge transport 136

ACKNOWLEDGEMENT

This work was supported by National Science Foundation (Grant No. CBET-1235979 and CMMI-1333182)

This work could not have been completed without lots of help and encouragement from many people. I would like to express my sincere appreciation and acknowledgement during this incredible journey.

First and foremost, I will be forever grateful to my advisor, Prof. Jung-Kun Lee, for his invaluable guidance and encouragement throughout the whole period of my PhD study, as well as for the opportunity to work for him. His unparalleled dedication and insight were truly instrumental to the progress of the research. Needless to say, without his mentoring and continuous support, it is impossible to finish my PhD study. And, with no hesitation, I can say it was very lucky that I had Prof. Lee as my PhD advisor. He was not only superb guide, but also great guardian.

I would also like to convey my gratitude to my other committee members, Prof. John A. Barnard, Prof. Ian Nettleship, and Prof. Youngjae Chun. Prof. Barnard was always approachable and I could have a lot of pleasant conversation with him. I assure that he might have excellent power to make other people delightful. In addition to being my PhD committee member, Prof. Nettleship also served a role as a committee for my PhD qualifying exam. His decisive way of

dealing with questions has always been a source of inspiration. I would like express a special acknowledgement to Prof. Chun. As a mentor, as a helper, and as a friend, he is literally great person, and we have built a very close personal relationship. I am so happy to know and put him on a list of my personal network.

I am very delighted to have former/current members of this high-powered group: Dr. Mengjin Yang, Dr. You-Hwan Son, Dr. Bo Ding, Po-Shun, Salim, Ryan, Jianan, and Xiye. I would especially thank former members, Mengjin, You-Hwan, and Bo for their countless efforts to help Prof. Lee well set up this laboratory. Based upon a solid foundation and lively working environment that they established, my researches could be going smooth. Thanks also should go to this group's past/current undergraduate researchers for their contribution to research project as well as making the group more energetic: Travis, Derrick, David, Eric, Erica, Thomas, Colin, Matt, Mike, and Joel.

Special thanks must go to Albert Stewart, who has been retired two years ago. I will never forget his kind words that he told me with a warm smile, "It's alright, no worries. This is why you are here and you learn." These simple sentences have tremendously influenced on my mind when to interact with other people.

I would also like to take this opportunity to thank my friends: Barry's family (Matt&Stephanie, William&Sue), Partib, Andrea&Nick, Lui, Konstantin, Mike Whiston, Mike Durka, Austin, Rig, Kai, Nate, Innam, Sang Hyun, Sungjae, Daeho. Special thanks have to go to my best friend Matt Barry. There might be no words that can sufficiently express my deep gratitude to him. I wish, in one day future, I can find the way to repay for all your kindness and friendship.

Thanks should be extended to the department staffs: Carolyn, Kelly, Shannon, Heather for their supports and helps relating to school work.

Finally, I have to express my gratitude to my family: Mom, Daddy, Grandma, and Granddad for their unconditional and warm support. I especially want to thank my Mom and Daddy for always being there. Thanks Mom&Daddy, yes, it's really finished this time.

1.0 INTRODUCTION

Nanomaterials exhibit unique physical and chemical properties, such as large surface area to volume ratios and high interfacial reactivity. Nanoparticles have therefore displayed excellent chemical and physical properties that are not observed in bulk materials. In particular, shape-dependent optical, electronic, and catalytic properties of nanomaterials have motivated researchers to engineer advanced nanomaterials by modifying the shape of the materials. Developing shape controlled inorganic nanomaterials and structural manipulation of shape anisotropic particles afford tuning their intrinsic properties. Furthermore, investigating and understanding its shape anisotropic effects on functional properties have great potential for both the scientific and commercial world, since inorganic nanocrystals with tailored geometries possess peculiar shape dependent phenomena; their utilization of such phenomena is of significant interest for a wide variety of functional application.

This dissertation consists of four-independent chapters covering i) the shape control of nanomaterials and structural modification of shape anisotropic particles using nanoparticles, ii) the modification of nanoparticle assembly with 2D plate clay, iii) microwave synthesis of 3D hierarchically structured particle and its functional applications, iv) conclusions and future work. In the Chapter 1, introductions to general concepts of shape control of nanomaterials by the anisotropic growth, structural modification of clay particle through the intercalation process of oxide nanoparticles, magnetorheology control via modification of particles alignment, as well as

research motivation are included. Chapter 2 firstly addresses the interparticle-association modes in the aqueous clay suspension and the characterization method of rheological behavior of the fluid systems, and then provides experimental results on controlling rheological behavior through the surface charge modification of the clay hybrid particles. The latter part of Chapter 2 covers the synthesis of magnetic iron oxide decorated organoclay hybrid and the effects on rheological property under an external magnetic field. Microwave synthesis of 3D hierarchically structured particle is tackled in Chapter 3. In this chapter, detailed descriptions on the principle of microwave irradiation and effects of microwave heating on the chemical reaction are presented. 3D self-assembled flower-like shaped Fe_3O_4 and Fe are fabricated using microwave irradiation. The fundamental insight on the formation mechanism for the structure evolution from the primary nanoparticle building blocks to hierarchical architecture is discussed. Furthermore, flower like shaped Fe_3O_4 particles are employed as magnetic-responsive particles into the magnetorheological fluid and the change in the magnetorheology of the prepared fluids in the presence of magnetic field are introduced in Chapter 3. Lastly, conclusions and future work are summarized in Chapter 4.

1.1 THE SHAPE CONTROL OF NANOMATERIALS

1.1.1 General concept: shape control of nanomaterials

Unlike bulk inorganic crystals, whose innate properties are independent of size and shape, the physical and chemical intrinsic properties of inorganic nanocrystals can be tailored as desired [1-10]. Controlling and manipulating these properties is currently a challenging issue in chemistry and materials science. For example, Au crystals have characteristics of optical and chemical behaviors that can be tuned continuously by size control in the nano-regime. Two crucial geometric variables, size and shape, strongly affect these phenomena. Since the size of nanocrystals were found to strongly influence the physical properties of nanocrystals, early investigations focused on the nanoscale size effect [7–13]. For example, it has been shown both theoretically and experimentally that the electronic band of a crystal is gradually quantized as the crystal-size is reduced, resulting in an increase in the band-gap energy. Nanocrystal size furthermore significantly influences the electron-transport process.

Similarly, the shape of nanocrystals plays a pivotal role in determining intrinsic properties [14,15]. Based on its dimensionality, the shape of a nanocrystal can be simply classified. Figure 1.1 represents the various shape of inorganic crystal; i) 0-D isotropic spheres and polyhedrons, ii) 1-D rods and wires, iii) 2-D plates, iv) 3-D hierarchically structured particles [16-19]. A number of painstaking efforts have been performed to establish reliable synthetic routes to well-defined nanocrystals with controlled size and shape. These synthetic

strategies include liquid-phase colloidal syntheses in aqueous solution [20-24], gas-phase syntheses utilizing vapor–liquid–solid (VLS) methods [25-28], chemical vapor deposition (CVD) [29,30], thermal evaporation,[31-33], and nonhydrolytic [1,5,7] reaction media. The liquid-phase colloidal preparative approach is considered to be a powerful method for the convenient and reproducible shape-controlled synthesis of nanocrystals, not only because this method is affordable for precisely tuning the resulting nanocrystals in terms of their size, shape, and composition on the nanometer scale, but also because it allows them to be dispersed in either an aqueous or nonhydrolytic media. These colloidal nanocrystals are, moreover, often referred to as ‘molecular nanocrystals’ and can be modified by chemical hybridization with other functional materials for applications in electronics and biological systems [34-38]. In general, simplified colloidal nanocrystal growth processes can be described by the following procedure; i) seed formation initiated via a rapid increase in the monomer concentration in the solution to supersaturation levels, ii) crystal growth from seeds by aggregation of monomers on the seed to achieve thermodynamic stable status, which results in progressive decrease in the monomers concentration, and iii) surface stabilization of the resulting nanocrystals.

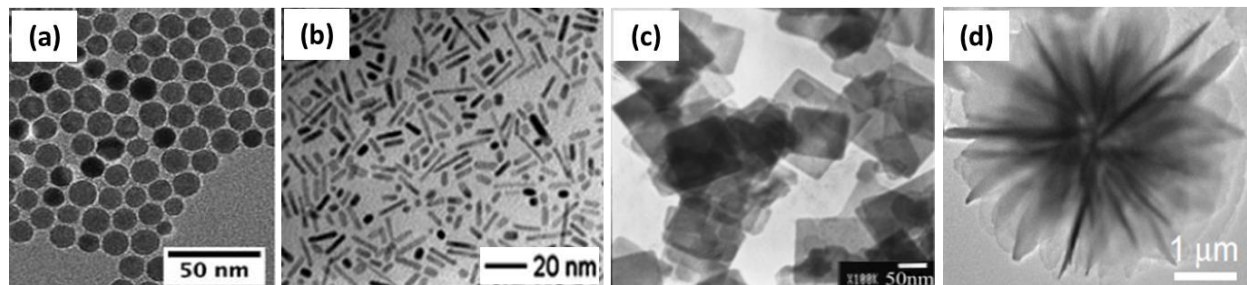


Figure 1-1 Representative examples of various shaped inorganic nanomaterials in TEM observation; (a) 0-D polyhedron, (b) 1-D rods, (c) 2-D plate, and (d) 3-D hierarchical structure [16-19]

1.1.2 Overview of proposed mechanisms for anisotropic growth

In considering the growth mechanisms of nanomaterials derived via solution based chemical process, three representative shape controlling mechanisms have been proposed to explain the assembly of species during the reaction. The proposed mechanisms are as follows:

- i) seed-mediated solution-liquid-solid (SLS) growth
- ii) oriented attachment (OA) growth
- iii) kinetically induced anisotropic growth

All of the proposed growth mechanisms above are found to be excellent for glib separation of the nucleation and growth stages, which are prerequisites to achieve shape controlled nanomaterial. This subsection will provide detailed description of the anisotropic growth behavior occurring in the proposed mechanisms.

1.1.2.1 Seed-mediated solution-liquid-solid (SLS) growth

As seeds in the chemical reaction process, nanocrystal can be beneficial for facilitating highly anisotropic growth of nanomaterials. 1D nanowires have been easily fabricated under gas-phase atmosphere through chemical vapor deposition (CVD) synthetic route which is processed based upon a vapor-liquid-solid (VLS) growth mechanism. Similar synthetic approach, so called

solution-liquid-solid (SLS) process, has been proposed by Trentler and Buhro [39,40] and applied for the generation of 1D structured particles fabrication. Dissimilar from VLS growth mechanism which can be applicable for the reactions requiring a high temperature environment, the SLS growth mechanism affords strong support for the fundamentals on low temperature (165-203 °C) growth in solution based reaction media.

The successful development of crystallized phases hinges upon the process of certain microscopic progression at the interface between nutrient and crystal as shown in Figure 1-2. During the crystal growth, existing species such as atoms, ions, or molecules in the reaction media are deposited onto a growth surface. Several consecutive elementary stages have been suggested to describe ultimate delivery of adspecies to these thermodynamic sites [41]. Buhro et al. simplified these steps into two processes; i) reversible deposition (adsorption) of adspecies from the fluid onto the growth surface, and ii) mobile diffusion of adspecies upon the growth surface. Figure 1-2 provides schematic representation of the i) and ii) processes [39].

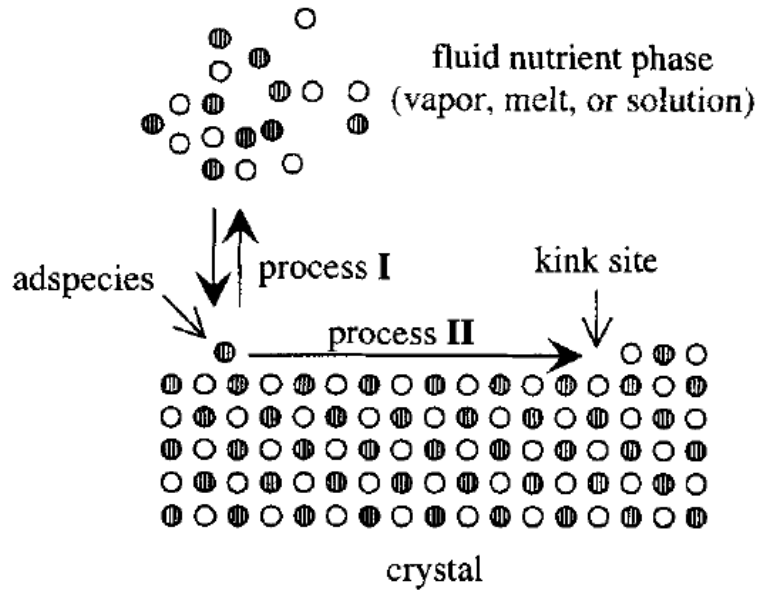


Figure 1-2 Microscopic interfacial processes supporting crystal growth [39]. Process (i) reversible adspecies deposition (adsorption). Process (ii) adspecies surface migration

Circumvention of growth defect can be feasible either by the return of mispositioned adspecies to the nutrient phase (process (i)) or by the migration of adspecies to kinks (process (ii)). In this regard, when deposition is irreversible and adspecies are immobile on the growth surface, amorphous structure is expected to be achieved than crystalline solid structure.

Figure 1-3(a) and 1-3(b) illustrates VLS mechanism and the low temperature solution-liquid-solid (SLS) growth mechanism, respectively. As mentioned above, SLS growth mechanism (Figure 1-2) is analogous to the well-reported VLS mechanism which is observed at higher temperature under chemical vapor deposition conditions [42,43].

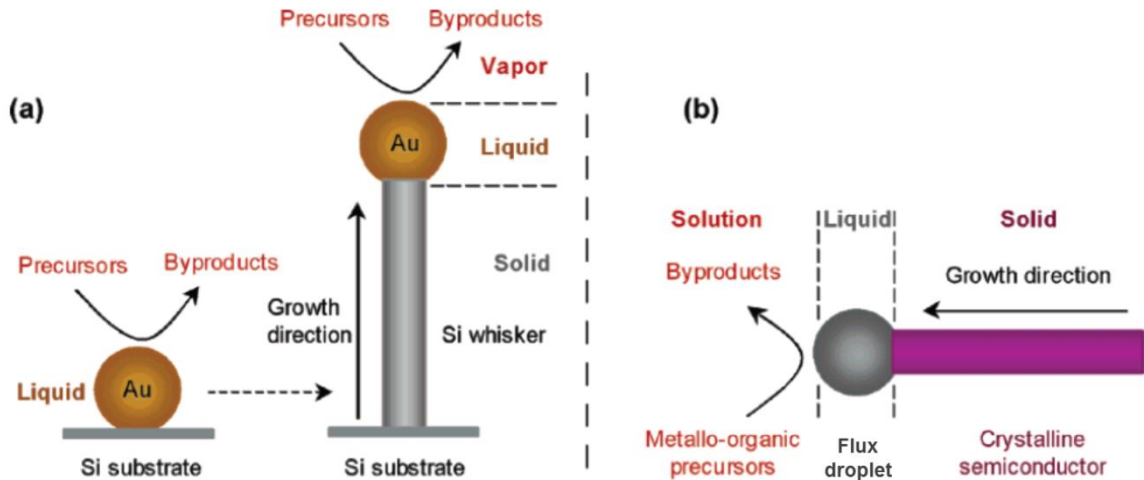


Figure 1-3 Growth mechanisms for pseudo-1D crystalline morphologies: (a) VLS mechanism proposed by Wagner and Ellis for growth under CVD conditions, (b) SLS mechanism proposed by Buhro and co-workers for analogous growth from solution [44]

The synthesis through the SLS process is conducted in solvent based dispersion of nano-sized liquid-flux droplets, which is a seed composed of target metal precursors. The precursor elements in the solution are deposited into the liquid-metal flux droplets by catalyzed reactions occurring in the solution phase. When the deposition level reaches critical point, the flux droplets become supersaturated, driving pseudo-one-dimensional crystal growth. In a polymerization process of the polymer, monomers begin polymerization with one another when they reach critical concentration in the reaction media. Similar with the polymerization of monomers, SLS growth resembles a living polymerization and a phase transfer reaction indicating the dissolution of precursor fragments (nutrients) to the living flux droplet and transferring these fragments from the solution phase to the liquid (flux) phase gives rise to low-temperature crystallization.

1.1.2.2 Oriented attachment growth

Since Banfield et al. [45] first demonstrated the concept of oriented attachment process, “oriented attachment” has attracted increasing attention in recent years as a new means for fabrication and self-organization of nanocrystalline materials under one-pot conditions [45-49].

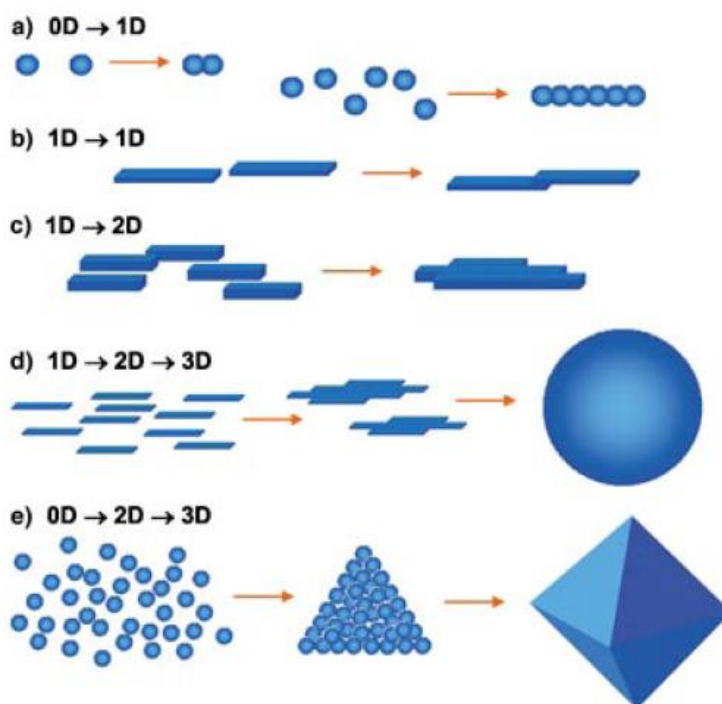


Figure 1-4 Various organizing schemes for self-construction of nano structures by oriented attachment

Figure 1-4 shows various organizing schemes for self-assembly of nanostructures through oriented attachment, including the formation of 1D nanorods from the 0D nanocrystallites (Fig 1-

4(a)), length-multiplied 1D nanostructures or 2D plate through the self-attachment by planar van der Waal interaction (Fig. 1-4(b)), or lateral lattice fusion (Fig. 1-4(c)) of 1D nanorods and ribbons, 3D architectures of 2D crystal strips derived from 1D nanoribbons (Fig. 1-4(d)), and advanced geometrical architecture from 0D through 3D (Fig 1-4(e)) [45-49]. From the classical standpoint, crystal coarsening has been described as growth of the large particles is processed through the expense of small sized primary nanoparticles by the Ostwald ripening [50]. The driving force for the Ostwald ripening process is the minimization of surface energy. In this process, firstly, tiny crystalline nuclei are formed in supersaturated media and then the formation of large particles occurs at the expense of the small primary particles owing to energy difference between large particles and smaller particles of a higher solubility based upon the Gibbs-Thompson law [51]. In these systems, the larger particles grow from small primary nanoparticles via an oriented attachment process. The adjacent nanoparticles which are thermodynamically unstable (possessing high surface energy) are self-assembled by sharing a common crystallographic orientation and merging of the particles at a planar interface. The underlying principle for spontaneous oriented attachment is that the elimination of the pair of high energy surfaces bring about a decrease in the surface free energy, implying thermodynamically stability. A number of reaction systems with the interaction of surface interfaces of the adjacent nanoparticles have produced either directed or undirected particle aggregation [52,53]. The growth mode of these systems cause the generation of faceted particles or anisotropic growth if there is numerous primary nanoparticles comprised of different crystallographic faces with sufficient surface energy difference.

1.1.2.3 Kinetically induced anisotropic growth

For producing nanomaterials with advanced architecture, kinetically induced anisotropic growth is one of the highly effective tactics that has been widely utilized in the synthetic chemistry area. Two important key factors play a pivotal role in the kinetic control of the final product shape, which are i) surface energy and selective adhesion, and ii) the effect of the crystalline seed phase. The following subsections will address an introduction to the kinetically induced anisotropic growth.

Surface energy and selective adhesion

The surface energy of the crystallographic faces of a seed determines the anisotropic growth patterns of nanocrystals. As shown in Figure 1-5, an example of ZnS growth reported by Zhang et al. highlights this kind of anisotropic growth [54]. The surface energy of each crystallographic face of ZnS seed is different in that (001) face is larger than those of other faces involving (100) and (110). Since the growth rate of the seed is in strong correlation with the surface energy, the surface energy differences between the each face intrigue rapid growth along the [001] direction of ZnS compared to the other directions and this results in the anisotropic growth along [001] direction. The other examples of the anisotropic elongation through the surface energy differences of the crystallographic faces can be found in TiO₂ and Mn₃O₄ nanorod fabrication [55-56]. Jun et al. and Cozzoli et al. addressed the shape anisotropic growth of TiO₂

induced by surface energy difference. Synthesis of Mn_3O_4 nanorod achieved through elongation along [001] direction is demonstrated by Seo et al..

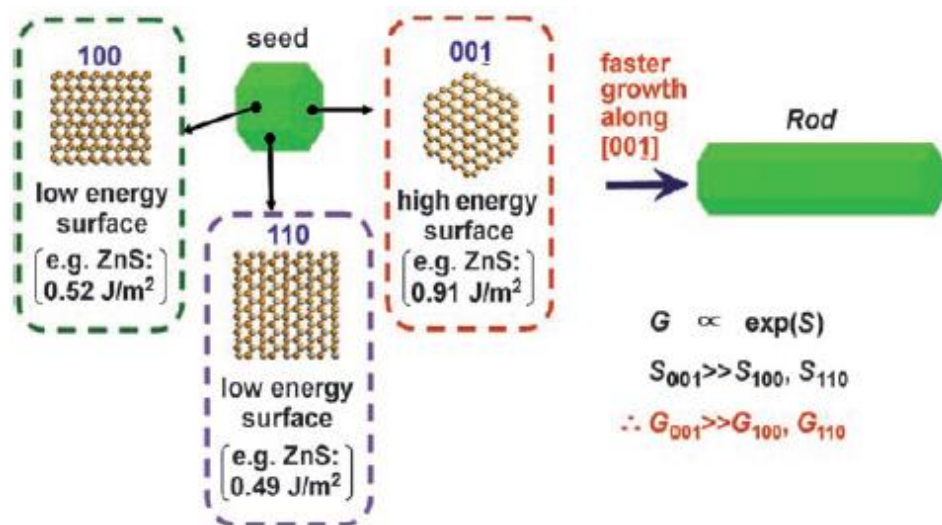


Figure 1-5 Surface energy of ZnS nanocrystals. The (001) face has the highest surface energy. Since the growth rate is proportional to the surface energy, the fastest growth occurs along the [001] direction [54]

(G = growth rate, S = surface energy)

Introducing surfactants into the reaction media affords surface energy modification of nanocrystals, in which functional group of the surfactants is preferentially attached onto the surface of growing crystallites [55-60]. In the chemical reaction system with surfactant, selective adhesion of the surfactant occurs during the reaction process in which surfactant molecules are selectively attached onto the surface of the crystallographic faces, specifically the faces in a thermodynamically unstable state (possessing high surface energy). By the selective adhesion of the surfactant, the growth rate difference between each crystallographic direction can be

modified. Manna et al. verified anisotropic growth by the selective adhesion in CdSe synthesis [57]. In this contribution, HPA is used as a surfactant and work for determining the shape of fabricated CdSe. When the reaction was performed at low concentration of HPA or absence of HPA, only spherical shape was observed in the final product. At high concentration of HPA, however, rod-shaped CdSe was obtained, since HPA is selectively anchored onto the surfaces (100) and (110) plane of the growing crystallites, suppressing the growth along the corresponding directions (Figure 1-6(a)).

Another phenomenon derived by the selective adhesion of surfactant is to induce compression along other axes. Formation of nanodisc in fabricating Cu_2S carried out by Ghezlbash et al. is a good example to elucidate this peculiar behavior [58]. Figure 1-6(b) shows the formation of nanodisc shaped Cu_2S in this work. The alkanethiol molecules which was used as surfactant binds to the (001) faces leading to decrease in the surface energy and this triggers the compression of other faces and this, in turn, results in the development of disc shaped particles.

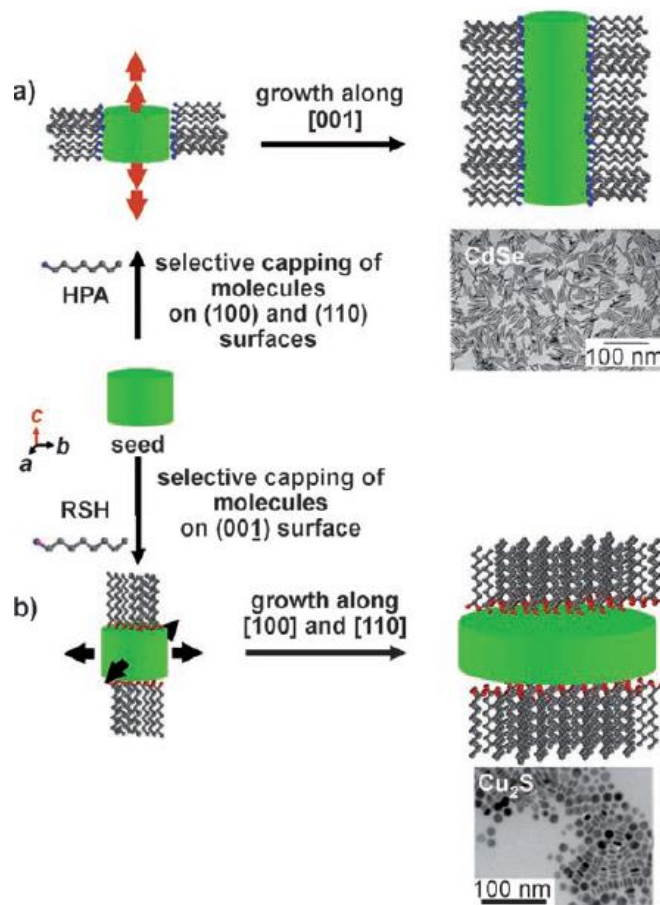


Figure 1-6 Surface modulation effects induced by the selective adhesion of surfactant: a) anisotropic rod [57], and b) disc growth [58]

The effect of the crystalline seed phase

Crystallographic phase of the nucleated seeds is also another variable for shape control of the nanocrystals. The shape of the nanocrystals is determined by its seed phase. Isotropic growth of the seed crystals with zinc blende phase and anisotropic growth of the one with wurtzite structure are good examples representing growth behavior influenced by the crystallographic phase of the nucleated seeds. When seed crystals are composed of zinc blende phase, 0D shaped particles such as spheres and cubes are achieved since the seed crystals with blende phase tends

to grow isotropically along the three axes (a , b , and c directions). In other case of seed crystals formed in a wurtzite structure, however, seeds prefer to grow anisotropically and this induces rod and disc shaped particles. Crystal seeds can potentially possess a variety of varied crystallographic phases, and the environment regulates conditions forming the stable phase [61-64]. In this regard, careful manipulation of the reaction temperature in the nucleation stage has been utilized as a simple and useful strategy for controlling the crystalline phase. Jun et al. and Lu et al. manifest control of the crystalline phase through adjusting the reaction temperature in the synthesis of MnS. [62,65]. Figure 1-7 shows the crystalline phase evolution with respect to the temperature performed in their works. At high temperature reaction regime, seed crystal with rock salt phase was preferred, resulting in the formation of isotropic cubes (Fig 1-7(a)). In contrast, lower temperature regime led to producing the seeds with wurzite phase which tend to grow anisotropically along the certain direction and this, in turn, generated nanorods (Fig 1-7(b)). Another demonstration to regulate crystalline phase through temperature mediated phase control tactic was conducted in CdS synthesis by Jun et al. and Zwlaya-Angel [61,66]. Producing CdS seed with wurtzite phase was preferred at high temperature and this gave rise to 1D nanorod formation (Fig 1-7(c)). At low temperature, however, generation of zinc blende nuclei was favorable and tetrahedral seeds with four $\{111\}$ faces are formed, and subsequently epitaxial growth of wurtzite pods along the $[001]$ direction from the $\{111\}$ faces befall, and finally, CdS bipods are formed (Fig. 7d).

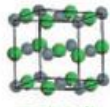
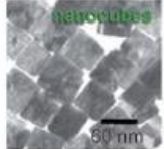
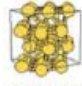
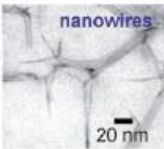
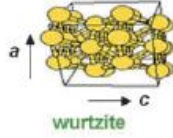


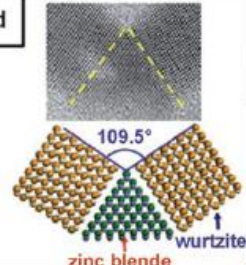
	preferred crystalline phase of seed	nanocrystal shape
Mns high ↑ growth temp. ↓ low	 rock salt	a  nanocubes 50 nm
	 wurtzite	b  nanowires 20 nm
CdS high ↑ growth temp. ↓ low	 wurtzite	c  nanowires
	 zinc blende	d  109.5° wurtzite zinc blende

Figure 1-7 Temperature-mediated crystalline-phase control of a,b) MnS and c,d) CdS nanocrystals

[61,62,65,66]

1.2 MODIFICATION OF SHAPE ANISOTROPIC PARTICLES

1.2.1 General concept of nanoparticles embedded clay composite

Porous materials find many applications in heterogeneous catalysis, metal ion trapping, and molecular separations. The intercalation of the nanoparticles into host lamellar solids is one promising approach to the rational design of porous solids with a pore size distribution on a molecular length scale. As illustrated in Figure 1-8, ceramic nanoparticle embedded clay hybrid, so called pillared clay, is a special class of intercalation composite materials in which the gallery intercalant is sufficiently large, enabling the host structure to maintain layer separation and allowing access to the intercrystal surfaces of the layered structure through the development of slit-shaped gallery pores. Pillared interlayered clays have been described as a microporous 2-dimensional labyrinth structure of molecular dimensions that is typified by the distance between the clay layers, the interlayer spacing, and the distance between the intercalated oxides, interpillar spacing. This heterostructured composite particle is analogous to supramolecular assembly processes used to form mesoporous molecular sieves. Moreover, porous clay heterostructures exhibit acidic properties for potential applications as sorbents and heterogeneous catalysts, while at the same time providing larger surface areas and pore sizes [67-70].

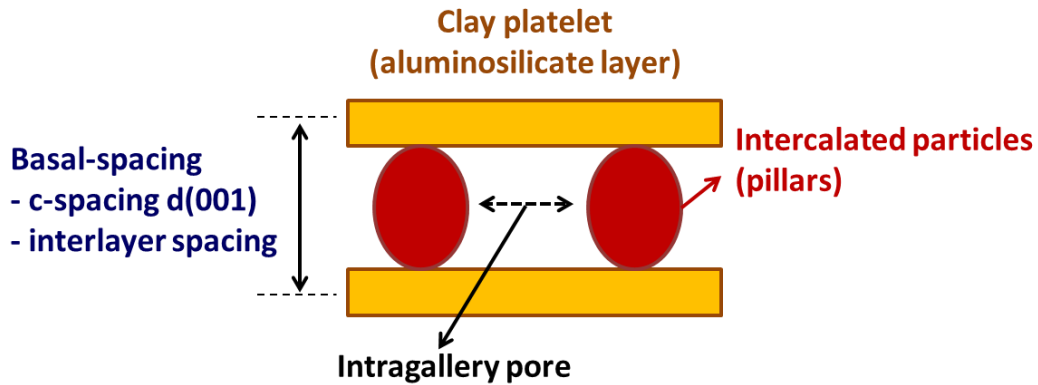


Figure 1-8 Schematic representation of the porous structured nanoparticles embedded clay hybrid composite

The interlayer spacing along the *c*-dimension is determined by the chemical nature and the height of the intercalated particles. The pore size in *a* and *b* dimensions is characterized by three parameters including the distance between the pillars and the interpillar distance. In particular, the interpillar distance is mainly associated with the density of pillars, indicating the number of intercalated species between the aluminosilicate layers. The extent and the distribution of the charge density on the clay layers and size of the pillars strongly affect the density of pillars. The interlayer and interpillar spacing can be regulated in the thermal treatment stage of the fabrication process, in which elimination of organic components of the polycations and the thermal annealing of pillars occurs.

1.2.2 Structural features of clay particles

Montmorillonite, a subset of clay, contains lamella structures, composed of phyllosilicates or layer silicates with a layer lattice structure in which two-dimensional

oxyanions are separated by layers of hydrated cations. The oxygen atoms define upper and lower sheets enclosing tetrahedral sites, and a central sheet having the brucite or gibbsite structure enclosing octahedral sites (Figure. 1-9). Clay that consists of two tetrahedral sheets around the central octahedral sheet in each layer is categorized as 2:1 phyllosilicates.

All tetrahedral sites are filled with Si^{4+} , and other species occupying the octahedral sites are Al, Mg, and Fe cations, respectively. The electrically neutral sheets are bonded together by relatively weak dipolar and van der Waals forces [71]. In contrast, montmorillonite clay has a negative charge at its face and positive charge at edge sites resulting from the isomorphous substitutions, via (i) Si^{4+} by Al^{3+} at tetrahedral sites, and (ii) Al^{3+} by Mg^{2+} , or (iii) Mg^{2+} by Li^{+} at octahedral sites. The charge variation is balanced by absorbed cations, such as, Na^{+} , K^{+} . The montmorillonite clays were used as the first choice to fabricate nanoparticle-embedded clay materials, because it is cost effective, abundant and easily processed in water. Furthermore, the surface charge strongly influences the ion exchange and swelling of the clay, and the rheology of the clay fluids.

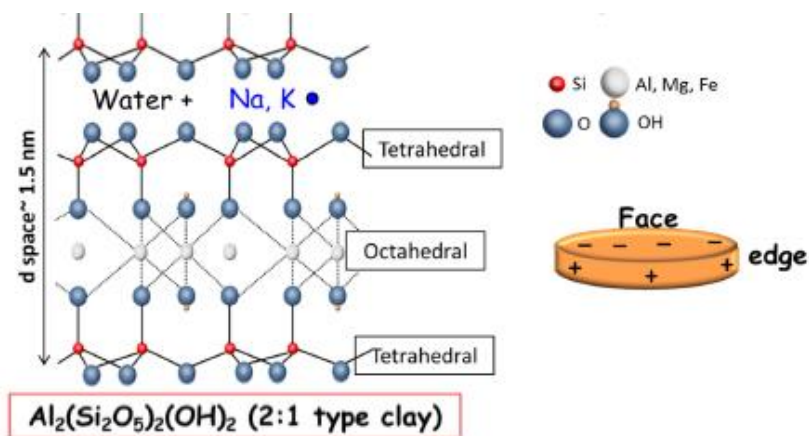


Figure 1-9 Schematic illustration representing structure of montmorillonite clay

1.2.3 The nanoparticles embedded clay hybrid composite

The modification of the physical and chemical properties of clay materials can be achieved via pH control using base and acid activation. For the layered clays, intercalation of metallic polycations into their interlayer region is widely used. The intercalation of metallic polycations brings about the generation of a new porous structure and the creation of active sites (acid and/or metallic), improving its intrinsic property. Over the past several decades, the development of inorganic pillared interlayered clays (PILCs) has created remarkable new opportunities in the field of the synthesis and applications of clay-based solids [72,73].

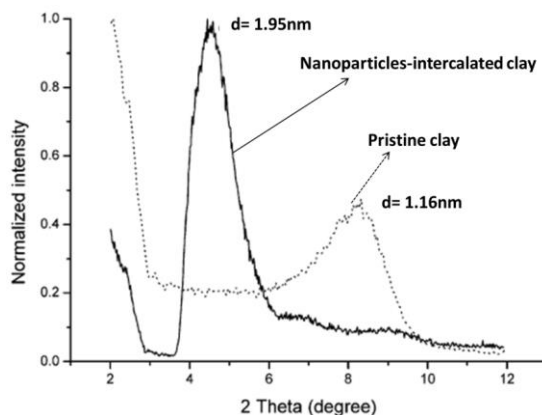


Figure 1-10 XRD patterns of pristine clay and nanoparticles (NPs)-intercalated clay [74]. Increase in c-spacing by intercalation of NPs into clay results in XRD peak shift to lower angle

The general fabrication approach of pillared interlayered clays is the intercalation of metal polycations into swelling clay particles. Through high temperature heat treatment, the intercalated polycations are successfully converted into the corresponding metal oxide via dehydration and dehydroxylation, and embedded oxides serve as ‘pillars’, creating interlayer meso- and micro-pores. In addition, *c*-spacing (basal spacing) of the parent clays increases by the intercalation of metal cation (Figure 1-10) [74]. The interlayer distance can be estimated from the basal *c*-spacing value ($d(100)$) obtained through the XRD patterns investigation. Fabrication of pillared clay is divided into four steps: expansion, exfoliation, intercalation, and calcination. In the intercalation step, the replacement of naturally absorbed Na^+ and K^+ cations by larger, more robust cations results in a pillared structure. In the annealing process, the embedded polycations yield rigid, thermally stable oxide species (pillars) which maintain the separation of the clay layers, thus preventing their collapse. This process results in an interesting two-dimensional porous structure of molecular dimensions (Figure 1-11).

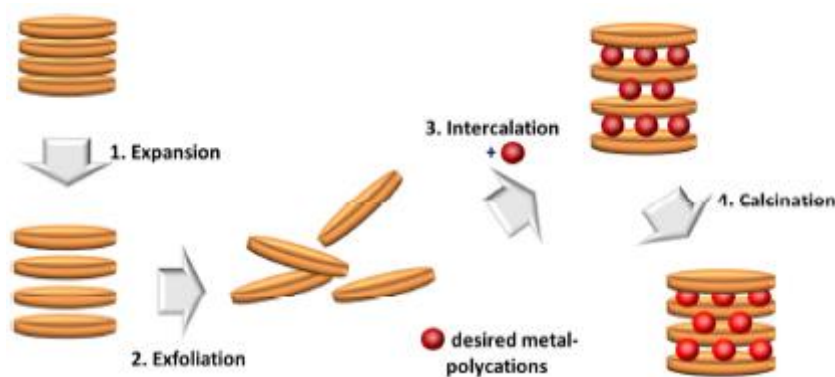


Figure 1-11 Schematic illustration of nanoparticles intercalation process

1.3 MAGNETORHEOLOGY CONTROL

1.3.1 General concept and characteristics of magnetorheological fluids

Magnetorheology is a subset of Rheology instigating the flow and deformation behaviors of the fluid system under a magnetic field. Magnetorheological (MR) fluids are suspensions of micrometer range ferro- or ferromagnetic multi-domain particles in a liquid matrix [75]. MR fluids are reversible and very fast (in millisecond) transition from a liquid to a solid state under the presence of applied magnetic field. The basic phenomena occurring in MR fluids system is related to the control of the structure of two-phase fluid by relatively moderate magnetic fields. The applied fields induce a polarization of the multi-domain magnetizable particles which result in their aggregation and/or forming network structure, and this, in turn, brings about tremendous increase in the viscosity (up to 10^3 times). As shown in Figure 1-12, in ‘on-set’ state of the magnetic field, magnetic moment in the MR fluid is induced by the applied field and it is vanishing at ‘off-set’ state (zero field), and the suspension returns back to its initial state [76]. In the absence of a magnetic field, MR fluid systems typically behave as Newtonian fluids. In contrast, when a magnetic field is applied transverse to the direction of flow, a yielding, shear thinning, and viscoelastic behavior are perceived. Strong interaction between magnetically induced particles gives rise to developing the chain-like network formation of the particles in the

direction of the field, and this is responsible for the increase in the viscosity of MR fluid under an applied magnetic field (Fig. 1-12c).

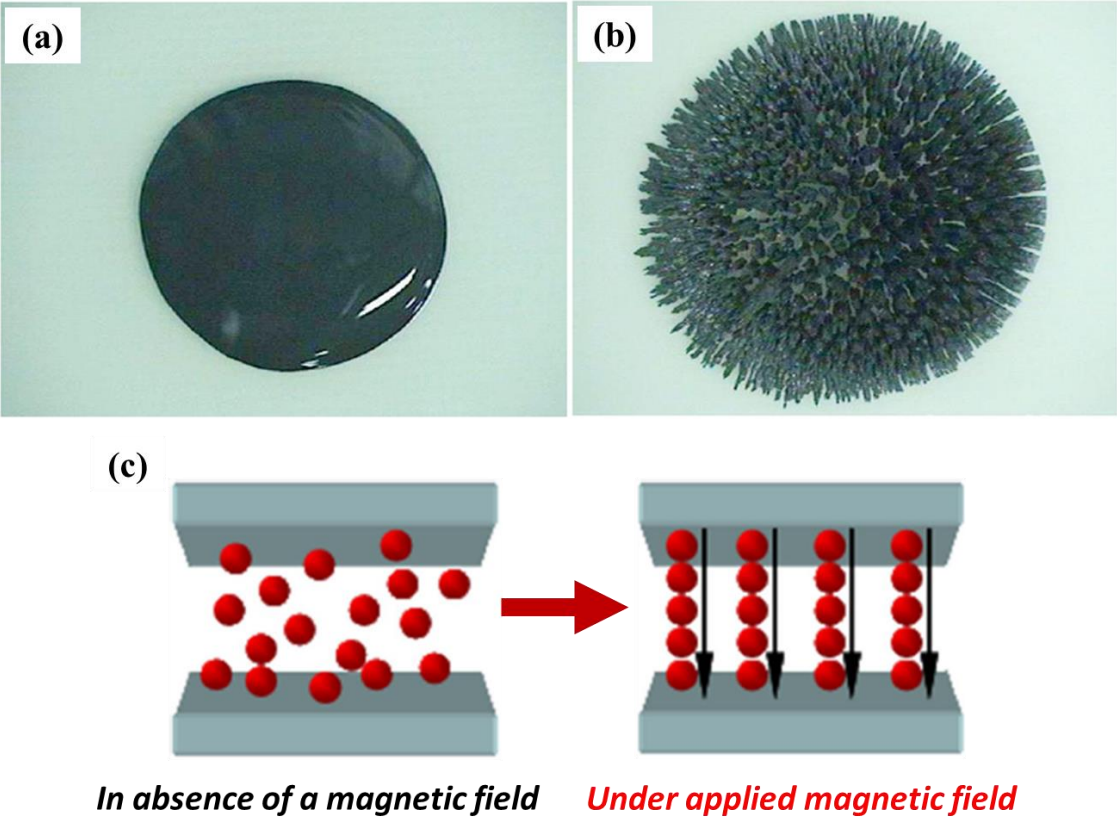


Figure 1-12 The surface changes of a MR fluid under applied magnetic field: (a) liquid phase under no magnetic field, (b) solid phase under an applied magnetic field, (c) alignment of the magnetic particles along the direction of a magnetic field [76]

Due to its fascinating behavior in the presence of a magnetic field, MR fluids are intensively attractive in the applications in mechanical system that involves active control of vibrations or the transmission of torque. Conventional applications include shock absorbers, clutches, brakes, seismic vibration dampers, artificial joints, and control [77]. Other applications

are extended to biomedical application, precision polishing, thermal energy transfer, sound propagation, and chemical sensing applications which require the utilization of magnetic field [78-82].

1.3.2 MR fluids

Typical MR fluids are two-phase fluids, and the fluids preparation can be achieved by dispersing a large quantity of highly magnetizable particles (micron-size) in a non-magnetizable liquid. Iron particles, particularly fabricated from thermal decomposition of carbonyl iron particles, are most widely used in various cases since they exhibit a high saturation value of magnetization ($\mu_0 M_s = 2.1$ T). Water, silicone oils, polyesters, polyethers, and synthetic hydrocarbons are commonly used as a liquid carrier. Use of additives including thixotropic agent, surfactants and polymers is necessary to deter severe precipitation and aggregation.

As described above, the field induced magnetization of the suspended particles is a driving force to intrigue MR effect. In the absence of a magnetic field, a viscosity of the suspension is relatively low. When external magnetic field is applied to the system, particles are magnetically induced and attracted one another along the applied field direction, and they develop anisometric aggregation (chain-like network formation). The resulting suspension shows a large yield stress. Since the developed chain-like network enhances the resistance to the system that tends to flow, higher shear stress is required to enable the suspension flow. In general, good MR fluids are to possess a large saturation magnetization, minimal remnant magnetization, applicable to wide temperature range, stable against sedimentation, and irreversible flocculation.

Other types of MR fluids, which include inverse-ferrofluids, magnetic composites containing fluids exist and are often employed. Inverse-ferrofluids are comprised of non-

magnetizable particles with micron size and ferrofluids [83,84]. In the inverse-ferrofluids system, the strength of the applied magnetic field and the saturation magnetization of ferrofluids play a central role in controlling the rheological behavior of the system. Since a wide variety of non-magnetizable particles are available, the functionality of the fluid system can be easily tunable by varying particle size and shape [85,86]. In the preparation of ferrofluid suspensions, two immiscible fluids containing one being magnetically inducible, are utilized [87,88].

Polymer based magnetic-responsive particles containing MR fluids are regarded as magnetic composites MR fluids, which consists of the solid counterpart of ferrofluids and MR fluids. Magnetic gels and elastomers [89,90] are widely known magnetic composites. Synthesis of magnetic elastomer is relatively simple and reliable, in which magnetic particles are added into polymer precursor solution and a magnetic field is applied prior to initiating crosslinking of polymer cluster. In some case studies on colloidal aggregation and optical trapping behavior, field-responsive composite involving superparamagnetic polymer-based particles have been employed [91,92].

1.3.3 Field induced particle interactions and structure formation

In case of MR fluids, particle interactions under an applied magnetic field are significantly strong and develop a formation of thick column of particles, which radically change the flow behavior [75]. Given a system of an isolated particle of relative magnetic permeability μ_p in the fluid with relative permeability μ_f under an external magnetic field \mathbf{H}_0 , a magnetic moment that particle will acquire is:

$$m = 4\pi\mu_0\mu_f\beta a^3 H_0 \quad (1.1)$$

Where a is the radius of the particle, μ_0 the permeability of vacuum, and $\beta = (\mu_p - \mu_f) / (\mu_p + 2\mu_f)$. This equation also holds when the permeability of the carrier fluid is larger than the one of the particle ($\beta < 0$) and the magnetization vector is opposed to the field. The interaction energy between two dipoles of moment m is expressed by;

$$W = [(m_\alpha m_\beta / r^3) - \{3(m_{\alpha r})(m_{\beta r}) / r^5\}] / 4\pi\mu_0\mu_f \quad (1.2)$$

where r indicates the separation vector between the centers of the two particles. This energy reaches the minimum when the two dipoles are aligned with r , while the maximum is achieved when they are perpendicular, which triggers a preferential aggregation developing a chain-like network formation of the particles along the applied magnetic field direction. The formation of particle network is dependent on the ratio of this interaction energy to kT . Taking into account the interaction energy between two dipoles of moment m , the non-dimensional interaction energy of two dipoles in repulsive configuration gives

$$\lambda = \pi\mu_0\mu_f\beta^2 a^3 H_0^2 / 2kT \quad (1.3)$$

For the particles having a diameter of $1\mu\text{m}$ with large permeability ($\beta \approx 1$) and $T = 300\text{K}$, $\lambda = 1$ for $H = 127 \text{ A/m}$, which corresponds to 1.6 Oe , can be obtained. In the fluid system with $\lambda > 1$, even under moderate magnetic field, magnetic forces usually dominate Brownian motion, and the random forces originating from Brownian motion can be neglected.

In order to procure all the quantities which govern the suspension behaviors, Stokesian dynamics are dimensionless and are useful approach as an equation of motion of a single particle, and allowing calculation of the trajectories of the particles [93,94]. For a given particle, we can write:

$$m(dv/dt) = \mathbf{F}^H + \mathbf{F}^{\text{ext}} + \mathbf{F}^I + \mathbf{F}^B \quad (1.4)$$

\mathbf{F}^H represents the hydrodynamic force on the test particle coming from the hydrodynamic friction and is proportional to $-\xi(v - v_0(x))$, where $\xi = 6\pi\mu a$, with μ the viscosity of the suspending fluid and $v_0(x)$ the imposed velocity field at the location x of the particle. The term \mathbf{F}^{ext} is the hydrodynamic force attributed to the symmetric part of the velocity gradient tensor. In the case of a pure shear characterized by the shear rate $\dot{\gamma}$, the scale of this force is as $6\pi\mu\dot{\gamma}a^2$. The third term \mathbf{F}^I reveals the interparticle force originating from the dipole-dipole interaction shown above. Concerning two particles α and β , the force can be displayed:

$$\mathbf{F}_{\alpha}^I = 12\pi\mu_0\mu_r a^2 \beta^2 H_0^2 (a/r)^4 [(2\cos^2\theta_{\alpha\beta} - \sin^2\theta_{\alpha\beta})\mathbf{e}_r + \sin^2\theta_{\alpha\beta}\mathbf{e}_{\theta}] \quad (1.5)$$

The last term \mathbf{F}^B is associated with the Brownian random force, which scales as kT/a . Since the inertial force can be neglected, the left hand side in equation (1.4) also can be neglected. The following equation is attained through dividing all the terms in equation (1.4) by $6\pi\mu\dot{\gamma}a^2$;

$$(v-v_0)/\dot{\gamma}a = [F^I]/M_n + [F^B]/P_e + [F^{\text{ext}}] \quad (1.6)$$

where M_n is the Mason number and P_e is the Peclet number;

$$M_n = 8\mu\dot{\gamma}/\mu_0\mu_f\beta^2H_0^2 \quad (1.7)$$

$$P_e = 6\pi\mu\dot{\gamma}a^3/kT \quad (1.8)$$

and M_n represents the ratio of shear to magnetic forces, and P_e is the expression of the ratio of shear forces to Brownian forces. For the particles with size larger than 1 μm and rational shear rates, the Peclet number is large enough to allow for neglecting the Brownian force. The non-dimensional magnetic dipole energy λ is related to the Mason number and to the Peclet number by the relation $M_n\lambda = 2P_e/3$. For a given MR fluid, the viscosity will be the same for the same values of M_n and λ .

1.4 RESEARCH MOTIVATION

1.4.1 Fluid rheology control via nanoparticle assembly with 2D clay particle

1.4.1.1 Rheology control of nanoparticle clay hybrid added bentonite suspension

As described in the section on structural features of clay particle, clay has a negative charge at the face and positive charge at the edge site resulting from the cation substitutions that occurs in tetrahedral and octahedral layers. Plate-like clay particles are connected to each other in the fluid through several modes; edge-to-face (E-F), edge-to edge (E-E), and face-to-face (F-F) type coagulations of clay particles. The driving force of the E-F type coagulation is the electrostatic force resulting from the negatively charged surface and the positively charged edges (E-F). Attraction between adjacent platelets via van der Waals forces leads to an E-E or F-F type coagulation. Modification of interparticle interactions is the most important factor for controlling viscosity, storage and loss modulus of clay suspensions. Although many studies have been conducted to modify interparticle interaction, the protocol of most trials has been based on the variation of clay suspension properties such as adjusting the ionic concentration and pH or using additives such as organic surfactants, polymers and nanoparticles as thickening agents [95-109]. Clay-nanocomposite embedding Fe_2O_3 , Al_2O_3 , ZrO_2 , TiO_2 , ZnO , $\text{SiO}_2\text{-Al}_2\text{O}_3$, $\text{Al}_2\text{O}_3\text{-Cr}_2\text{O}_3$, $\text{SiO}_2\text{-TiO}_2$, and $\text{SiO}_2\text{-CoO}$ nanoparticles have been successfully synthesized [110-116]. They are used in catalytic reaction, water purification, and sorption-based chemical separation [117-119].

However, the effect of these nanoparticles intercalated clay particles as additives on the rheological properties of clay suspensions have not been investigated.

In this section, the hybrid clays, Fe₂O₃-embedded and Al₂O₃-SiO₂-embedded clay hybrid composites are fabricated. Then, the effect of nanoparticle intercalated clay hybrid composites on montmorillonite suspensions and a specific effect of pH on the surface charging of montmorillonite suspensions containing clay hybrid particles will be introduced. Fe₂O₃ and Al₂O₃-SiO₂ nanoparticles have been selected as the target species for embedment since they possess large variation of surface charge as a function of pH. This would allow for the clear comparison of different rheological behaviors resulting from changes in surface charges.

1.4.1.2 Magnetorheology control of iron oxide nanoparticle decorated organoclay fluid

As mentioned in previous sections on MR fluids, suspensions of the magnetically responsive nanoparticles can be rapidly and reversibly transformed between a liquid-like to a solid-like state within milliseconds in the presence of a magnetic field. Magnetic iron oxide nanoparticles have been widely utilized in preparation of MR fluid. However, a number of researchers have pointed out that very fine iron oxide nanoparticles do not have large magnetic moment which results in the magnetic force of fine nanoparticles being insufficient to subdue Brownian motion in the fluid. In parallel, the use of large magnetic particles has pros and cons. While large magnetic particles possess a significant magnetic moment, they exhibit large remnant magnetization. In this regard, magnetic nanoparticles assembly is gaining growing attention in that the collective response of magnetic nanoparticles triggers both a large magnetic moment, as well as high sensitivity to an external field. To achieve stable and reliable magnetic

nanoparticles arrays, several materials including clay minerals have been examined as a supporter for the nanoparticles.

In this work, magnetic iron oxide nanoparticles (γ -Fe₂O₃) decorated organoclay hybrid particles, which are structurally different from the nanoparticle embedded clay hybrid particles, are fabricated. Then, we instigate the self-assembly of magnetite nanoparticles on the surface of hydrophobic clay in organic liquid, which does not require electrostatic interaction between the nanoparticles and the clay minerals. In addition, magnetorheological (MR) property of the organic fluid of nanoparticle decorated organoclay will be examined.

1.4.2 Facile synthetic route of 3D structured particles via MW irradiation

1.4.2.1 MW-synthesis of self-assembled Fe and Fe₃O₄ particles for wastewater treatment

Rational control over the morphology, crystalline structure, and size of nanostructures has attracted much attention due to their novel chemical and physical properties [120]. Recently, the synthesis of Fe-based nanomaterial with 3-dimensional hierarchical architecture has been extensively studied because of its versatility for a wide variety of applications. Conventional preparative methods for the synthesis of hierarchically structured Fe-based nanomaterials, require several hours to a day to complete achieving the desired nanostructure. Although researchers have introduced and developed well-designed synthetic tactics to achieve 3-D architecture, the structure transformation from the primary nanoparticles to the final structure has not yet been clearly identified. We synthesized 3-D hierarchically superstructured flower-like shaped (FLS) Fe and Fe₃O₄ particles. To increase the reaction rate, microwave irradiation was employed. Furthermore, the effects of critical variables (particularly reaction temperature and

pressure) on the final architecture will be discussed, and plausible formation mechanisms will be suggested. Furthermore, the fabricated particles are employed to the application in wastewater treatment containing sulfide species.

1.4.2.2 Investigation of magnetorheological behavior of the fluid

The other case study in this chapter is to employ this hierarchically structured iron Fe_3O_4 particle to control rheological behavior of aqueous fluid under magnetic field. In this part, we focus on the interparticle association in the fluid to explain the change in MR behavior in the presence of a magnetic field.

2.0 MODIFICATION OF NANOPARTICLE ASSEMBLY WITH 2D PLATE

2.1 INTRODUCTION

2.1.1 Surface charge modification of 2D clay particle

Clay minerals are intensively utilized in a wide range of applications such as ceramic products, drilling fluids, molding sands, paints, and paper making [121,122]. Among the clay minerals, bentonite, a smectite type clay mineral, has attracted much attention due to its unique swelling ability, ion-exchange capacity, and rheological properties. In particular, the rheological properties of bentonite suspensions have been considerably studied. The most important factor to directly control the viscosity and the storage and loss modulus of clay suspensions is interparticle interaction. Plate-like clay particles in the fluid are connected through several modes: edge-to-face (E-F), edge-to-edge (E-E), and the face-to-face (F-F) type coagulations of clay particles. The driving force of E-F type coagulation is an electrostatic force resulting from the negatively charged surface and the positively charged edges (E-F). Attraction between adjacent platelets by van der Waals forces leads to E-E or F-F type coagulation. To modify interparticle interaction, researchers have changed the ionic concentration [95-98] and pH [99-101] of the fluids. Additives such as organic surfactants, [102-104] polymers, [105-107] and nanoparticles [108,109] have been also added to the fluid as thickening agents. Intercalation of nanoparticles

into the interlayer space of clay can introduce new functional properties to clay. Native clay minerals normally bind Na^+ and Ca^+ cations at the intragallery exchange sites. The replacement of the small cations by larger, more robust polycations transforms the clay to pillared clay with subsequent thermal treatment. Inorganic pillared interlayered clays (PILCs) embedding Fe_2O_3 , Al_2O_3 , ZrO_2 , TiO_2 , ZnO , $\text{SiO}_2\text{-Al}_2\text{O}_3$, $\text{Al}_2\text{O}_3\text{-Cr}_2\text{O}_3$, $\text{SiO}_2\text{-TiO}_2$, and $\text{SiO}_2\text{-CoO}$ nanoparticles have been successfully synthesized [110-116]. They are used in catalytic reactions, water purification, and sorption-based chemical separation [117-119]. However, the effect of these nanoparticle intercalated clay particles as additives on the rheological properties of clay suspensions has not been investigated. The objective of this work is to introduce the effect of nanoparticle intercalated clay hybrid particles on montmorillonite suspensions and specific effect of pH on surface charging of montmorillonite suspensions containing clay hybrid particles. To the best of our knowledge, in a recent work, only the heterocoagulation process between montmorillonite and nanoparticles has been extensively studied, which reported the interaction of clay particles with oppositely charged inorganic oxide nanoparticles [108,109]. In this work, two different types of hybrid materials, iron oxide-clay hybrid (ICH) and $\text{Al}_2\text{O}_3\text{-SiO}_2\text{-clay}$ hybrid (ASCH) were studied. We synthesized the hybrids and investigated their structural characteristics. In addition, we explored the effect of added hybrid particles on the rheological behavior of bentonite suspensions as a function of surface charge. Also, the viscosity of prepared bentonite suspensions containing hybrid particles is examined in a high-temperature, high-pressure environment.

2.1.2 Magnetorheological property of iron oxide decorated clay fluid

Nanophase magnetic materials have been extensively studied because of their potential applications [123-125]. Suspensions of the magnetic nanoparticles, so called ferrofluids, are regarded as smart materials, meaning that they can be rapidly and reversibly transformed between a fluid-like to a solid-like state within milliseconds by applying a magnetic field [75]. Consequently, the suspensions of the magnetic nanoparticles show dramatic and tunable changes in rheological properties under the influence of the external applied magnetic field. In addition, functionalized $\gamma\text{-Fe}_2\text{O}_3$ nanoparticles have been studied for use in separating target materials magnetically, which is a more selective and efficient method than others such as centrifugation or filtration [126-129]. However, very fine iron oxide nanoparticles do not have large magnetic moment and the magnetic force of fine nanoparticles is not large enough to overcome Brownian motion in the fluid. At the same time, while large magnetic particles have large magnetic moment, they have a larger coercive field and remnant magnetization. Therefore, in larger particles, the relative change in the magnetization over an external magnetic field is small and the magnetic response is less sensitive to an external field than that of fine nanoparticles.

In this regard, magnetic nanoparticles arrays are receiving a considerable amount of interest. This is because the collective response of magnetic nanoparticles generates both large magnetic moment and high sensitivity to an external field, which is needed for many applications of magnetic materials. Several supporting materials have been studied to induce the assembly of the nanoparticles [95-99]. Clay minerals provide one of the best matrix materials on which nanoparticles can be collected and aligned in that clay minerals are abundant, environmentally friendly and economical [110-115]. Since plate type clay materials have different electric charges locally in water, the surface, edge or interlayer space of clay materials can be decorated

with charged nanoparticles. When the magnetic nanoparticles were attached to clay minerals, a movement of nanoparticle-clay mixture was controlled by applying a magnetic field. Because of a tunable motion of the mixture and an absorbent ability of the clay, the mixture of magnetic nanoparticles and clay minerals was successfully used to separate contaminants in water [127,129,130].

To date, however, studies on the magnetic nanoparticle decorated clay have been mainly carried out in an aqueous fluid system. In organic solutions, the electrostatic interaction between clay and oxide nanoparticles is not strong and the viscosity of the base fluid is large. Consequently, it is difficult to stimulate a strong magnetic response by applying a small magnetic field to organic suspensions of a clay-magnetic nanoparticle mixture. In this study, we investigate the self-assembly of magnetite (Fe_3O_4) nanoparticles on the surface of hydrophobic clay in organic liquid, which does not require electrostatic interactions between the nanoparticles and the clay minerals. We also examine the magnetorheological behavior of the organic fluid of nanoparticle decorated hydrophobic clay (called organoclay). When plate-type montmorillonite and magnetite nanoparticles are treated with alkyl amine and oleic acid, magnetite nanoparticles are strongly attached to the surface of montmorillonite due to hydrophobic attraction. Such magnetite nanoparticle decorated clay is well dispersed in organic media and the rheological properties of the fluid are easily controlled by applying a magnetic field.

2.2 BACKGROUND

2.2.1 Structure of 2D plate clay and interparticle-association

Today, clays are one of important materials in a wide variety of applications fields covering the ceramics, cosmetics, cement, drilling fluids, metal, and paper industry [131]. The use of clay is further extended to adsorbent, decoloration agents, ion exchangers, and molecular sieve catalysts [132]. Clay particles exhibit distinguished behavior from other colloidal materials by the highly anisometric particle shape, the broad particle size distribution, flexibility of the layers, the outstanding cation exchange capacity, and the different association modes of aggregation originating from anisotropic surface charge difference (permanent charges on the face and pH-dependent charges at the edge) [133]. Montmorillonite, a subset of clay, has lamella structures, and its general formula is $(Al_{2-y}Mg_y)Si_4O_{10}(OH)_2 \cdot (M^+, M_{1/2}^{2+})_y \cdot nH_2O$ [134]. Figure 2-1 illustrates the structure frame work of the clay which is basically composed of two layers, alumina and silica sheets that are stacked on the top of each other. The central octahedral sheet is sandwiched by two tetrahedral sheets, and these units are occupied in the atomic lattices of clay particles [135]. The octahedral sheet is comprised of closely packed oxygen and hydroxyls and Al, Mg, and Fe atoms are embedded in octahedral coordination which stays in equidistant from six oxygen atoms or hydroxyls. The other unit around the octahedral sheet is called the tetrahedral sheet, which is built of silica tetrahedrons. In each tetrahedron, a silicon atom is equidistant from six oxygens and hydroxyls. The silica tetrahedral groups are positioned to form

a hexagonal structure, and it is repeated open-endedly for the sheet formation of $\text{Si}_4\text{O}_6(\text{OH})_4$. The combination of two tetrahedral sheets and the octahedral sheet is denoted as a unit layer, and the clay particles composed of unit layers are called 2:1 type clay. Most clay minerals consist of unit layers in a form of being stacked parallel to each other. Indefinite stacks of unit layer in face-to-face orientation form a crystal lattice. The distance between the plane in one layer and another plane in the next layer is known as basal or c-spacing $d(001)$. Each sheet in the unit layer is held together through covalent bonding, which makes unit layer stable.

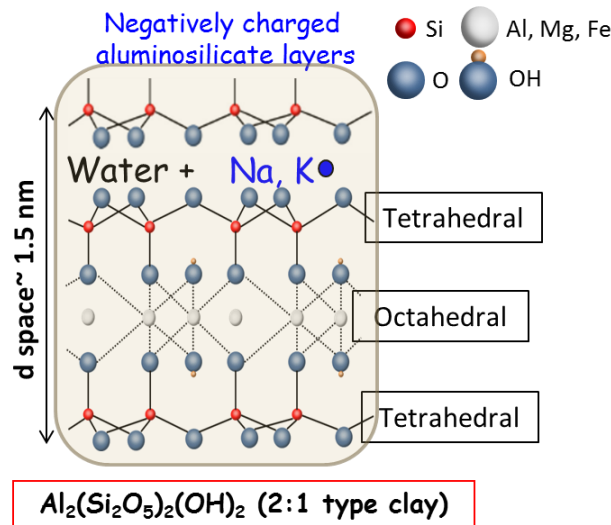


Figure 2-1 Schematic illustration of clay structure

Crystals of clay particle carry a charge, and the main contribution to the surface charge of clay layers is the permanent negative charge on the basal planes due to the isomorphous substitutions of certain atoms in their structure for other atoms of a different valent [136]. In the tetrahedral sheet, the replacement of Si^{4+} for Al^{3+} occurs, which results in localized charge distribution, while either Mg^{2+} or Fe^{2+} replaces Al^{3+} in the octahedral sheet [137]. This leads to

charge deficiency and a negative charge is created on the surface of clay. Aroused negative charges can be compensated by naturally absorbed cations such as Na^+ and K^+ . Additional polar sites, mainly octahedral Al-OH and tetradral Si-OH groups, are situated at the broken edges [137]. These amphoteric sites are conditionally charged, and variable charges can be promoted by direct H^+ or OH^- migrated from aqueous media.

As described, isomorphic substitution associated with the structural characteristic in the clay particle intrigues surface charge anisotropy in the clay, representing negatively charged face and pH-variable edge site. The surface charge anisotropy between the face and edge in the clay develops unique interparticle associations in the clay suspension. As illustrated in Figure 2-2, when a suspension of clay particles flocculates ($>3\text{wt}\%$ clay in a given suspension), three different association modes possibly take place, which are i) face-to face (F-F), ii) edge-to-edge (E-E), and iii) edge-to-face (E-F). F-F and E-E interactions occur through attraction between adjacent clay platelet by Van der Waals forces, while electrostatic forces between the negatively charged faces and the positively charged edges give rise to E-F association mode. F-F association which brings about thicker and larger flakes decreases in the gel strength due to minimizing the number of platelet units to participate in constructing gel structure and surface area necessary for interaction between platelets. Meanwhile E-F and E-E interparticle associations promote to build a gel-like structure with three dimensional voluminous ‘cardhouse’ in the clay suspension. The particle association between clay platelets determines the rheological behavior of the clay-based fluid system and this will be discussed in experimental section.

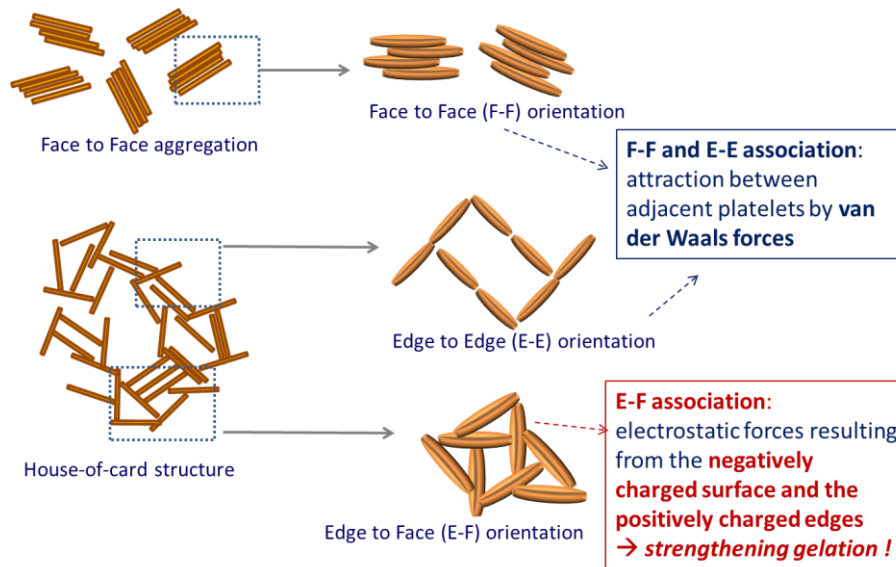


Figure 2-2 Association modes of individual clay platelet

2.2.2 Estimating rheological properties of fluid systems

2.2.2.1 Flow behavior of clay suspension

The flow behavior of any system is illustrated in terms of the relationship between the shear stress τ and the shear rate $\dot{\gamma}$. The shear stress is stated precisely as the tangential force applied per unit area, and the shear rate is defined as the change of shear strain per unit time. The ratio of shear stress τ to shear rate $\dot{\gamma}$ is defined as viscosity η . In other words, η indicates a measure of the resistance to flow of fluid suspension.

$$\eta = \frac{\tau}{\dot{\gamma}} \quad (2.1)$$

Figure 2-3 depicts fluid behavior of five different types of fluid systems: Newtonian, pseudoplastic, Bingham plastic, Bingham, and Dilatant. The Newtonian which the shear stress is directly proportional to shear rate, reveals constant viscosity, whereas viscosity of other types of fluid behavior called non-Newtonian fluids could be varied with shear rate. Correlation between shear stress and shear rate of aqueous clay suspensions basically follows the Bingham plastic behavior [138].

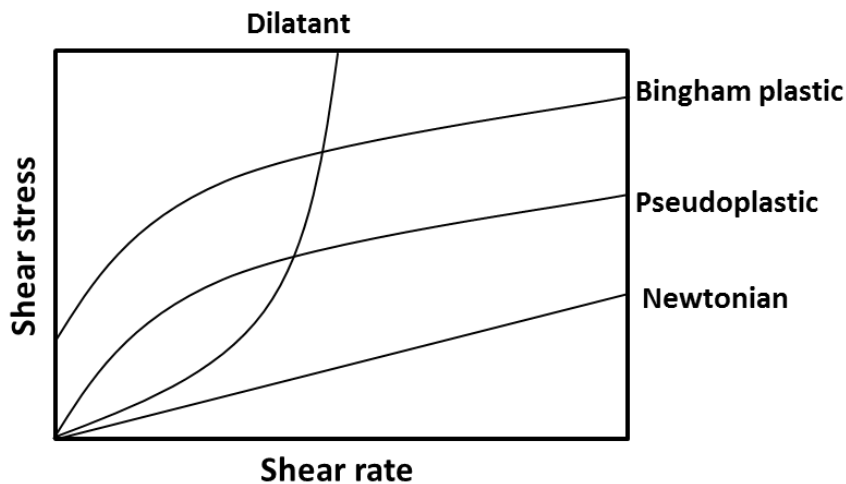


Figure 2-3 Consistency curves for four different types of flow systems

The Bingham model postulates that a finite stress should be applied to initiate flow and the flow will become Newtonian at greater stresses. Hence, the resistance of the fluid suspension to flow can be set as two regimes; i) a Newtonian regime in which the shear stress is proportional

to the shear rate and ii) a non-Newtonian regime in which the shear stress is constant regardless of the increase in shear rate. The Bingham model is expressed as follow:

$$\tau = \tau_B + \eta_{pl}\dot{\gamma} \quad (2.2)$$

where, η_{pl} is the plastic viscosity, which is determined by the slope of the curve, and τ_B is the Bingham yield stress estimated from the intercept of the flow curve at high shear rate. The other models describing the rheological behavior of clay suspensions are the Casson equation [139]

$$\tau^{1/2} = k_0 + k_1\dot{\gamma}^{1/2} \quad (2.3)$$

and the Herschel-Bulkley equation [140].

$$\tau = \tau_y + K\dot{\gamma}^n \quad (2.4)$$

where yield stress is τ_y , flow consistency is K , and flow behavior indices are n . Both models have been employed to provide a description to the consistency curves of the clay based fluids [141]. In both cases, the given suspension has an initial yield stress at low shear rates. As shear rates increases to high regime, flow behavior of the suspension exhibits shear thinning type behavior leading to a decrease in viscosity.

2.2.2.2 Viscoelastic behavior – oscillatory shear

An applicable way to investigate particle-particle interaction in clay suspension is to confirm viscoelastic behavior [133]. Among the various measurements for the rheology test, this approach is affordable to obtain qualitative information on interparticle interactions including the gel strength of clay suspensions, the gelation mechanism, and the possible structures that are formed in the suspensions. Oscillatory experiments are used to monitor the viscoelastic behavior of clay suspensions. This test allows measuring the response of viscoelastic materials to small amplitude oscillatory shear. When small amplitude sinusoidal oscillation is applied to the system, stress and strain can be measured simultaneously. By measuring the time lag of frequency Δt , it is feasible to attain the phase angle shift δ :

$$\delta = \Delta t\omega \quad (2.5)$$

where ω is the frequency in radians per second, which is given by:

$$\omega = 2\pi\nu \quad (2.6)$$

where ν is the frequency in terms of Hertz.

In oscillatory shear, a complex shear modulus G^* is described through the equation:

$$\tau(t) = G^*(\omega)\gamma(t) \quad (2.7)$$

where G^* is a function of the oscillation frequency ω . For an applied oscillatory strain, the stress will possess a similar form, but its phase will be in advance of the strain by an angle of δ .

Equations in this case are:

$$\gamma(t) = \gamma_0 \exp(i\omega t) = \gamma_0 \sin \omega t \quad (2.8)$$

$$\tau(t) = \tau_0 \exp[i(\omega t + \delta)] = \tau_0 \sin(\omega t + \delta) \quad (2.9)$$

where γ_0 and τ_0 are the amplitude of the imposed strain and the amplitude of the sensed stress, respectively. In a complete elastic system, the stress is exactly in phase with the strain ($\delta=0$), while in a complete viscous liquid, it is exactly out of phase with the strain ($\delta=90^\circ$). For a viscoelastic system, the phase angle shift lies on a certain point between elastic and viscous systems. From the equations above, the following relations can be derived;

$$G' = |G^*| \cos \delta \quad (2.10)$$

$$G'' = |G^*| \sin \delta \quad (2.11)$$

$$G^* = G' + iG'' \quad (2.12)$$

where $i = \sqrt{-1}$

G' and G'' represent the storage modulus and loss modulus that corresponds to elastic and viscous response, respectively. The storage modulus G' indicates a part of modulus in phase with strain and this physically means elastically stored energy during a deformation. The loss modulus is attributed to the modulus that is out of phase with the strain and implies a measure of the

dissipated energy in a cycle of deformation. Figure 2-4 gives a typical small amplitude oscillation result of a viscoelastic fluid system.

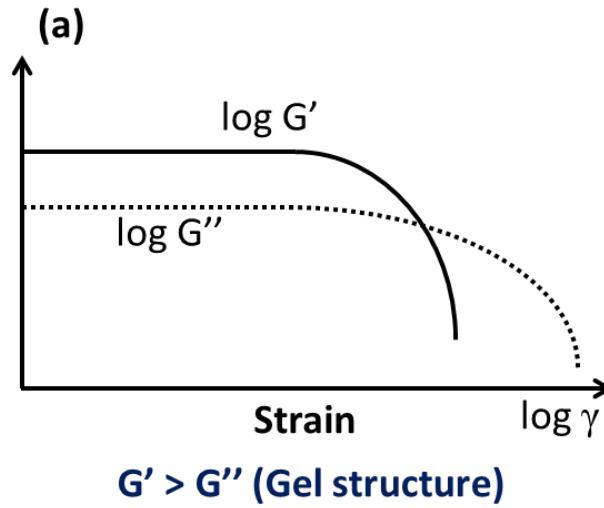


Figure 2-4 Measurements of viscoelastic behavior in small amplitude oscillatory method

In the strain regime with $G' > G''$, the given fluid system has gel-like behavior, while in the strain regime showing $G' < G''$, it exhibits liquid-like behavior. The small amplitude oscillation experiment also provides a transition point from gel-like to liquid-like behavior of a viscoelastic fluid system ($G' = G''$).

2.3 EMBEDDED CLAY HYBRID NANOPARTICLES

2.3.1 Sample preparation

2.3.1.1 Materials and chemicals

Na⁺ - montmorillonite (Kunipia F, Kunimine Corp.) was used as starting material to fabricate metal oxide nanoparticle-clay hybrid particles. The chemical formula of Kunipia F is $\text{Na}_{0.35}\text{K}_{0.01}\text{Ca}_{0.02}(\text{Si}_{3.89}\text{Al}_{0.11})(\text{Al}_{1.60}\text{Mg}_{0.32}\text{Fe}_{0.08})\text{O}_{10}(\text{OH})_2 \cdot n\text{H}_2\text{O}$, and its cation exchange capacity (CEC) is 100 mequiv/100 g. Embedded nanoparticles were synthesized from $\text{FeCl}_3 \cdot 6\text{H}_2\text{O}$, $\text{AlCl}_3 \cdot 6\text{H}_2\text{O}$, $\text{Si}(\text{OC}_2\text{H}_5)_4$, and NaOH, which were obtained from SigmaAldrich and J.T. Baker. Aqueous clay fluids, were prepared by mixing hybrid particles and bentonite ($\text{H}_2\text{Al}_2\text{O}_6\text{Si}$, CAS 1302-78-9, SigmaAldrich).

2.3.1.2 Synthesis of nanoparticle-clay hybrids

In this study, two different types of nanoparticle clay hybrid particles were prepared through the intercalation of metal polycations into the interlayer space of the clay and the subsequent thermal annealing. A detailed synthesis process of the hybrid particles is as follows.

Iron oxide clay hybrid (ICH) particles

Iron oxide clay hybrid (ICH) particles were synthesized following the procedure that was precisely described elsewhere [110]. Fe polycation solution was prepared by dissolving an aqueous solution of 0.2 M $\text{FeCl}_3 \cdot 6\text{H}_2\text{O}$ and that of 0.4 M NaOH at 70 °C. An intercalation process was carried out by mixing Fe polycation solution with Na^+ -montmorillonite at 70 °C to intercalate Fe polycations into the interlayer space of Na^+ -montmorillonite. The resulting particles were collected and excessive polycations on the surface were washed out with D.I. water several times. The hybrids were then dried and subsequently annealed at 450 °C in an atmosphere of N_2 to fully transform intercalated Fe polycations into embedded iron oxide nanoparticles.

Aluminosilicate nanoparticle-clay hybrid (ASCH) Particles

We also prepared the hybrid particles in which aluminosilicate nanoparticles were embedded into the interlayer space of Na^+ -montmorillonite (Al_2O_3 - SiO_2 clay hybrid (ASCH) particles). An Al polycations solution was prepared by slowly mixing an aqueous solution of 0.2 M $\text{AlCl}_3 \cdot 6\text{H}_2\text{O}$ and 0.2M NaOH. The molar ratio of $\text{OH}^-/\text{Al}^{3+}$ in the Al polycation solution was 2 [142]. The mixture solution was stirred vigorously for 24 h at room temperature and mixed with $\text{Si}(\text{OC}_2\text{H}_5)_4$ to prepare the aqueous hydroxy silico-aluminum polycation solutions in which the molar ratio of Al/Si is 1. These hydroxy silico-aluminum polycations were mixed with the Na^+ -montmorillonite to intercalate the prepared polycations into the interlayer space of Na^+ -montmorillonite. After the intercalation process, the hybrid particles were washed, freeze-dried, and thermally annealed at 400 °C in a N_2 atmosphere to fully convert the polycations into the aluminosilica nanoparticles.

2.3.2 Characterization

2.3.2.1 Characterization of hybrid particles

To examine the effect of the hybrid particles on the rheological properties of clay-based fluids, we prepared the aqueous clay fluids by dispersing bentonite and hybrid particles in D.I. water. In aqueous fluids containing particle suspensions, bentonite (Aldrich, USA) was selected as a main clay component. After the solid particles were poured into D.I. water, the suspensions were agitated for 30 min by a mechanical stirrer and were subsequently sonicated for 30 min by an ultrasonic horn. All processes were performed at room temperature. Solid contents in five different fluids were (i) 5 wt % bentonite (5B), (ii) 5 wt % bentonite and 0.5 wt % ICH particles (5B-0.5ICH), (iii) 5 wt % bentonite and 0.5 wt % ASCH particles (5B-0.5ASCH), and (iv) 5 wt % bentonite and 5 wt % ASCH particle (5B-5ASCH). To control the net surface charge of the particles in the fluids, we also adjusted the pH of the fluids by adding NH_4OH or HCl (J.T. Baker).

2.3.2.2 Characterization of rheological properties

The influence of hybrid particle additives on the rheological behavior was measured by a rheometer (MCR 301, Anton paar, Austria) installed with a high-temperature, high-pressure (HTHP) cell. Measurements were performed at temperatures ranging from 25 to 200 °C and at pressures between 1 and 100 bar. In the steady state measurement, the shear rate was increased from 1 to 200 s^{-1} , the step size was 4 s^{-1} and the duration time at each step was 10 s. In order to

explore the viscoelastic properties of the fluids, a small amplitude oscillatory test was also conducted as the amplitude of the oscillatory strain was increased from 0.001% to 100% at a fixed angular frequency of 10 rad/s. Prior to the oscillatory measurement, the fluids were presheared at the shear rate of 50 s^{-1} for 300 s and aged for 5 min.

2.3.3 Results and discussions

2.3.3.1 Structure of ICH and ASCH particles

Low angle XRD patterns of as-grown hybrid particles are shown in Figure 2-5. The interlayer spacing can be estimated from the basal spacing $d(001)$ of the samples, which is determined from $(00l)$ reflections in low-angle X-ray diffraction patterns. A change in the interlayer space of the intercalated hybrids estimated by tracking the position of (001) peaks provides strong evidence for the intercalation of polycations [143]. Compared with pristine montmorillonite (Figure 2-1a), both ICH (Figure 2-1b) and ASCH (Figure 2.1c) particles show the shift of (001) peak to the lower angle. The basal distance of 0.96 nm in pristine montmorillonite, was increased to 1.94 nm in ICH and 2.05 nm in ASCH. This expansion of the interlayer space indicated that Na^+ ions in the montmorillonite were successfully replaced with larger oxide nanoparticles in the hybrid particles. XRD results showed that the size of embedded nanoparticles was about 2 nm after the intercalation process. Figure 2-6 shows high angle XRD patterns of the pristine montmorillonite and the hybrid particles. Additional reflections that appeared in ICH are indexed as the rhombohedral hematite phase ($\alpha\text{-Fe}_2\text{O}_3$). This attests to the formation of the oxide nanoparticles within the interlayer space. In the case of ASCH, no

crystalline phase appeared after ASCH particles were annealed at 400 °C. In general, it has been reported that Al_2O_3 possess a high thermal stability, which initiates phase transformation from amorphous to $\gamma\text{-Al}_2\text{O}_3$ at 500-600 °C; and some oxide materials such as SiO_2 , Cr_2O_3 , and La_2O_3 inhibit phase transformation of Al_2O_3 [144-148]. Therefore, the amorphous nature of aluminosilicate nanoparticles shows that Al and Si are uniformly mixed to form the solid solution.

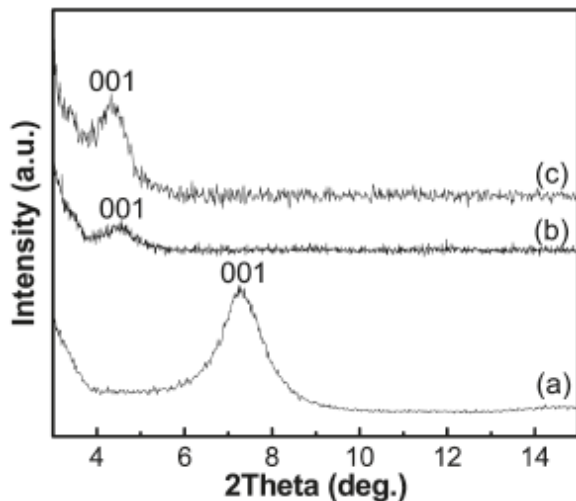


Figure 2-5 Low-angle X-ray diffraction patterns of pristine Na^+ -montmorillonite and hybrid particles; (a) pristine clay, (b) as-grown ICH, and (c) as-grown ASCH particles

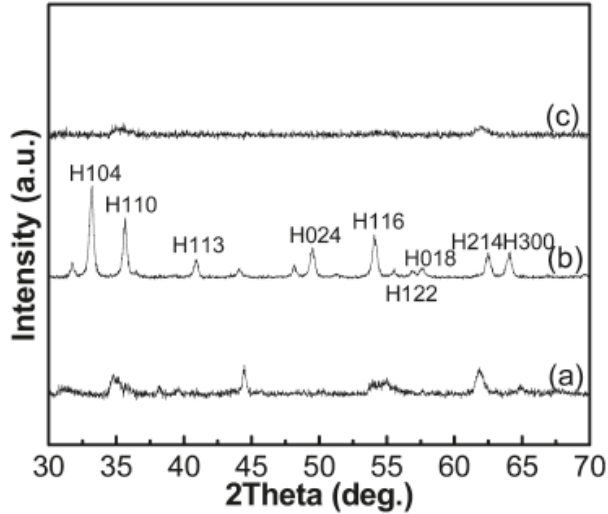


Figure 2-6 High-angle X-ray diffraction patterns of pristine Na⁺-montmorillonite and hybrid particles: (a) pristine clay, (b) 450 °C annealed ICH, and (c) 400 °C annealed ASCH particles (H: Hematite)

2.3.3.2 Microstructures of clay fluids containing hybrid particles

The effect of the hybrid additives on the formation of the clay networks was examined by analyzing the microstructure of the solid suspension. To investigate the particle network in the suspension, the fluids were quickly frozen by pouring liquid nitrogen and the frozen solids were dried at -45 °C. This process enabled us to preserve the particle network in the suspension. Figure 2-7 shows scanning electron microscope (SEM) micrographs of the freeze-dried solids. The fluid consisting of only bentonite (Figure 2-7a) has an entangled ivy-like internal structure with the irregular shape of interparticle pores. When 0.5 wt % ASCH is added to 5 wt % bentonite suspension, the zigzag type connection of the clay particles disappear and the clay particles randomly stack (Figure 2-7b). However, a very different internal structure of the solid is

found in freeze-dried 5B-0.5ICH (Figure 2-7c). Individual platelike particles were cross-linked and a relatively well-oriented pore structure was developed.

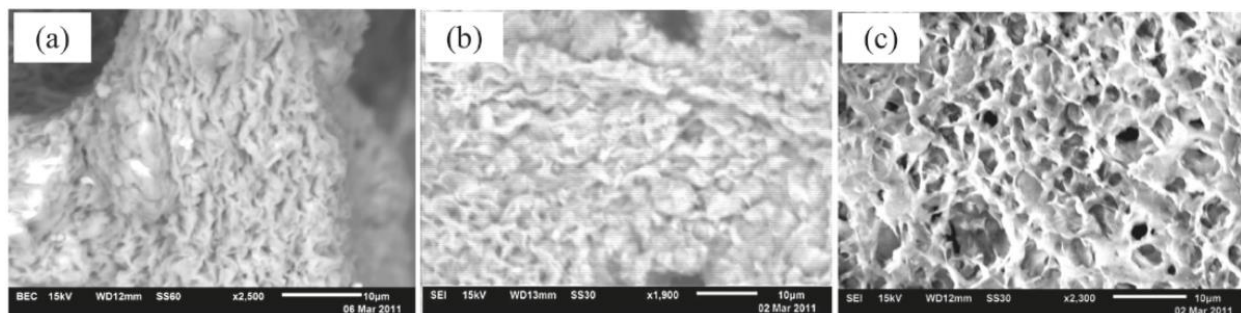


Figure 2-7 SEM micrographs of freeze-dried solids of (a) 5B, (b) 5B-0.5ASCH, and (c) 5B-0.5ICH

2.3.3.3 Effect of clay hybrid particles on the rheological properties of aqueous clay fluids

The flow behavior of any system is illustrated in terms of the relationship between the shear stress τ and the shear rate $\dot{\gamma}$. The shear stress is defined as the tangential force applied per unit area, and the shear rate is defined as the change of shear strain per unit time. The ratio of shear stress to shear rate is defined as viscosity η . In other words, η is a measure of suspension fluid's ability to dissipate momentum within a fluid flow. Correlations between shear force and shear strain in fluids can be categorized as Newtonian, pseudoplastic, Bingham plastic, Bingham, and dilatant behaviors. The Newtonian model assumes that shear stress is directly proportional to shear rate; it therefore follows that a Newtonian fluid possesses a constant viscosity, whereas the viscosity of fluids described by non-Newtonian models is dependent on the local shear rate of the

fluid. In this study, the correlation between shear stress and shear rate is explained by using the Bingham plastic behavior. The effect of the hybrid particles on the shear rate-viscosity correlation in the aqueous fluids under atmospheric pressure is presented in Figure 2-8.

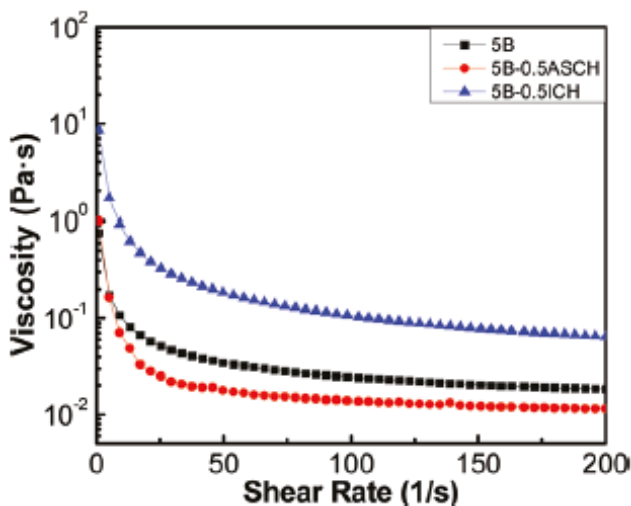


Figure 2-8 Viscosity vs. shear rate curves of the fluid samples at 25 oC under atmospheric pressure

When NH_4OH or HCl was not added to the fluid, the pH of the fluids was in the range of 8-8.5. In comparison with the reference fluid (5B), the viscosity of 5B-0.5ICH suspension increased almost by one order of the magnitude. In contrast, the addition of 0.5 wt % ASCH into 5 wt % bentonite fluid decreased the viscosity of the fluid by about 50% as the shear rate increased from 20 to 200 1/s. The change in the yield stress also attests to the opposite effect of ICH and ASCH on the rheological properties. A yield point which is a transition point to a plastic flow shows the binding strength of the coagulated clay network structure in the fluid. The shear stress at the yield point was obtained by extrapolating shear stress vs shear strain curves as illustrated in Figure 2-9.

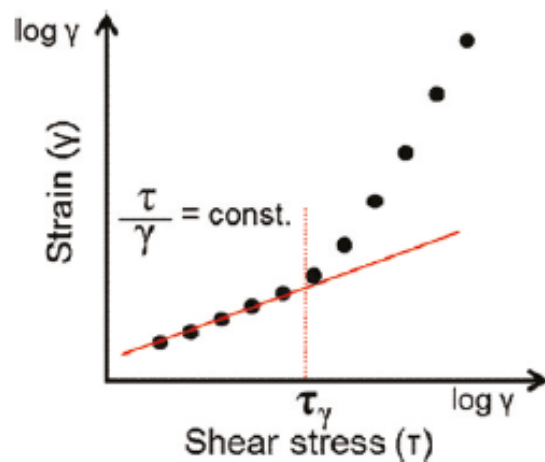


Figure 2-9 Schematic illustration of acquisition of yield point using the tangent in the linear-elastic deformation

The yield stress of 5B, 5B-0.5ICH, and 5B-0.5ASCH was 1.27, 0.98, and 12.05 Pa, respectively. The small amount of ICH additive significantly increased the yield stress, but the decrease in the yield stress was observed in 5B-0.5ASCH. High viscosity and yield stress of clay fluids are mainly due to the electrostatic attraction between negatively charged faces and positively charged edges of the platelike clay [149]. Hence, the dramatic change in the viscosity and yield stress of the fluids imply that the added hybrid particles modify the interparticle force in the clay suspension. As shown in Figure 2-7 on SEM micrographs of the freeze dried samples, the hybrid particles can develop a stable and robust gel network in the fluid. To scrutinize the interparticle interaction, the viscoelastic behavior of the fluid was measured by a small amplitude oscillatory test at a fixed angular frequency of 10 rad/s. Figure 2-10 shows the relation between storage modulus (G') and strain (ϵ). In the investigation of viscoelastic behavior of fluid systems, the storage modulus (G') and loss modulus (G'') represent the elastic and viscous response of a

given fluid system [150]. The storage modulus related to the internal motion of material and the linear viscoelastic region that corresponds to a plateau in the $G'-\varepsilon$ curve, represents the stability of fluid system [151]. G' of 5B-0.5ICH showing a long linear viscoelastic region (LVR) was 5-6 times larger than that of 5B in the range of strain from 0.1 to 100%. In contrast, $G'-\varepsilon$ curve of 5B-0.5ASCH did not show LVR and G' continuously decreased with an increase in ε . Longer LVR in 5B-0.5ICH suggests that the addition of ICH fortifies the coagulated network structure and enhances the stability of the clay suspension. ASCH oppositely influenced on the rheological properties of the clay suspension and turned the fluid to be more viscous. This trend is also observed in the flow stress of the clay suspension.

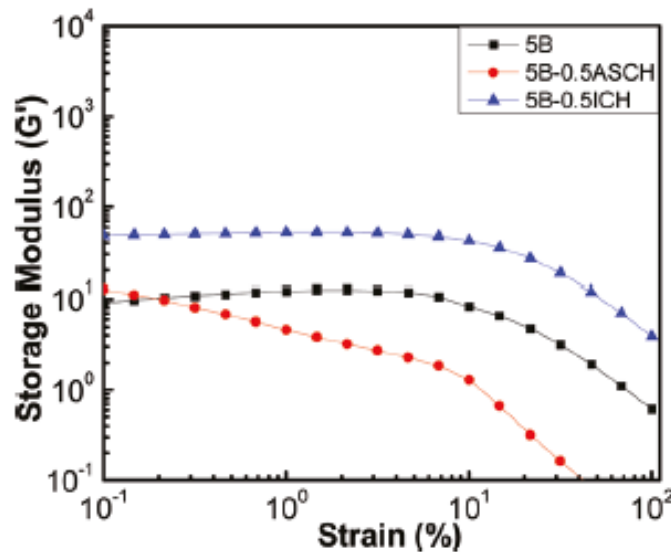


Figure 2-10 Storage modulus vs. strain amplitude curves of the fluid samples at fixed frequency (10 rad/s)

Figure 2-11 presents the change in G' and G'' plotted as a function of shear stress yielding from the amplitude oscillatory test shown in Figure 2-10. In this plot, a critical point at which the storage modulus becomes equivalent to the loss modulus is called a flow point. The shear stress at the flow point can be used in an alternative method to determine the magnitude of the external shear stress which is needed to transform the fluid from the elastic state to the viscous state [151]. Therefore, the strength of the interparticle interaction and the particle network in the fluids can be evaluated by monitoring the transition of the fluids from a solid-like elastic state to a liquid-like viscous state [152]. The flow stress increased from 1.44 Pa (5B fluid) to 8.02 Pa (5B-0.5ICH fluid). However, the flow stress for 5B-0.5ASCH was only 0.12 Pa, which is consistent with other measurement results suggesting that ACSH prevents the coagulation of the clay in the fluid and weakens the strength of the network structure.

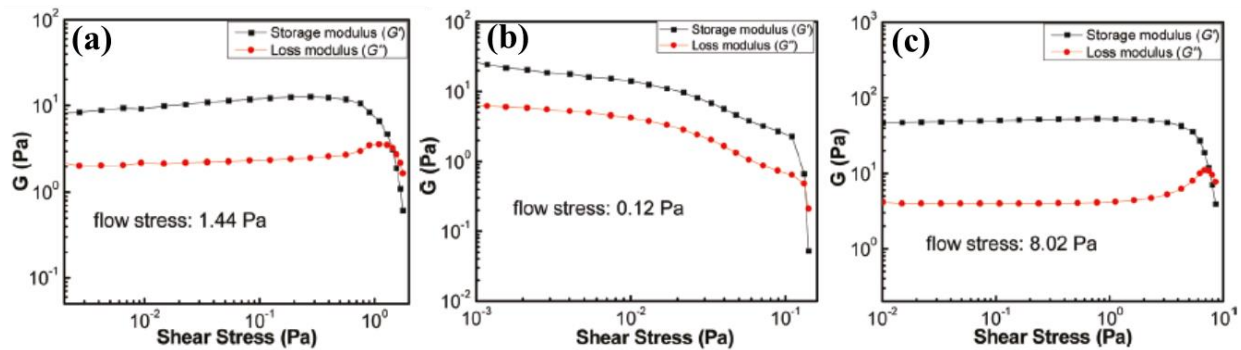


Figure 2-11 Change in storage (G') and loss modulus (G'') of fluid samples as a function of the shear stress; (a) 5B, (b) 5B-0.5ASCH, and (c) 5B-0.5ICH suspensions

2.3.3.4 Change in the viscosity of the clay fluids at high temperature and high pressure

One of the main applications of fluids containing clay particles is to control the rheology of water during the subterranean drilling. Therefore, there are interests on the change in the viscosity at the high temperature and pressure conditions found deep underground. Hence, we performed high-temperature, high-pressure studies. In addition to the properties under atmospheric pressure at 25 °C, the viscosity of the clay suspensions was measured as a function of temperature at the pressure of 100 bar. Temperature dependence of the viscosity is shown in Figure 2-12. In pure bentonite fluids above 100 °C (Figure 2-12c), the increase in the temperature increased the viscosity and yield stress of the fluid; however this effect was not found to be significant for fluids below 100 °C. This has been attributed to the fact that the change in the ionic activity at high temperature promotes the flocculation of the clay particles [153,154]. Briscoe et al. suggested that heating the bentonite suspensions increased the conductivity of the fluid system, which is attributed to rise of Na⁺ concentration dissolved from the surface of the particles. An increase in content of Na⁺ by the raise of temperature leads to increase in yield stress and viscosity of clay suspensions [96-98].

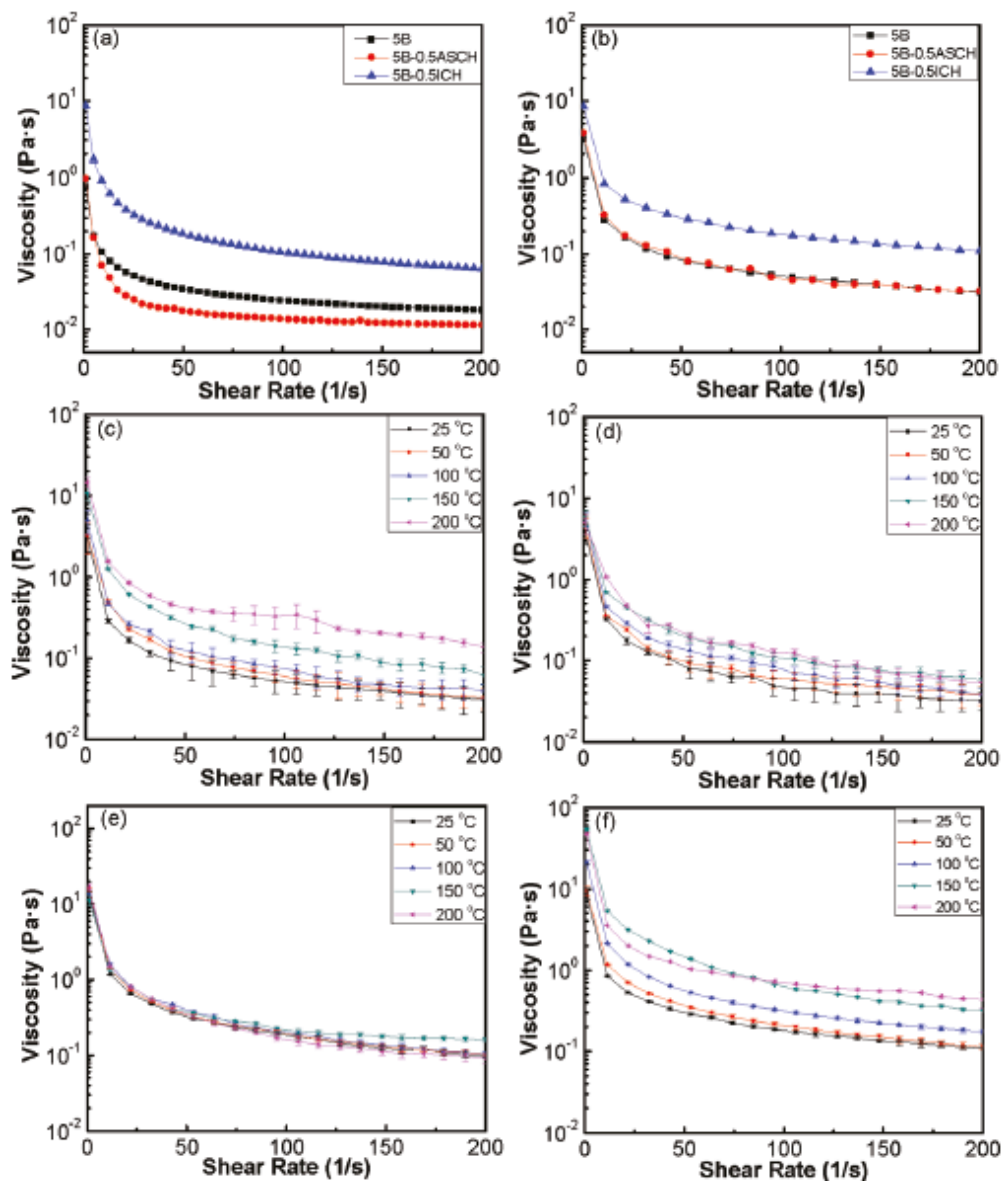


Figure 2-12 (a) 5B, 5B-0.5ASCH, 5B-0.5ICH at 25 °C, atmospheric pressure, (b) 5B, 5B-0.5ASCH, 5B-0.5ICH at 25 °C, 100 bar, (c) 5B, at 20-200 °C, 100 bar, (d) 5B-0.5ASCH, at 20-200 °C, 100 bar, (e) 5B-0.5ASCH, at 20-200 °C, 100 bar, (f) 5B-0.5ICH at 20-200 °C, 100 bar

As shown in panels (a) and (b) in Figure 2-12, the effect of high pressure is not as pronounced as that of high temperature, though the compression of the liquid media slightly increased the viscosity and yield stress of 5B and 5B-0.5ASCH [155-157]. The viscosity of 5B-

0.5ICH was primarily affected by an increase in temperature. However, the addition of ASCH suppressed the increase in viscosity and yield stress at higher temperature. To confirm the role of the ASCH additive, the amount of ASCH in the clay fluid was increased from 0.5 to 5 wt %. When the 5 wt % of ASCH was added to the 5 wt % bentonite fluid, the viscosity of the fluid was increased slightly than that of the 5B-0.5ASCH fluid, and lost its dependence on temperature. This suggests that addition of ASCH prevents the continuous gel structure of the clay and makes the clay particles well-dispersed even in the fluid of 200 °C with high ionic concentration.

2.3.3.5 Effect of pH on the rheological properties of clay fluids containing hybrid particles

The change in the rheological properties of the clay fluids implies that the hybrid additives modify the coagulation behavior of the bentonite fluid. Given that the electrostatic interactions between platelike clay particles could be mainly affected by pH variation, we examined this hypothesis by varying the pH of the fluids. The viscosity and yield stress of the fluids were measured as a function of pH; the results are summarized in Figure 2-13 and Table 2-1. Compared to pure bentonite and ICH fluids, the viscosity and yield stress of ASCH fluid are strongly depended on the pH of the fluid. Their viscosity and yield stress were larger at pH 5 than at pH 8 and 10 by more than one order of magnitude.

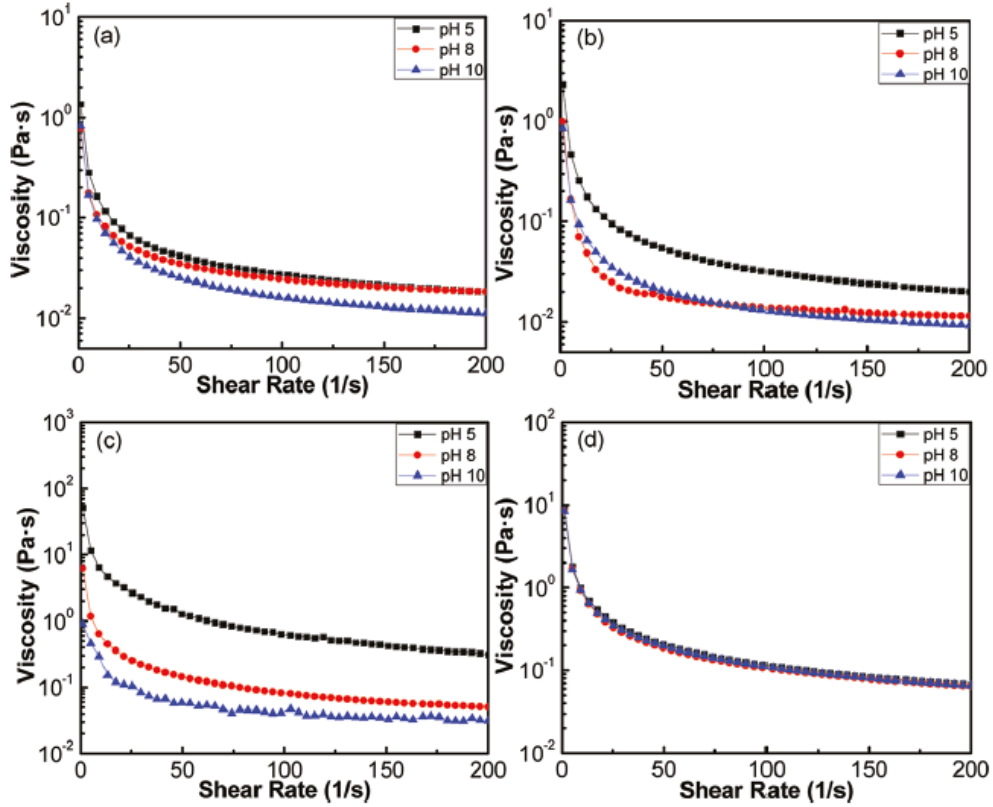


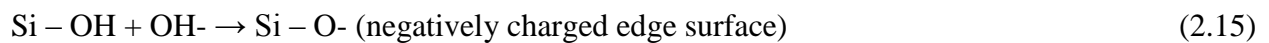
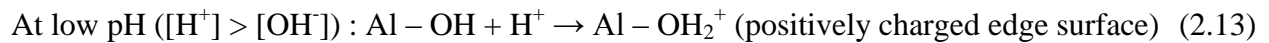
Figure 2-13 Viscosity vs. shear rate curves of the fluid samples with respect to change of pH: (a) 5B, (b) 5B-0.5ASCH, (c) 5B-5ASCH, and (d) 5B-0.5ICH suspensions

Table 2-1 Variation of yield stress of the prepared fluid samples with respect to change of pH

Fluids samples	Yield stress (Pa)		
	pH5	pH8	pH10
5B	1.52	1.27	1.20
5B-0.5ASCH	2.91	0.98	0.91
5B-5ASCH	67.51	7.69	4.32
5B-0.5ICH	11.07	12.05	10.58

2.3.3.6 Evolution of different surface charge on hybrid additives

The association of the platelike clay in water is attributed to the evolution of both positive and negative electric charges on the surface of the clay in fluids. The surface charge distribution of plate-like montmorillonite (or bentonite) consists of permanent negative charge at the face (charge-invariable) and pH-dependent positive charge at the edge (charge-variable). On the edge of platelets, the layers of octahedral Al-OH and tetrahedral Si-OH groups have broken links and dangling bonds at the end [137]. The broken links are amphoteric sites, because variable charges are conditionally developed at the edge. Concentrations of H^+ or OH^- which depend on the pH of the aqueous fluids determine the polarity of the broken links. The evolution of the charge at the edge of the platelets under different pH is expressed as follows



A question of the interest is how the intercalation of the oxide nanoparticles changes the charge distribution of the hybrid particles. To inspect the variation in surface charge with respect to pH, we investigated the zeta potential of bentonite, ICH, and ASCH in 1mM KCl electrolyte as a function of pH. Zeta potential can be utilized to estimate the effect of the particle charge on such as aggregation, flow, sedimentation, and filtration behaviors and also can be used to evaluate the effects of various reagents on the properties of the colloid suspension [158]. Generally, colloidal particles with $|\text{zeta potential}| > 30 \text{ mV}$ are considered stable. The results are

shown in Figure 2-14. The zeta potential of the platelet clay particles is a net surface charge, which is determined by a difference between the negative face charge and positive edge charge [158]. $\text{Al}_2\text{O}_3\text{-SiO}_2$ clay hybrid particles became more negatively charged in higher pH, which is in good agreement with eqs 1-3. In comparison, the negative charge of iron oxide clay hybrid particles exhibited marginal variation in a given pH range. The zeta potential of ASCH particles showed a dramatic decrease with an increase in pH and saturated at about -45 mV in $\text{pH} \geq 8$. This variation can be explained by the surface charge of $\text{Al}_2\text{O}_3\text{-SiO}_2$ nanoparticles embedded within the interlayer of montmorillonite [159]. The surface charge of $\text{Al}_2\text{O}_3\text{-SiO}_2$ nanoparticles stays negative at $\text{pH} > 2$. This negatively charged surface of embedded $\text{Al}_2\text{O}_3\text{-SiO}_2$ nanoparticles makes the overall charge of ASCH particles to be more negative than that of pure montmorillonite particle. When Fe_2O_3 nanoparticles were intercalated, the surface charge of ICH particles became much more positive than that of ASCH particles in whole range of pH. This is attributed to the high isoelectric point (IEP) of Fe_2O_3 nanoparticles. Because the surface of Fe_2O_3 nanoparticles is positively charged in water, the edge of ICH particles is positive even at $\text{pH} \sim 8$, where pure montmorillonite shows the negative charge at the edge surface. These results suggest that the surface charge of oxide nanoparticles intercalated within the interlayer of the clay particles has an important effect on the net charge of the hybrid particles through changing the charge at the edge surface.

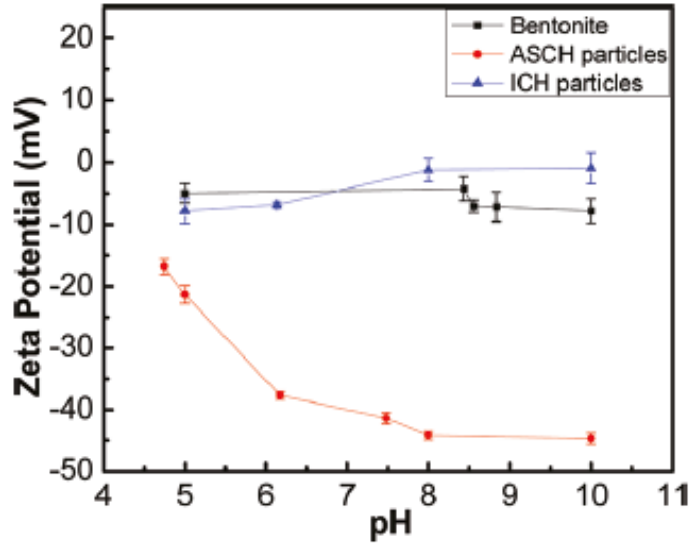


Figure 2-14 Variation of zeta potential of bentonite, ASCH, and ICH particles as a function of pH

2.3.3.7 Role of the surface charge of hybrid additives on the gel structure of the clay fluids

Differences in the net surface charge and pH dependence of the hybrid particles explain the role of the hybrid particles as rheology controlling additives in the aqueous bentonite fluids. The association of the clay platelets in the fluids occurs through several modes: edge-to-face (E-F), edge-to-edge (E-E), and face-to-face (F-F) flocculation [160]. The F-F type association that brings about the precipitation of thick clay flakes weakens the gel strength because of (i) the decreased number of the clay particles that participate in constructing the gel structure and (ii) the decreased surface area of aggregate that is necessary for interplatelet interactions. In contrast, the E-F and E-E association of platelets promote the gel-like structure and form the three-dimensional voluminous “house-of-card” structure within the fluid [149]. A correlation between

the zeta potential and the viscosity in hybrid particle added bentonite fluids reveals that more negatively charged edge surface of the hybrids lowers the viscosity of the aqueous fluids. As shown in 5B-0.5ICH, the development of the positive charge at the edge surfaces that is manifested by the increase in the net surface charge increases the viscosity and yield stress of the fluid. The positively charged edges of the hybrid additives produce attractive interactions with the negatively charged face of the bentonite, leading to the construction of the three-dimensional 'house-of-card' structures. However, more negatively charged edges of the hybrids generate a repulsive force between hybrid and bentonite particles and consequently prevent the coagulation and the network structure formation in the bentonite fluid. As illustrated in Figure 2-15, this repulsive interparticle force between negatively charged surfaces reduces both viscosity and yield stress, as shown in 5B-0.5ASCH at pH 8 and 10. For ICH particles, the variation of zeta potential at pH 5-10 was marginal and the stabilized positive charge at the edge surfaces strengthens E-F association. This explains the internal microstructure of 5B-0.5ICH showing the well-developed porous network that is the origin of its high viscosity and yield stress.

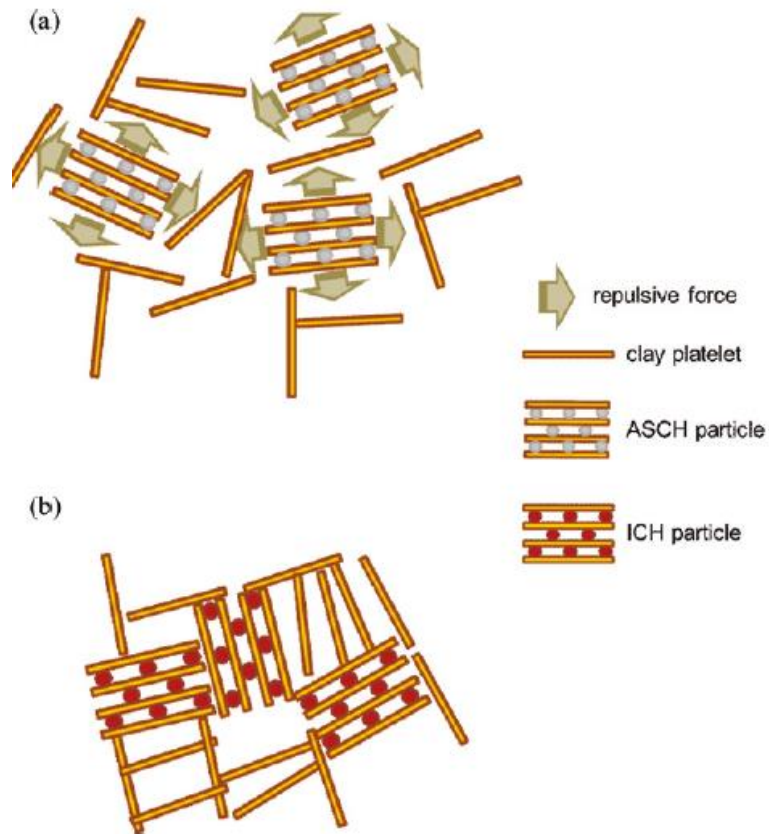


Figure 2-15 Schematic illustration of (a) particles association in 5B-0.5ASCH and (b) "house-of-card" structure in 5B-0.5ICH fluid

2.4 IRON OXIDE NANOPARTICLES DECORATED CLAY

2.4.1 Sample preparation

2.4.1.1 Materials synthesis

Na⁺-montmorillonite (Kunipia F, Kunimine Corp) was used as a starting clay material. It has the chemical formula $\text{Na}_{0.35}\text{K}_{0.01}\text{Ca}_{0.02}(\text{Si}_{3.89}\text{Al}_{0.11})(\text{Al}_{1.60}\text{Mg}_{0.32}\text{Fe}_{0.08})\text{-O}_{10}(\text{OH})_2 \cdot n\text{H}_2\text{O}$ and a cation exchange capacity (CEC) of 100 mequiv/100g. FeO(OH) (Aldrich), oleic acid (Mallinckro) and 1-octadecene were used to synthesize iron oxide nanoparticles. All the chemicals were used without further purification.

Oranopilation of the clay: the Na⁺-montmorillonite was dispersed in water containing the cationic surfactant, cetyl trimethylammonium bromide (CTAB) at room temperature. The weight ratio of the montmorillonite/water was 1:50 and the amount of CTAB was calculated to completely exchange cations in the montmorillonite. The temperature of the solution was then increased to 80 °C, and the solution was vigorously stirred for 4 h. The resulting CTAB intercalated clay was filtered and washed several times with distilled water before being dried at 60 °C in a vacuum for 24 h. Then the agglomerated particles were ground with a mortar.

Synthesis of the Fe₂O₃ nanoparticles [161]: Magnetite nanoparticles were synthesized in a three-neck flask equipped with a condenser, magnetic stirrer, thermocouple and heating mantle. A mixture of 0.178 g FeO(OH) fine powder (2.00 mmol), 2.26 g oleic acid (8.00 mmol) and 5.00

g 1-octadecene was heated to 320°C and reacted for 1 h during vigorous stirring. The resulting oleic acid coated iron oxide nanoparticles were collected by centrifugation and were then washed several times with ethanol (EtOH). The residual liquid was frozen and sublimed at -50 °C in a vacuum for 24 h.

2.4.1.2 Fluid preparation and characterization

Preparation of the magnetic fluid: The oleic acid coated magnetite nanoparticles were attached to the surface of organoclay plates in mineral oil. First, 0.5g of the organoclay powder was slowly added to 20ml mineral oil, and the mixture was sonicated to exfoliate organoclay. The resulting exfoliated organoclay plates were well dispersed in the mineral oil and 0.5g oleic acid coated magnetite nanoparticles were added into the solution of exfoliated organoclay. The mixture was then sonicated for 1h to promote the attachment of the magnetite nanoparticles to the surface of the organoclay.

The shape and crystal structure of the synthesized materials were characterized using x-ray powder diffraction (XRD, a Philips PW 1810 diffractometer with Cu K α radiation, $\lambda=1.542\text{\AA}$, 40 kV, 30 mA), transmission electron microscopy (TEM, Jeol 200CX), and photocorrelation spectroscopy (PCS) (Horiba LB 550). The magnetic properties of the materials were measured using a vibrating sample magnetometer (VSM, LakeShore 7400). Rheology measurements of the particle dispersed fluid were performed by a rheometer (Anton Parr, MCR 300) with a magnetorheological cell. To examine the effect of a magnetic field on the rheology of the fluids, a homogeneous magnetic field was set perpendicular to the direction of shear flow during the rheology measurement.

2.4.2 Results and discussions

2.4.2.1 Characterization of structure, morphology, and magnetic property of prepared nanoparticle-clay composite

Figure. 2-16 shows the x-ray diffraction (XRD) patterns for the pristine clay; the organoclay, that is, the clay intercalated with CTAB; and the nanocomposite clay, that is, the organoclay decorated with magnetic nanoparticles. When the CTAB molecules were dissociated in water, cetyl trimethylammonium cations replaced the alkali or alkali earth cations within the interlayer space of montmorillonite [162]. Hence, the (001) reflection of the montmorillonite phase shifted from $2\theta = 7.2^\circ$ to $2\theta = 5.9^\circ$. The basal spacing along the c-axis was calculated to be 12.4 \AA for pristine clay and 14.8 \AA for the CTAB treated organoclay using the XRD patterns. An inset shows the XRD pattern of nanoparticle decorated organoclay. The reflections of the magnetite in the XRD pattern of the nanocomposite clay indicate that iron oxide nanoparticles were well bonded to the organoclay via attractive interaction between hydrophobic nanoparticles and the organoclay. Since the basal spacing of organoclay ($\sim 1.5 \text{ nm}$) is much smaller than the diameter of magnetite nanoparticles ($\sim 7.5 \text{ nm}$), the nanoparticles mainly bonded to the surface of the exfoliated organoclay platelets.

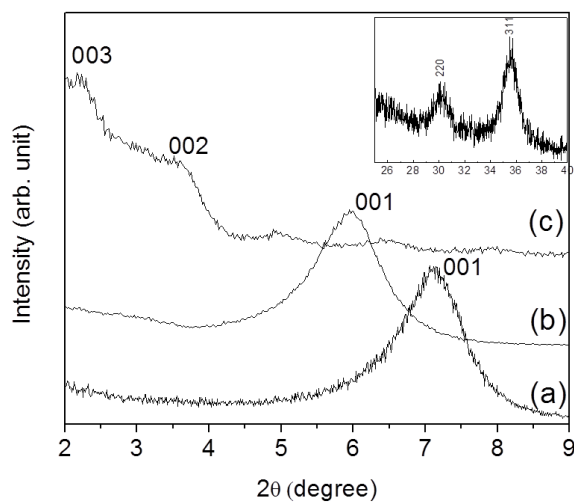


Figure 2-16 XRD patterns of (a) pristine clay, (b) CTAB-treated clay (organo clay) and (c) CTAB-treated clay and OA-treated iron oxide nanoparticles. The inset shows XRD pattern in the range of 30-40 (2theta) from (c)

Figure 2-16(a) and (b) show the TEM micrograph and particle size distribution of the OA-treated iron oxide nanoparticles. Spherical nanoparticles show a uniform size distribution, with a mean diameter of 7.5nm. Fig. 2-16(c) provides a TEM micrograph of the pristine clay where 2-dimensional layers of exfoliated clay are found. To observe the microstructure of the iron nanoparticles and organoclay, we carried out HT-TEM observation of a cross-sectional image. Fig. 2-16(d) shows a lattice image of the exfoliated clay 4nm in size and the nanoparticles 7nm in size.

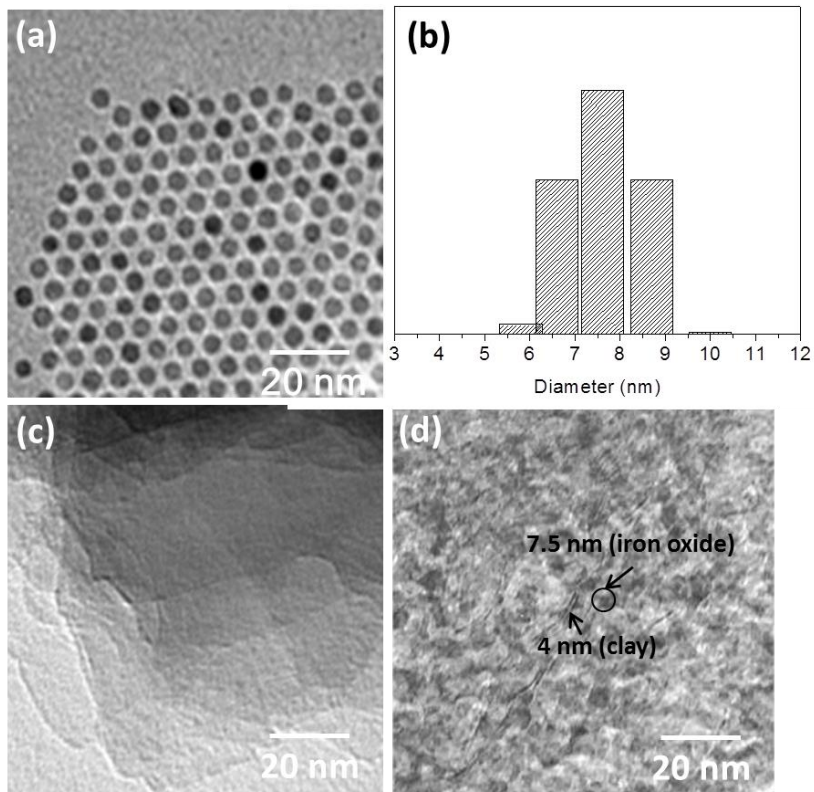


Figure 2-17 TEM images and particle size distribution: (a) OA-treated iron oxide, (b) size distribution of OA-treated iron oxide, (c) pristine clay, and (d) OA-treated iron oxide and CTAB-treated clay

Photographs of the oil based fluids containing the three different particles (CTAB treated organoclay, OA treated magnetite nanoparticles, and magnetite nanoparticle decorated organoclay) and schematics of the structure of the particles dispersed in the fluid are shown in Figure 2-18. All of the particles were well dispersed in the mineral oil, with no segregation over a 30-day period.

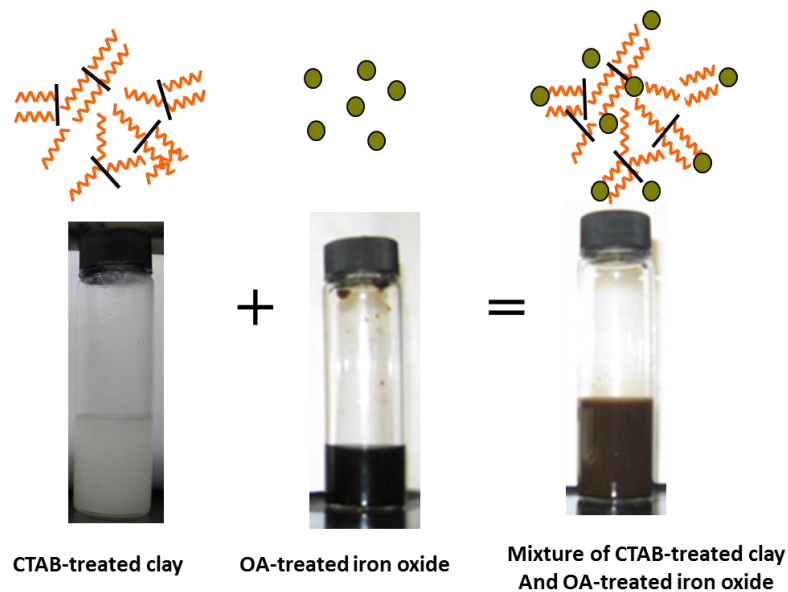


Figure 2-18 Sample image for fluids containing modified particles in mineral oil and their microstructure from the TEM

Figure 2-19 shows the M-H curves of the iron oxide nanoparticle decorated organoclay. Its saturation magnetization (σ_s) was 42 emu g^{-1} , which is half the saturation magnetization of magnetite ($\sim 80 \text{ emu g}^{-1}$) [163,164]. This indicates that the magnetite content in the composite is about 50 wt%. The coercive field of the composite material in the inset of Figure 2-19 is almost zero, which agrees well with a well-known very small coercive field of the magnetite nanoparticles [165,166].

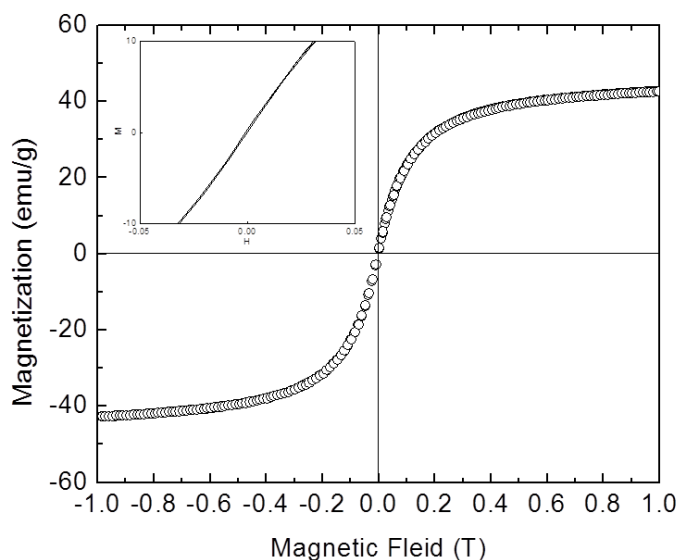


Figure 2-19 Magnetic property of heterostructured sample of OA-treated iron-oxide and CTAB-treated clay

2.4.2.2 Magnetorheological property of iron oxide nanoparticle decorated organoclay fluid

The rheological properties of the mineral oil based fluids containing 1 wt% OA treated magnetite nanoparticles, CTAB treated organoclay, and magnetite nanoparticle - organoclay mixture were also measured. In Figure 2-20, the viscosity and shear stress of the fluids are plotted as a function of shear rate. Both the CTAB treated organoclay fluid and magnetite nanoparticle - organoclay mixture fluid show thixotropic behavior. Specifically, viscosity dramatically decreased as shear rate increased. In contrast, the fluid containing 1wt % OA-treated iron oxide nanoparticle exhibited typical Newtonian fluid behavior, where viscosity is independent of shear rate. When the shear rate was 80 1/s and temperature was 25 °C, the

viscosity was 12 cp for 1wt % OA-treated iron oxide nanoparticle, 26 cp for 1wt% CTAB-treated clay and 38 cp for 1 wt% nanoparticle decorated organoclay.

The dramatic change in viscosity as shear rate increased shows that the organoclay and nanoparticle decorated organoclay interconnected to form a network structure in mineral oil. The network formation and breakdown in the fluids are more quantitatively explained by measuring shear stress vs. shear rate relation. Shear stress curves in Fig. 2-20(b) consist of two different regimes. When the shear rate was smaller than 85 1/s, the slope of the shear stress – shear rate curves was larger for the nanoparticle decorated organoclay fluid and the bare organoclay fluid than for the magnetite nanoparticle fluid. The higher stress needed to produce the shear strain in the organoclay based fluids can be attributed to the unique network formation capability of the organoclay in the fluid. As the shear rate becomes larger than 85 1/s, the slope of the stress-strain curve becomes similar in all samples. Since the organoclay cannot be interconnected in a high shear rate regime, the network structure of the clay is broken and a difference in the rheological properties among three fluids becomes negligible.

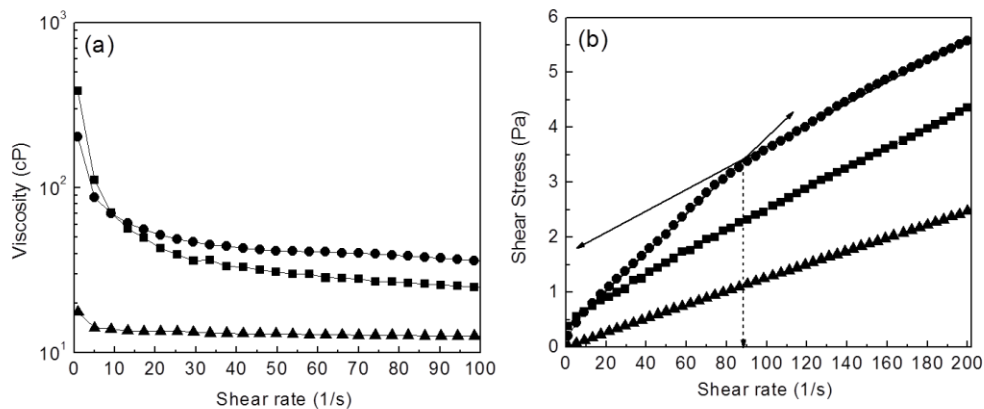


Figure 2-20 (a) Viscosity and (b) shear stress vs. shear rate of fluid containing of (●) OA-treated iron-oxide and CTAB treated clay, (■) CTAB-treated clay and (▲) OA-treated iron oxide nanoparticles

Since the magnetic particles are strongly bonded to the clay using a chemical interaction, the clay moves with the magnetic nanoparticles when they are exposed to a magnetic field. Therefore, decorating the surface of the organoclay with magnetite nanoparticles provides the freedom to tune the rheological properties of the fluid by applying a magnetic field. In this study, the magnetorheological properties of the fluid were measured while the fluid was in an oscillating motion. This oscillatory technique is widely used in characterizing the viscoelastic properties of fluid systems [165, 167-169]. A correlation between storage modulus and strain amplitude under a magnetic field is shown in Figure 2-21 Oscillation frequency was fixed at $\omega = 5$ rad/s, and a sweeping strain ranged from 0.01% to 100%. A magnetic field of 0.38T was applied.

To investigate the effect of the strong bond of the magnetic nanoparticles to the clay, the viscoelastic properties of a fluid containing only OA-treated iron oxide nanoparticles were also examined. Application of the magnetic field increased the storage modulus of the nanoparticle decorated organoclay fluid by three times. In addition, a linear viscoelastic (LVE) behavior was

observed in the magnetic field applied fluid when the sweeping strain was small. Storage modulus of the viscoelastic fluid is related to the elastic internal motion of a solid component [169]. The nearly constant storage modulus over small strain shows that the magnetic field induced a stable network of the solid components, leading to solid-like behavior. As the shear strain increased, the elastic behavior of the solid network could not be maintained, even under a magnetic field, and the loss modulus increased. A critical point at which the storage modulus is same as the loss modulus is called the “flow point” [167]. When a magnetic field of 0.38T was applied, the flow point of the fluid containing the nanoparticle decorated organoclay moved from 10.3% to 38.1%. An increase in the flow point supports our claim that the nanoparticle decorated organoclay forms a strong network structure in mineral oil and maintains a solid-like behavior under a magnetic field.

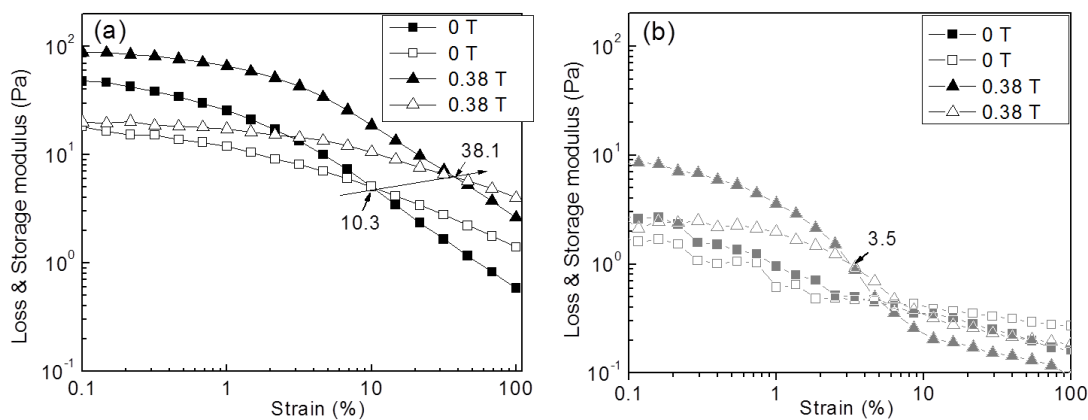


Figure 2-21 Storage modulus vs. strain amplitude of the fluids containing OA-treated iron oxide nanoparticles (a) OA-treated iron oxide and CTAB-treated clay with different magnetic field. Solid symbol represent storage modulus and open symbol are loss modulus

3.0 MIROWAVE SYNTHESIS OF 3D STRUCTURES PARTICLE

3.1 INTRODUCTION

Synthesis of intricate 3-dimensional (3D) hierarchical nanostructure materials with controlled morphology and orientation has attracted intense interest owing to their potential application in catalysis, drug delivery, energy storage, water treatment, and sensors [170-184]. Many kinds of hierarchical superstructured materials such as nano-flowers, snowflakes, and dendrites have been successfully synthesized and examined to explore their physical and chemical characteristics with respect to morphology [185-187]. In general, the simplest synthetic route to a 3-dimensional hierarchical structure is the oriented assembly of nanoparticles to decrease their surface energy by stacking nanoparticle building blocks. Therefore, it is important to develop simple and reliable synthetic method for hierarchically ordered architectures with desired morphology, which greatly acts on the properties of the final product.

Recently, a microwave reaction has been applied to chemically synthesize nanomaterials. This technique offers several advantages over other conventional techniques, such as vapor–liquid–solid (VLS), vapor phase, hydrothermal and solvothermal synthesis [188-191]. Microwave irradiation reduces reaction time and temperature, which is due to the molecular level interaction of the microwave with the reagent species [192,193]. This has allowed the preparation of highly crystalline nanomaterials with tailored shapes and sizes, such as uniform

Ag nanoparticles, microporous SnO₂, TiO₂ nanowires, CdTe nanocrystals, Cu₃Se₂ nanoplates, and iron oxide nanorings [194-199].

Fe-based magnetic nanomaterials have been intensively studied for applications of magnetic data storage devices, magnetic resonance imaging, biomedical markers, wireless sensors, water treatments, and ferrofluids [200-209]. In addition to their outstanding magnetic properties, a very unique intrinsic property of Fe-based nanomaterials is their sulfidation ability. Fe-based materials are easily converted to iron sulfide, which is used to decompose hydrogen sulfide (H₂S). Due to its toxic and flammable nature, H₂S needs to be removed from waste gas streams of chemical plants or from byproducts of oil/gas drilling operations [210,211]. Various transition metal oxide materials with high catalytic activity have been utilized in H₂S removal [212-214]. Among these materials, Fe-based materials are widely reported as strong oxidation reagents for H₂S treatment [215,216]. Several methods have been developed to synthesize Fe₃O₄ and Fe particles, which include thermal decomposition, co-precipitation, hydrothermal processing, reverse micelle, and sol-gel processing [217-221]. In comparison, the effect of microwaves on the growth of Fe₃O₄ and Fe particles with a hierarchical superstructure has not been studied yet. Herein, we demonstrate a facile microwave-assisted method to fabricate flower-like Fe₃O₄ and Fe particles. The effect of reaction parameters and annealing conditions on the morphology and phase of the particles were examined. A growth mechanism of hierarchical particles in ethylene glycol (EG)-mediated solution was proposed. Moreover, the reaction of flower-like particles with S²⁻ ions was tested to evaluate their efficacy as a H₂S absorbent in water.

In this work, utilization of flower-like Fe₃O₄ particles will be extended to controlling rheological behavior of fluid system under magnetic field. Based upon interesting fact that the

magnetic particles in solutions can be aligned when an external magnetic field is applied, we will investigate viscoelastic properties of flower-like Fe_3O_4 -containing fluid system that can be rapidly and reversibly controlled by the magnetic field. Furthermore, influence of hierarchical morphology of flower-like Fe_3O_4 particles on fluid viscosity will be addressed.

3.2 BACKGROUND

3.2.1 Principles of microwave irradiation

Microwave irradiation is a form of electromagnetic radiation within the frequency range of 0.3 - 300 GHz. A large fraction of the microwave spectrum is reserved for the utilization in telecommunication and cellular phone applications. All the domestic 'kitchen' microwave ovens and all commercially available dedicated microwave reactors for the chemical synthesis are designed to be operated at a frequency of 2.45 GHz, which corresponds to a wavelength of 12.24 cm. The microwaves are generated by a magnetron, comprised of an oscillator converting high-voltage direct current into high frequency radiation (Figure 3-1). The frequency of 2.45 GHz is selected for two reasons. The first reason is to avoid any interference with telecommunication, wireless networks and cellular phones. Second, this frequency is ideal as a kitchen microwave, since it is attainable to manufacture corresponding magnetron at low cost, and the typical penetration depth in food is in the range of a few centimeters.

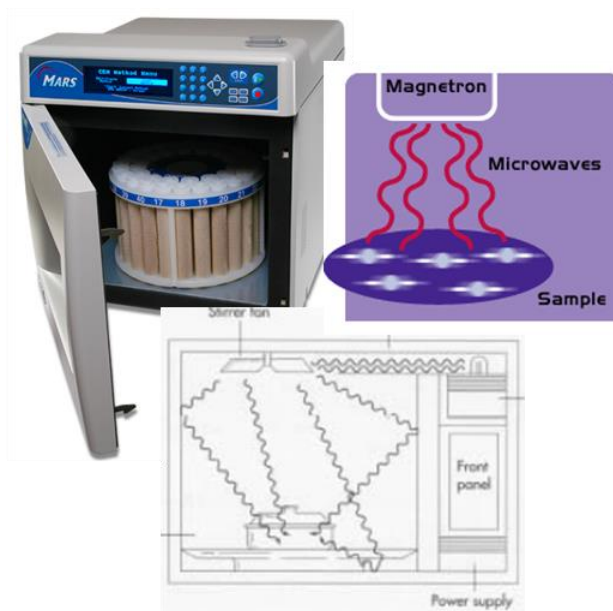


Figure 3-1 Commercially available microwave reactor for the chemical synthesis (Mars, CEM)

The wavelength λ_0 of a microwave (12.24 cm) is in correlation with the frequency (2.45 GHz) through the equation (3.1). The frequency represents the number of oscillations of the electric or magnetic field per second [222]:

$$\lambda_0 = \frac{c}{f} \quad (3.1)$$

Microwave chemistry is based on the efficient heating of matter by so called microwave dielectric heating on the ability of a specific material to absorb microwave energy and to convert it into heat [223,224]. The heating mechanism involves two main processes; i) dipolar polarization and ii) ionic conduction shown in Figure 3-2. In the dipolar polarization process, an important property is the mobility of the dipoles and the ability to align the dipoles in a response to the direction of the electric field. The orientation of dipoles is altered with an oscillating electric field. A dipole is sensitive to external electric fields, and molecules possessing a

permanent dipole moment attempt to align themselves to the field by rotation with the direction of the field. In gases, molecules are spaced far apart and their alignment is rapid, which enables the molecules to rotate in time with the applied field, while in liquid medium, the rotations of polar molecules begin to lag behind the electric field oscillations, and this leads to producing resistive heating in the medium. This phenomenon is described as dielectric loss, which is the amount of input microwave energy that is lost to the sample by being dissipated as heat [225].

If two samples, distilled water and tap water, are heated in a single mode microwave at a fixed radiation power and time, the final temperature of the tap water sample will be higher compared to that of the distilled water. This result is attributed to the second major interaction process of the electric field component with the sample, regarded as the ionic conduction. In the ionic conduction process, the dissolved charged particles migrate back and forth under the influence of the microwave irradiation and dissipate a heat by the collision with neighboring molecules, and therefore, create heat. It is noted that the ionic conduction process is a much stronger interaction than the dipolar polarization with respect to the heat-generating capacity, and this renders significant effect on synthesis of nanoparticles in ionic liquids [226].

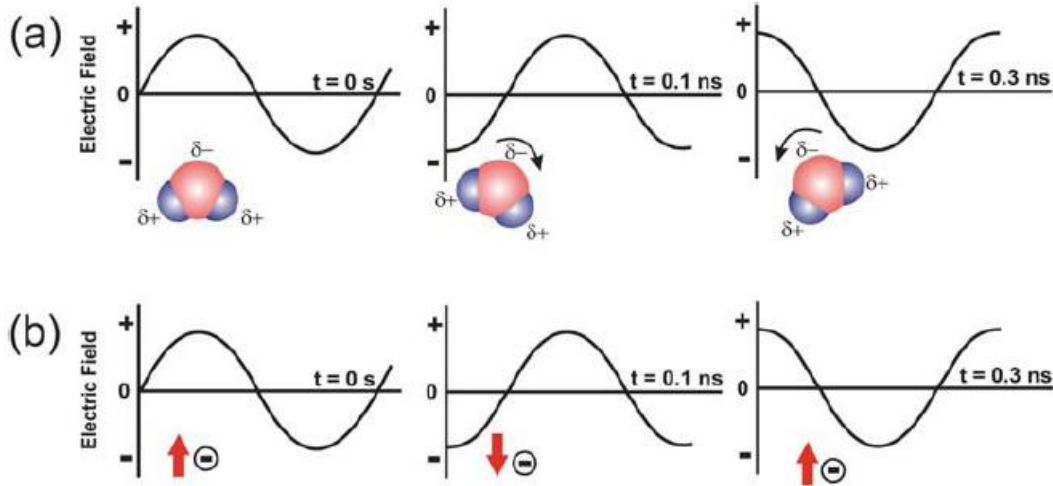


Figure 3-2 Two main heating mechanisms under microwave irradiation: (a) dipolar polarization, (b) ionic conduction mechanism [226]

The coupling of microwave energy in the medium depends on the dielectric properties of the substance to be heated. Two parameters define the dielectric properties of the substance; i) the dielectric constant ϵ' , representing the ability to be polarized by the electric field, and ii) the dielectric loss ϵ'' , describing the efficiency with which electromagnetic radiation is converted into heat [227]. Microwave heating can be described using a complex permittivity ϵ_r . A measure ϵ_r is related to the capacity C , which indicates the ability to store electric energy expressed in equation (3.2),

$$\epsilon_r = C/C_0 \quad (3.2)$$

For the electromagnetic field, ϵ_r is extended by the imaginary part $i\epsilon''$ via equation (3.3),

$$\epsilon_r = \epsilon' + i\epsilon'' \quad (3.3)$$

where $i^2 = -1$. The dielectric loss factor ε'' is derived from comparing the irradiated microwave energy to the energy coupled with the sample. ε'' depends on the dielectric conductivity σ and the frequency f ,

$$\varepsilon'' = \frac{\sigma}{2\pi f} \quad (3.4)$$

The degree of energy coupling in the reaction system can be expressed as the ratio of ε' and ε'' and is called loss factor ($\tan \delta$),

$$\tan \delta = \frac{\varepsilon''}{\varepsilon'} \quad (3.5)$$

$$\tan \delta \sim \frac{1}{x} \quad (3.6)$$

The definition of the loss factor is the ability to convert electromagnetic energy into heat at a given frequency and temperature. Furthermore, it is in correlation with the penetration depth (x) of microwave irradiation into a material as shown in equation (3.6).

According to the mechanism of energy input, dipole polarization or ion conduction, the loss factor is further affected by other factors, including the ion concentration, ion size, dielectric constant, microwave frequency, and viscosity of the reaction medium [228]. For instance, the loss factor of water and organic solvents diminishes with increase of temperature, owing to decrease in the absorption of microwave radiation in water at higher temperature. In contrast, the penetration depth of microwaves increases. Organic solvents are generally categorized in three

different groups in terms of their high, medium, and low absorbing properties. Solvents with high microwave absorbing ability typically have $\tan\delta > 0.5$, while the loss factor value of medium and low absorbing solvents is 0.1-0.5 and < 0.1 , respectively [223].

Table 3-1 Loss factors ($\tan\delta$) and dielectric constant of different solvents [229]

Solvent	$\tan\delta$	Dielectric constant	Solvent	$\tan\delta$	Dielectric constant
ethylene glycol	1.350		DMF	0.161	
ethanol	0.941	24.6	1,2-dichloroethane	0.127	
DMSO	0.825	47	water	0.123	80.4
2-propanol	0.799		chlorobenzene	0.101	
formic acid	0.722		chloroform	0.091	4.8
methanol	0.659	32.7	acetonitrile	0.062	36
nitrobenzene	0.589		ethyl acetate	0.059	6.2
1-butanol	0.571		acetone	0.054	20.6
2-butanol	0.447		tetrahydrofuran	0.047	
1,2-dichlorobenzene	0.280		dichloromethane	0.042	
NMP	0.275		toluene	0.040	
acetic acid	0.174	6.1	hexane	0.020	1.9

3.2.2 Effects of microwave heating in chemical reaction

Microwave-assisted material synthesis is characterized by the outstanding accelerations resulting from the chemical reaction involving unique heating rate, which cannot be achieved and duplicated by conventional heating. The effect of microwave irradiation in chemical reactions is classified into two separate terms which are thermal effects and non-thermal effects. Thermal effects originate from the heating rate, superheating or ‘hot spot’, and the specific microwave effect caused by the uniqueness of the microwave dielectric heating mechanisms.

Such phenomena are not usually attainable by classical heating, and thus, thermal effects have been widely accepted notion in the field of microwave synthesis. Non-thermal effects, which are still a controversial topic, are induced by the highly polarizing radiation of microwaves. This subsection will cover an overview of thermal effects and non-thermal microwave effects, and provide basic concepts for understanding these microwave-dependent effects.

3.2.2.1 Thermal effect

Table 3-2 presents the different characteristics of microwave dielectric heating and conventional heating, and the given features in microwave-dependent dielectric heating provokes so called thermal effects. Microwave heating exploits the ability of the materials to transform electromagnetic energy into heat. While the conventional heating accompanying the conduction and convection processes, in microwave heating, energy transmission is generated by dielectric losses. The magnitude of heating is dependent on the dielectric properties of the molecules, which is also dissimilar to conventional heating. These characteristics signify the speculation that radiation absorption and heating may be carried out selectively. As shown in Figure 3-3, heating through microwave irradiation is rapid and volumetric with uniform heating distribution across the whole material. In contrast, conventional heating is gradual, and initially, heating spots are more concentrated on the surface of reactors, then impart to the sample. The efficient and uniform volumetric heating with minimized thermal gradients achieved from microwave irradiation result in rapid and more spatially uniform nucleation and growth of the material [230]. These benefits innate to microwave dielectric heating have often been contemplated to be responsible for accelerating certain reactions.

Table 3-2 Characteristics of microwave and conventional heating [231]

Microwave heating	Conventional heating
Energetic coupling	Conduction/convection
Coupling at the molecular level	Superficial heating
Rapid	Slow
Volumetric	Superficial
Selective	Non-selective
Dependent on the properties of the material	Less dependent

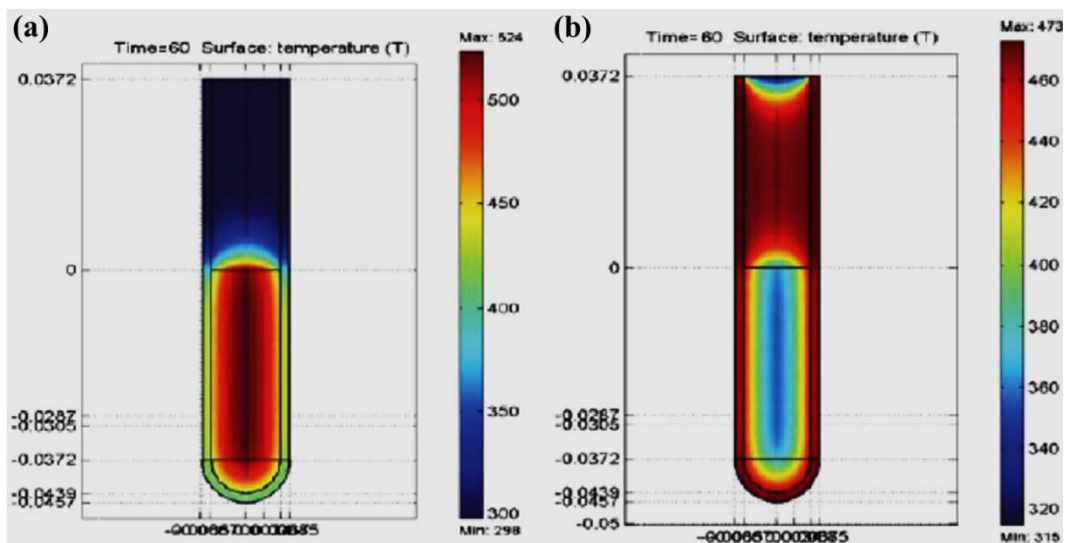


Figure 3-3 Temperature profile after 60s heated by (a) microwave irradiation, (b) conventional oil-bath treatment [232]

3.2.2.2 Heating inhomogeneity. ‘Hot-spot’

In a chemical reaction using conventional heating, crystals often tend to nucleate on a container wall and undergo a slow growth rate due to randomly spread ions, tardy and non-uniform nucleation stage, availability of few seed nuclei, and an uneven heating profile across the reaction medium [233]. In contrast, microwave dielectric heating gives rise to efficient internal volumetric heating, minimizing the tendency of wall effect [234]. Hence, it is suggested that in a microwave-assisted reaction, numerous ‘hot-spots’ probably form by volumetric dielectric heating, facilitating massive nucleation of seeds throughout the solution and this leads to overall rapid formation of the final product and higher yield.

It has been intensively studied and addressed the presence of ‘hot-spots’ in the microwave-assisted synthesis. This is a thermal effect that is attributed to the inhomogeneity of the applied electric field. The temperature in certain zones within the reaction media is much higher than the macroscopic temperature. In addition to volumetric dielectric heating, difference in dielectric properties of materials can be the driving parameter to create a ‘hot-spot’, due to the uneven distribution of electromagnetic field strength [235].

Figure 3-4 shows the $\text{Ce}^{3+}/\text{Tb}^{3+}$ co-doped LaF_3 synthesized through the microwave irradiation [233]. When microwave irradiation triggered the reaction, monodispersed nanoparticles (4.5nm) were produced. In comparison, oil-bath heating yielded the final product with broad size distribution (3-8nm). In the proposed reaction mechanism, by the microwave irradiation, fast and spatially uniform nucleation was induced in the polar liquid environment and

a uniform concentration of reactive monomers around the crystal embryos, and this, in turn, advanced subsequent growth under stable and steady conditions.

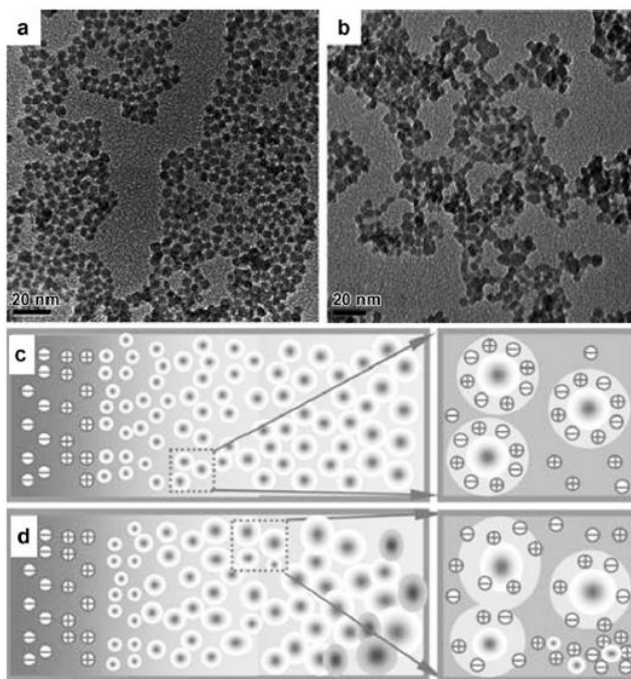


Figure 3-4 a),b) TEM images of Ce^{3+}/Tb^{3+} co-doped LaF_3 fabricated under MW and oil-bath heating, respectively [233]. c),d) Proposed mechanisms for the nucleation stage of the Ce^{3+}/Tb^{3+} co-doped LaF_3 under MW irradiation and oil-bath heating, respectively

3.2.2.3 Selective heating

In the microwave-assisted synthesis, the selective heating is defined as the ability of microwave energy to be preferentially absorbed by highly polar substrates. When a mixture compound containing different dielectric properties (loss factor, $\tan\delta$) is exposed to microwave irradiation, the substance with higher loss factor will absorb the energy preferentially and get

heated more rapidly compared to the other compound [236,237]. One example to demonstrate the selective heating is to investigate the temperature variation of the oxide particles grafted by a certain functional group, specifically hydroxide group, which has good ability to absorb microwave energy [238]. The result revealed that surface temperature of an oxide particle decorated with hydroxyl group dramatically increases, intriguing local overheating on the surface. Figure 3-5 provides another experimental demonstration on the selective heating process in the microwave-assisted synthesis of α -Fe₂O₃ nanoring [239]. The proposed formation mechanism represents microwave induced nucleation-aggregation-dissolution stages (Figure 3-5). Initially, α -Fe₂O₃ nanodisk is formed through oriented attachment process. Subsequently, the formed nanodisk is selectively heated to considerably high temperatures beyond a critical point characterizing the remaining bulk mixture. The creation of a ‘hot-spot’ on the surface of nanodisk accelerates further localized-etching by the highly polarizable phosphate ions, leading to transformation into α -Fe₂O₃ nanorings [240].

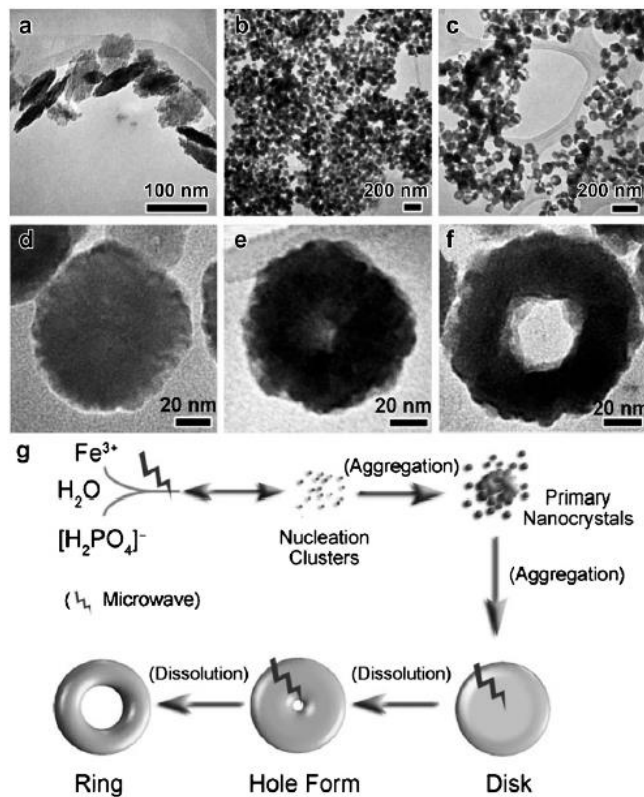


Figure 3-5 a)/d), b)/e), c)/f) TEM images showing the morphology evolution of α -Fe₂O₃ nanostructures achieved by the MW reaction [239,240] at 220 °C after (a,d) 10 s, (b,e) 50 s, and (c,f) 5 min, g)

Schematic representation of α -Fe₂O₃ nanoring formation

3.2.2.4 Non-thermal microwave effect

In addition to thermal and specific microwave effects, another possible microwave effects so called non-thermal effects have been proposed [241-245]. Basically, non-thermal microwave effects must be discerned as the rate acceleration that cannot be vindicated by thermal or specific microwave effects. Non-thermal effects are strongly related to the direct interaction of

microwave field with molecules or substances in the reaction medium, which cause no macroscopic temperature effects on the reaction path [246,247]. The main advantage of employing microwave irradiation to the materials synthesis is that the reaction time can be dramatically reduced. The rate of the reaction can be described by the Arrhenius equation as follow,

$$K = A e^{-\Delta G/RT} \quad (3.7)$$

Considering the Equation (3.7), the pre-exponential factor A describes the molecular mobility and depends on the frequency of the molecules vibrations at the reaction interface. It has been argued that the pre-exponential factor A or the free energy of activation (entropy term) can be changed by the reorientation of dipolar molecules under an electric field [248,249]. In addition, polar reaction mechanisms involves similar effects, suggesting that the polarity increases from the ground to the transition state and this brings about enhanced reactivity since the activation energy barrier decreases [250]. Bilecka et al. has experimentally validated reaction-kinetic accelerated formation of ZnO through minimizing the activation energy [251]. Further efforts to investigate this issue have been extended to estimate the influence of varying microwave frequency. Caponetti et al. and Nyutu et al. [252,253] scrutinized the effects of the microwave frequency on the final product in microwave synthesis and revealed that the size features and surface morphology of the nano crystals were all affected by the microwave frequency.

3.2.3 Mechanisms of shape anisotropic particle growth

As described in the subsection on the mechanism for the anisotropic growth of nanomaterials in Chapter 1, three representative shape controlling mechanism have been proposed and employed for understanding anisotropic particle growth. These are i) seed-mediated solution-liquid-solid (SLS) growth, ii) oriented attachment (OA) process, and iii) kinetically induced anisotropic growth. In 1D rod/wire synthesis, the main governing mechanisms for the particle growth are the oriented attachment process and selective adhesion behavior. Formation of 2D plate/disc particle can be achieved through the selective adhesion, in which capping agents participate in the reaction medium and play a crucial role in controlling the growth direction. In comparison, the particle growth mechanism for the formation of 3D hierarchical architecture is more sophisticated. The basic building blocks, including 0D spheres, 1D rods, and 2D plates, have unique geometries and natures, and self-assembly of the building blocks *via* van der Waals interaction, electrostatic, dipolar fields, hydrophobic interactions, and hydrogen bonds determine the advanced shape of the final products. The following subsections will present some selected examples to highlight the importance and versatility of the particle growth mechanism for the field of inorganic nanomaterial synthesis.

3.2.3.1 1D nanorod

Figure 3-6 represents the formation process of 1D BiPO₄ nanorod through a time-dependent reaction [254]. As shown in the figure, detailed TEM images of a series of aggregated particles at the early stage of the crystal growth indicate an oriented attachment growth. In this process, primary particles aggregate in an oriented fashion to produce a larger single crystal, or

the particles randomly aggregate and reorient, recrystallize, or undergo phase transformations to produce larger single crystals. Such growth mode possibly triggers to the formation of faceted particles, resulting in anisotropic growth if each crystallographic face possesses different surface energy [255]. In addition, it has been reported that the anisotropic growth often occurs in inorganic materials with hexagonal crystal structure, such as ZnO and CdSe [256,257]. BiPO₄ has hexagonal crystal structure, which favors anisotropic growth preferentially along the [001] direction.

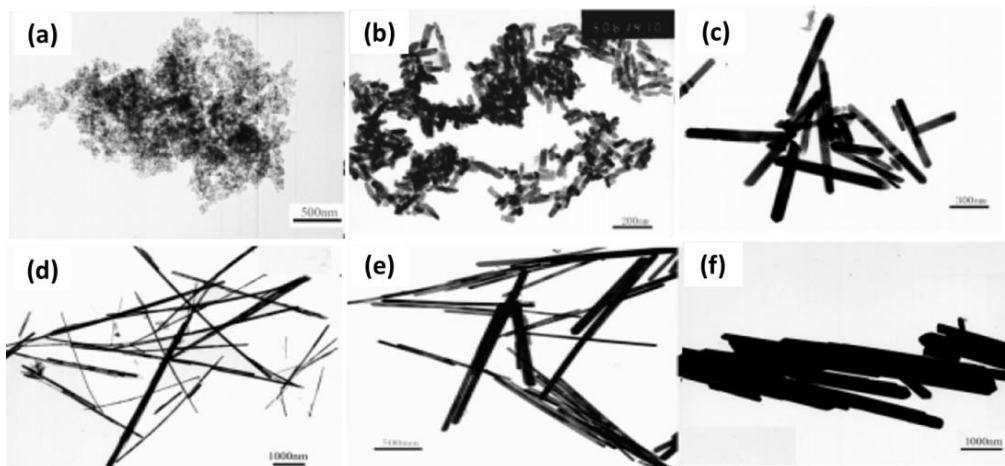


Figure 3-6 TEM images of BiPO₄ obtained after sonication for (a) 2, (b) 5, (c) 8, (d) 15, (e) 25, and (f) 60 min [254]

Investigation of 1D-anisotropic growth through combined effects of oriented attachment and selective adhesion process was performed by Liu et al. in which introduces development of Te nanorod in reaction media with a surfactant [258]. Based on the TEM observation presented in Figure 3-7, the formation of Te nanorods includes four-step growth mechanism; i) the generation of *a*-Te and *t*-Te primary nanoparticles, ii) growth of Te nanoords on the seeds of *t*-Te

nanoparticles, iii) continuous formation of Te nanorods by the expense of α -Te colloids, and iv) the formation of uniform Te nanorods through ripening process (Figure 3-8). Such an evolution process so called the solid-solution-solid transformation and the surfactant-assisted growth mechanism can be supported by the results from TEM observation. Due to the presence of surfactant in the reaction media, surfactant molecules are strongly and rapidly attached on the surface of the nanoparticles and this leads to suppressing aggregation of Te atoms, and allowing for the formation of stable colloids in a very early stage to form nascent nanoparticles. Since the 1D structure of the final products (Te nanorod) is associated with the anisotropic nature of the building blocks along the [001] direction, it could be assumed that the sidewalls, which are corresponding to {100} and {110} planes, were completely passivated by the surfactant molecules.

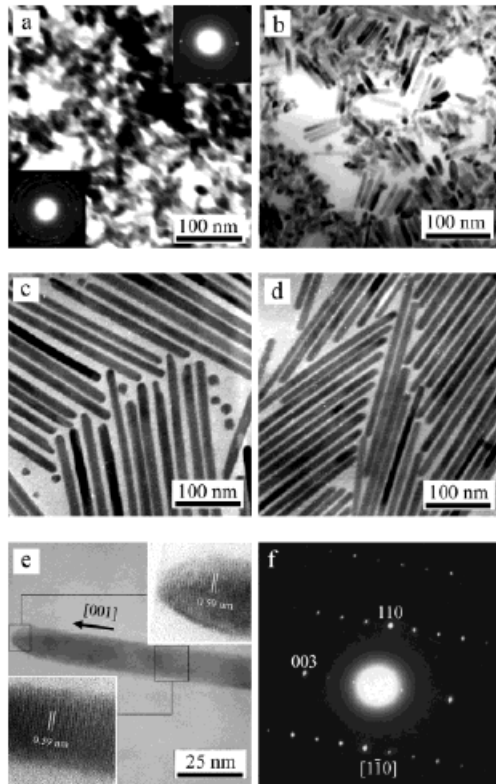


Figure 3-7 TEM images showing different stages of growth for Te nanorods after an aging time of (a) 0 min, (b) 20min, (c) 15 h, and (d) 20 h, (e) HRTEM images of an individual Te nanorod, (f) SAED pattern of nanorod, which is indexed to be the [110] of t-Te [258]

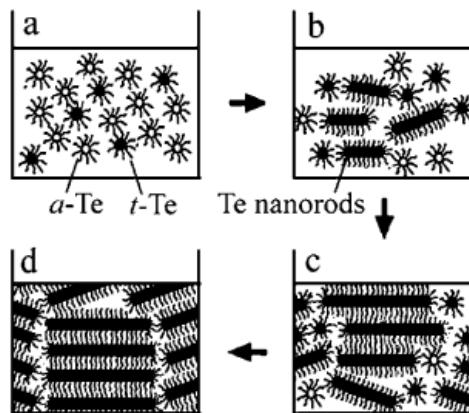


Figure 3-8 Schematic illustration of a plausible mechanism for the formation of Te nanorods via a solid-solution-solid transformation and a surfactant-assisted growth mechanism [258]

A number of groups have examined the use of strong complexing agent such as polyol to lower the hydrolysis rates of transition alkoxides [259]. Jiang et al., have employed polyol based reaction media to the 1D TiO₂, In₂O₃, and PbO nanowire synthesis and proposed anisotropic growth mechanism resulting from the formation of polymeric network [260]. According to the suggested mechanism, since glycols could serve as a ligand in the reaction mixture, chain-like coordination complexes with metal cations can be formed. As the chain-like complexes become sufficiently long, they are agglomerated into bundles and then precipitate out from the reaction media in the form of uniform nanowires which are composed of the glycolate precursor.

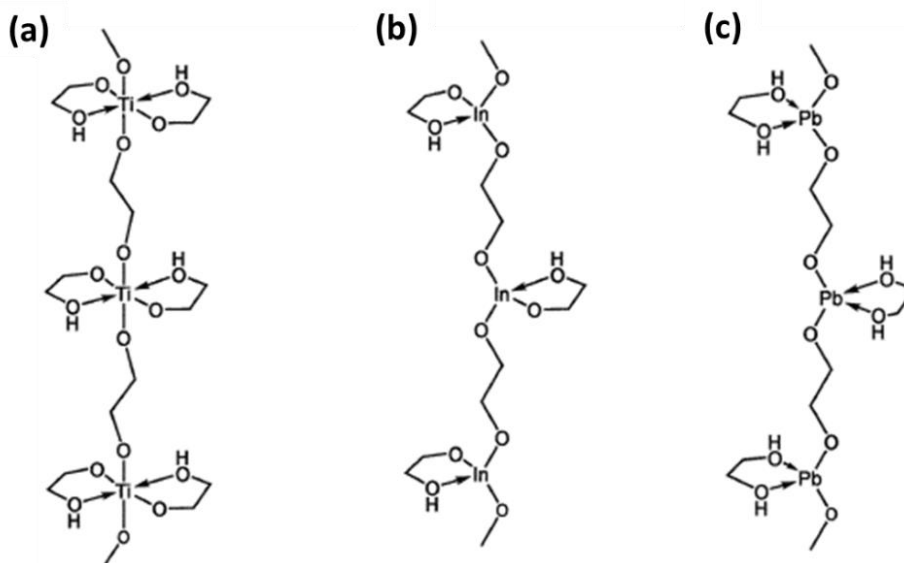


Figure 3-9 Schematic illustrations of linear complexes that were formed between ethylene glycol (a) Ti, (b) In, and (c) Pb cations [260]

3.2.3.2 2D plate/disc

In colloidal systems, the formation of 2D plate/disc shaped nanocrystals is uncommon, which is dissimilar with a 1D rod/wire. As schematically illustrated in Figure 3-10, in a kinetically driven growth regime, 1D nanorod growth is typically achieved by faster growth along a specific direction. On the other hand, when the growth direction is hindered and growth along the other two axis is coincidentally bechanced, 2D plate/disc shape particles can be developed. Ghezelbash et al., have synthesized 2D disc shaped Cu_2S through surface modification using alkanethiol surfactant [261]. The introduced alknethiol surfactant is preferentially adsorbed onto the plane along [001] direction and this results in inhibition to grow along the corresponding directions, and induces the growth along [100] and [110] direction. As a result, 2D disc shaped particles are accomplished (Figure 3-10(b)). Another similar modification tactic used for 2D particles synthesis can be found in the literature on NiS nanoprism [262]. As shown in Figure 3-10(b), in the presence of surfactant prohibiting growth along [110] direction, rapid growth along the other directions occurs.

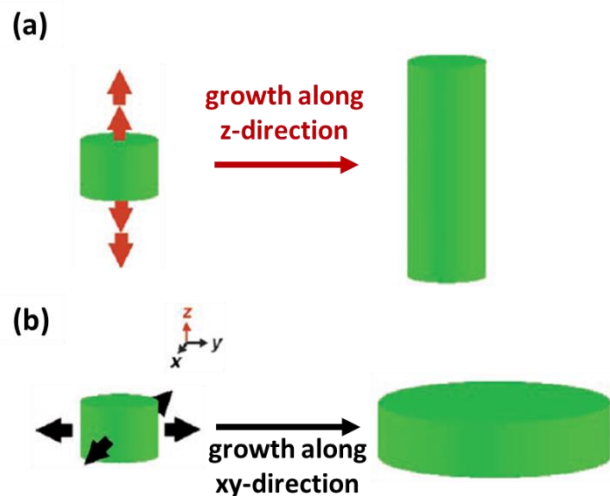


Figure 3-10 1D rod versus 2D disc growth; (a) preferential growth along one direction (z-axis), (b) growth along two directions (xy-plane)

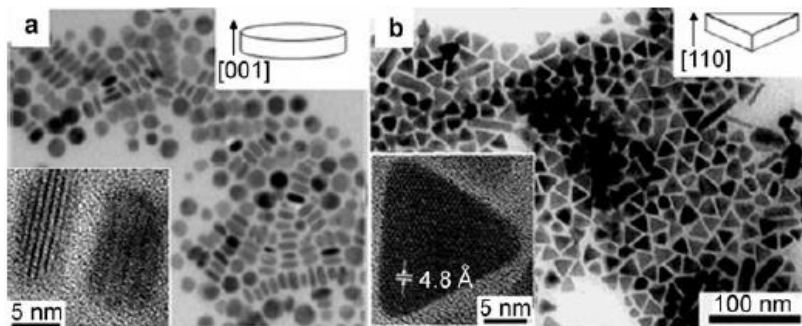


Figure 3-11 (a) Cu_2S discs [261] and (b) NiS nanoprism [262] through solvent less thermolysis of metal-alkanethiol complexes. Insets show HRTEM images of the Cu_2S discs and NiS prisms

Geng et al., have investigated growth behavior of BiOCl nanosheets through the self-assembly based on oriented attachment [254]. Figure 3-12 indicates the TEM images representing aggregation and crystallization process. The growth of BiOCl showed a similar self-assembly process from primary nano particles to lamellar structure in the reaction. The coarse

fringes of the nanosheets become smooth, implying the oriented attachment of nanoparticles at the fringe of the nanosheets and a further crystallization process.

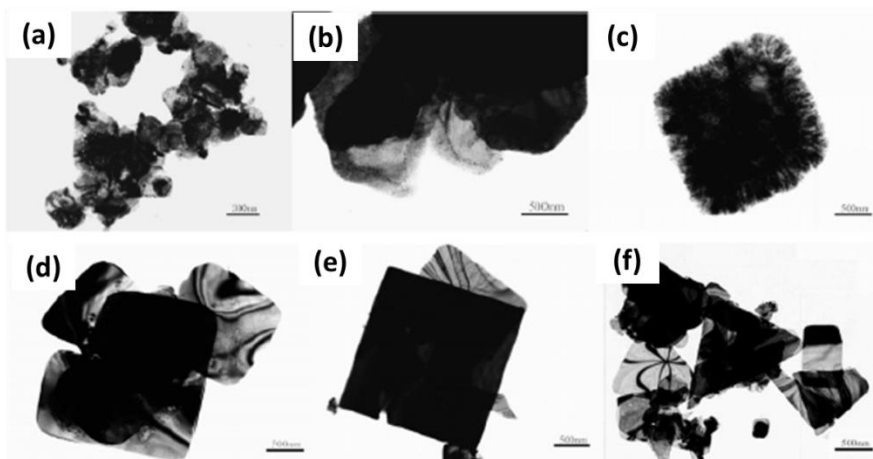


Figure 3-12 TEM images of BiOCl obtained after sonication for (a) 2, (b) 5, (c) 8, (d) 15, (e) 25, and (f) 60 min. The coarse fringes of lamellae became smooth, indicating an aggregation and crystallization process [254]

3.2.3.3 3D hierarchically architected particles

Concerning the driving force for the self-assembly of the 3D structured particles, although many hierarchical microstructures with oriented growth and assembly of nanosheets have been introduced, the detailed mechanism for the formation of complex inorganic microstructures still remains a mystery and has rarely been discussed [263]. Since multiple variables affect the self-assembly, entailing crystal-face attraction, electrostatic and dipolar fields associated with the aggregate, van der Waals forces, hydrophobic interactions, hydrogen bonds,

or the impact of their joint role [264], the formation mechanism for 3D hierarchical structure is quite intricate.

Wei et al., addressed the vapor-liquid-solid (VLS) formation mechanism on microwave-assisted synthesis of 3D SnO₂ nanoflower self-assembled from formed nanowires [265]. In this work, they found out that the supersaturation ratio plays a critical role in controlling the morphology of the final products in the VLS growth process. In the microwave heating process, there are excessive metal oxide and metal atom precipitating out in the reaction owing to the fast heating rate. Once Sn liquid drops form, it absorbs a Sn metal atom from the reaction media and rapidly grows in a short time. Due to the Sn metal atom precipitating out in the reaction environment rapidly, multiple critical nucleations will occur at the liquid-solid interface and continue to grow with adsorbed molecules, and this, in turn, leads to the formation of the flower like architecture.

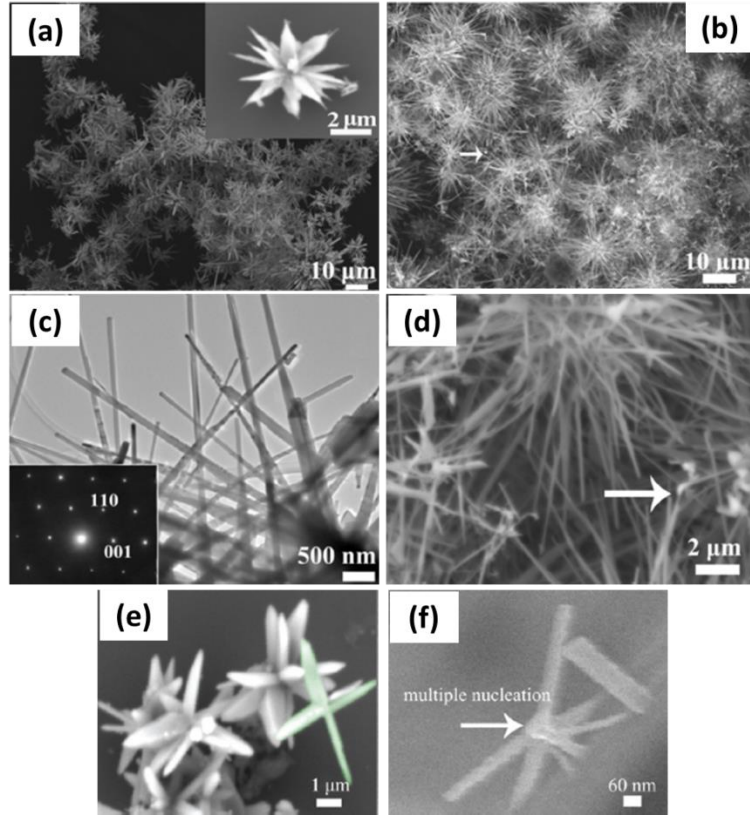


Figure 3-13 SEM images of SnO₂ nanoflowers: panels (a) and (b) are low-magnification SEM images of the nanoflowers, (c) TEM image of SnO₂ nanowires: the inset is the corresponding SAED pattern, (d) local high magnification SEM image of panel (b) [265]

The plausible mechanism on developing flower-like α -Fe₂O₃ from the reaction media with solvent mixture of DI water and ethanol has been suggested by Zeng et al. [266]. On the basis of the time-dependent experiments of the products, this work proposed a two-step growth model for the formation of a flower-like advanced nanostructure. As shown in Figure 3-15, in the first step, primary nanoparticles first appear in the solution. The primary nanoparticles gradually transformed to uniform nanoplates via Ostwald ripening process. Since there is a trace amount of water in the reaction system the particle growth process can possibly be limited. Subsequently, a secondary nucleation begins, and the flowers grow layer by layer, which is similar to the

progression referred in the terrace-step-kink model [267]. Based upon the notion that the layered structure can roll into nanotubes [268], multilayered structure rolled up and scrolled into flower-like nanostructures during the growth.

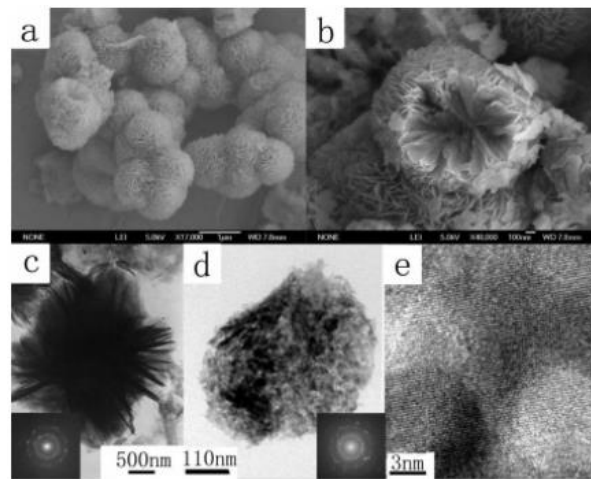


Figure 3-14 (a) SEM image of the flower-like α -Fe₂O₃, (b) high magnification SEM image of a single nanoflower, (c) TEM image of a single nanoflower (inset: SAD patterns), (d) TEM image of a single petal (inset: SAD pattern), (e) HRTEM image of a single petal [266]

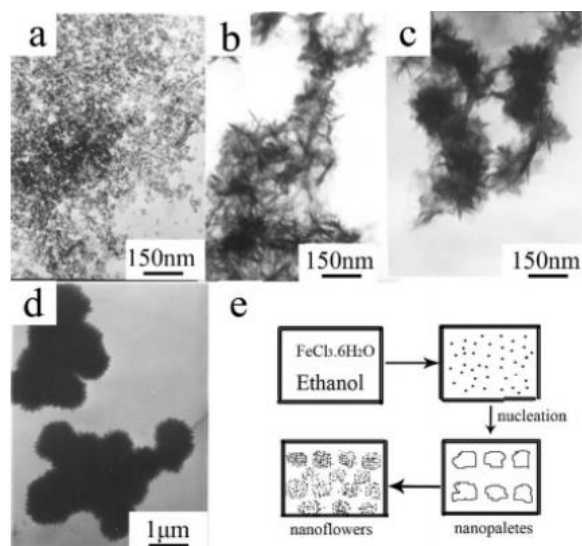


Figure 3-15 Time-dependent experiments for the precursor after reacting for (a) 1h, (b) 2h, (c) 3h, (d) 6h, and (e) schematic illustration for the nanoflower formation [266]

More complicated and detailed growth mechanism on the formation of hierarchical architecture has been intensively studied by Li et al. [269]. They investigated the self-assembly of flower like β -FeSe utilizing polyol based reaction media and addressed how polyol contributes in transformation of 2D nanoplates to 3D advanced structure. Basically, polyol possess the strong chelating ability with iron ions, which allows it to anchor to the surface and edges of the β -FeSe nanoplates and this leads to minimization of the total energy of the system and van der Waals interactions between the anchored polyol molecules, self-assembly of the nanoplates through edge-to-edge attachments and edge-to-surface conjunctions.

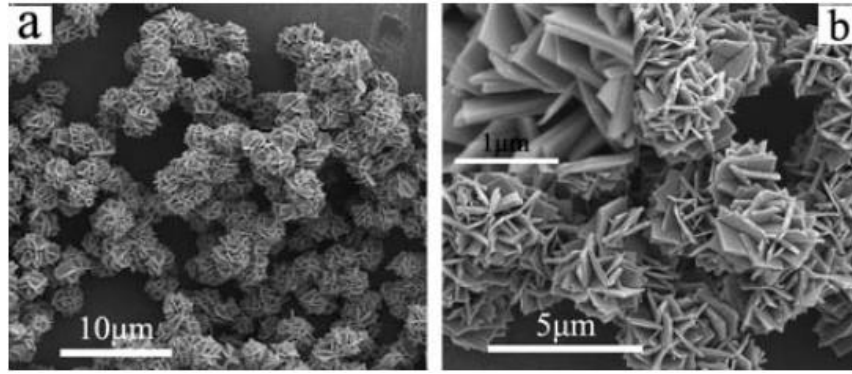


Figure 3-16 FESEM images of the as-prepared β -FeSe by microwave irradiation for 1 h. (a) Low magnification image, (b) high magnification image (inset: a much higher magnification image) [269]

3.3 3D SELF-ASSEMBLY OF FLOWER-LIKE PARTICLES

3.3.1 Sample preparation and characterization

3.3.1.1 Synthesis of flower-like shape particles

The fabrication of flower like shape (FLS) iron oxide particles was achieved by the ethylene glycol (EG) mediated self-assembly process of nanoparticles, which has been adapted to the synthesis of several nanomaterials [270-272]. 1.3 g of $\text{FeCl}_3 \cdot 6\text{H}_2\text{O}$, 7.2 g of tetrabutylammonium (TBAB), and 2.7 g of $\text{CO}(\text{NH}_2)_2$ (urea) were mixed homogeneously in 180 ml of EG at room temperature for 1 h. A mixture precursor with a red color was loaded into a Teflon vessel. The solution in a sealed Teflon vessel was reacted at 120–210 °C for 30 min under microwave irradiation (CEM-Marsxpress, USA). The pressure inside the vessel was controlled to be between 0.2 MPa and 1 MPa. The reaction temperature and pressure were independently controlled by changing the input of microwave power and the solution content in the vessel. The resulting particles were collected by centrifugation, washed with ethanol several times, and subsequently dried in a vacuum oven at room temperature for 18 h. As-grown particles with green color were crystallized at 400 °C in N_2 or forming gas ($\text{N}_2 + 5\% \text{H}_2$) for 2 h.

3.3.1.2 Characterization

The crystal structure of the thermally-annealed FLS-iron oxide particles was examined by the X-ray diffraction (XRD) method (Philips, PW-1810 diffractometer, Cu-K α radiation, $\lambda = 1.54$ Å). The Raman spectroscopy of particles was carried out at room temperature with an incident beam wavelength of 633 nm (Renishaw, inVia Raman microscope). The Fourier transform infrared (FTIR, Bruker VERTEX-70LS) spectra was recorded in a transmission geometry. Particles were mixed with KBr and the mixed particles were pressed into pellets. The morphology of FLS iron oxide particles was probed by field emission-scanning electron microscope (FE-SEM, Philips XL-30) and transmission electron microscope (TEM, JEOL 200CX). Magnetic properties were measured at room temperature by vibrating sample magnetometer (VSM, Lake Shore 7400). Nitrogen adsorption and desorption isotherm of the particles were also measured at liquid nitrogen temperature to analyze the surface structure. Before the adsorption measurement, the samples were outgassed under a vacuum for 3 h at 100 °C. In order to confirm the sulfidation ability of FLS particles, 0.1 g of the particles was introduced into 100 ml of 12.5 mM sodium sulfide (Na₂S) aqueous solution in a 200 ml glass. Then, the concentration of sulfur ions in water was monitored by measuring the ionic conductivity of S²⁻ (Denver instrument, 250 conductivity meter) at every 10 min.

3.3.2 Results and discussions

3.3.2.1 Crystal structure analyses

XRD patterns of the as-grown and annealed particles are presented in Figure 3-17. In the XRD pattern of the as-grown FLS precursor particles (Fig. 3-17a), broad peaks indicate a co-existence of α -Fe₂O₃ and α -FeOOH. Nucleation of α -FeOOH is known to compete with that of α -Fe₂O₃ below 80 °C [273]. Reflections of the as-grown particles at 26.4°, 33.0°, 44.8°, 53.7°, and 61.3° are indexed as (012), (104), (202), (116), and (214) of α -Fe₂O₃ (JCPDS 80-2377). Figure 3-17(b) and Figure 3-17(c) show XRD patterns of the samples that were annealed at N₂ and N₂+5%H₂ atmosphere. To make the particles magnetically active, particles were annealed only in a reducing atmosphere. After being annealed at 400 °C in a N₂ atmosphere, the XRD pattern of the FLS particles matches well with the diffraction pattern of Fe₃O₄ (magnetite, JCPDS 85-1436). In comparison, annealing in N₂+5%H₂ resulted in the appearance of a Fe phase (JCPDS 87-0721). There are several polymorphs of iron oxide and oxyhydroxide (e.g., α -Fe₂O₃, α -FeOOH, γ -FeOOH) and each phase exhibits a distinctive Raman spectrum. The Raman investigation, therefore, is regarded as one of the reliable methods to discern phases of the particles which do not have a long range order [274]. In addition, Raman spectroscopy is complementary to XRD analysis, which does not clearly differentiate Fe₃O₄ from γ -Fe₂O₃ [275]. To accurately identify the crystal phase of each product, Raman spectroscopy is used and the Raman spectra of the as-grown and N₂-annealed particles are displayed in Figure 3-18. For the as-grown precursor particles (Fig. 3-18a), Raman peaks represent the coexistence of α -FeOOH (227, 262, 324, and 432 cm⁻¹) and α -Fe₂O₃ phases (388, 494, 616, 652, 826, 914, 1064, and 1103 cm⁻¹), which are in agreement with reported studies [276-278]. The Raman spectra of N₂-

annealed FLS particles are presented in Figure 3-18(b). A relatively strong band centered at 661 cm^{-1} and two broad peaks at 306, and 530 cm^{-1} is shown in the results, confirming the formation of the Fe_3O_4 phase for FLS- Fe_3O_4 particles [279,280]. This indicates that the as-grown particles consisting of $\alpha\text{-Fe}_2\text{O}_3$ and $\alpha\text{-FeOOH}$ phases are fully transformed to Fe_3O_4 in N_2 -annealing.

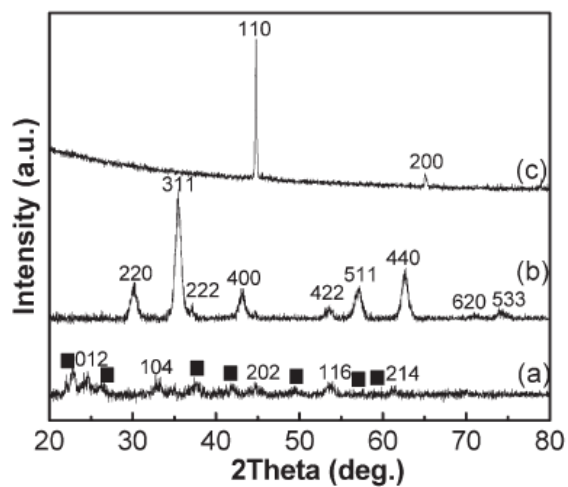


Figure 3-17 XRD patterns of fabricated FLS particles; (a) as-grown FLS-precursor, (b) FLS- Fe_3O_4 , and (c) FLS-Fe particles. (■ : $\alpha\text{-FeOOH}$)

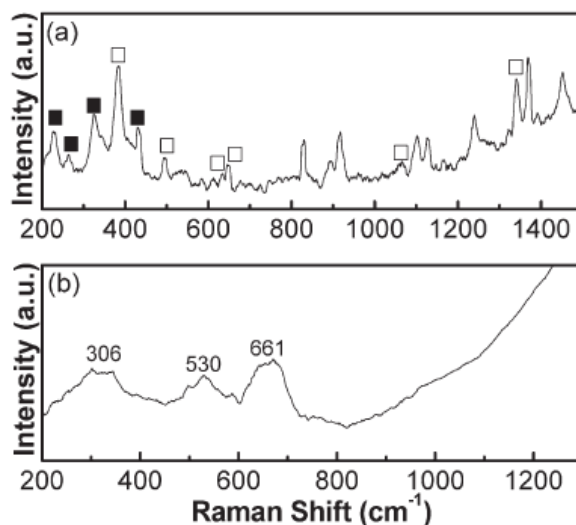


Figure 3-18 Raman spectra of (a) as-grown FLS particles and (b) N₂-annealed FLS particles (■ : α -FeOOH, □ : α -Fe₂O₃)

When FeCl₃ meets with EG, a series of reactions occur and nanoparticles are formed in the precursor solution. First, FeCl₃ first meets with EG (HOC₂H₄OH) and a partial reduction occurs to generate iron alkoxide [281]. Then, Fe₂O₃ primary nanoparticles are formed by a reaction between iron alkoxide and oxygen [199]. In addition to the precipitation of Fe₂O₃ nanoparticles, Fe³⁺ from FeCl₃ can directly react with OH⁻ and produce FeOOH. To validate the reaction mechanism of primary nanoparticles, the FTIR spectra of the as-grown and thermally-annealed FLS particles were investigated. The FTIR spectrum of the as-grown FLS particles is shown in Figure 3-19. The strong absorption band lying in the 2500–3000 cm⁻¹ range is characteristic of the C–H stretching mode and all the peaks located below 1750 cm⁻¹ are Fe–O, C–O, C–C, and CH₂ bonds that are the main moieties of Fe-alkoxide [282]. With Raman spectra and XRD patterns, the FTIR spectra clearly supports the notion that the Fe-alkoxide is formed from the EG-mediated reaction of FeCl₃ and a significant amount of Fe-alkoxide is still left in the as-grown particles.

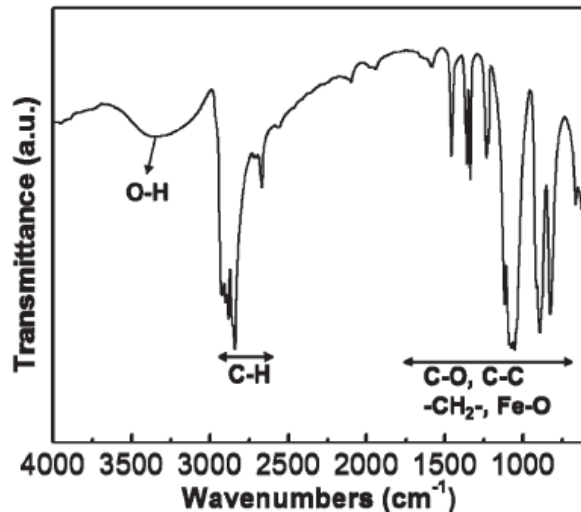


Figure 3-19 FTIR spectra of the as-grown FLS particles

3.3.2.2 Morphology of the superstructured particles

Changes in the morphological characteristics were examined by SEM and TEM. Figure 3-20 shows SEM and TEM micrographs of the as-grown FLS particles. When raw materials were reacted at 180 °C and below 0.2 MPa, the product of the reaction was FLS particles with a size of 2 ~ 3 μm. The surface of the petal-like plates was very smooth and their thickness was smaller than 100 nm (Fig. 3-20a and 3-20b). A detailed microstructure of FLS particles is shown in the inset of Figure 3-20(c). The selected area diffraction (SAD) patterns of as-grown FLS-particles exhibit diffraction rings confirming polycrystalline nature of the as-grown FLS particles. This is consistent with XRD patterns. Grain boundaries of nanoparticles are not observed even in a TEM micrograph with higher magnification (Fig. 3-20d). Figure 3-21 shows

SEM and TEM micrographs of the particles after thermal annealing. The morphology of Fe_3O_4 nanoparticles crystallized by N_2 annealing is similar to that of as-grown FLS particles (Fig. 3-21a). This suggests that FLS particles maintain their unique shape during N_2 treatment at 400°C . TEM images of Fe_3O_4 (Fig. 3-21b and 3-21c) indicate that each petal-like plate of FLS particles is polycrystalline and porous. Appearance of pores in the petals of FLS particles is ascribed to the decomposition of iron alkoxide and $\alpha\text{-FeOOH}$ and the removal of residual organic species during annealing. The SAD patterns (the inset of Fig. 3-21b) clearly reveal polycrystalline nature. High magnification TEM micrograph in Fig. 3-21(c) shows that the individual petal consists of small nanoparticles with a size of $10 \sim 15$ nm. This value is inconsistent with the particle size that is determined by analyzing XRD patterns via the Debye-Scherrer equation. In comparison, Fe particles crystallized by $\text{N}_2+5\%\text{H}_2$ annealing display a moderate change in the shape during the annealing process (Fig. 3-21d). Though the hierarchical superstructure was found and the pores were created, FLS particles partially collapsed and the petals warped more after $\text{N}_2+5\%\text{H}_2$ annealing than N_2 annealing.

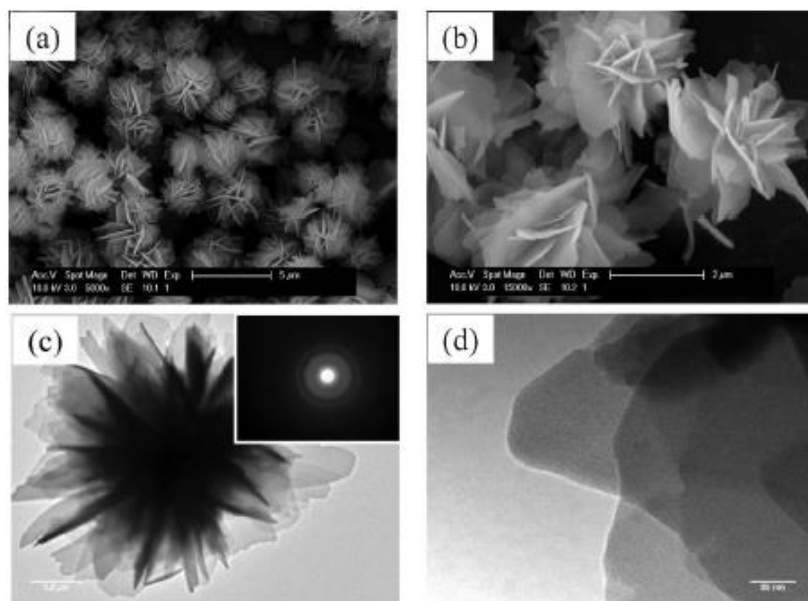


Figure 3-20 SEM and TEM micrographs of as-grown FLS-precursor particles. (Inset: selected area diffraction (SAD) patterns)

3.3.2.3 Effects of reaction parameters on primary particles and self-assembly

The morphology of the superstructured particles is sensitive to experimental parameters such as reaction temperature, reaction time, reagent concentration, solvent types, and solution pH [283-285]. In the present work, we systematically investigated the evolution of the hierarchical structures during the microwave-assisted reaction. There is an optimum range of reaction temperature and reaction pressure, which is suitable for the formation of hierarchically structured FLS-particles. Among the experimental variables, the reaction temperature is critical in the self-assembly of the nanoparticles. As shown in Figure 3-22(a), the reaction at 120 °C leads to irregular aggregates of nanoparticles. When the reaction temperature was increased to 150 °C

(Fig. 3-22b), the nanoparticles assemble to form 3-dimensional (3-D) frameworks of nanoplates. However, the binding strength between the nanoplates is not strong enough to make the surface of the nanoplates smooth. The surface is rough and the individual nanoparticles are still identified.

At the reaction temperature of 180 °C (Fig. 3-22c), 3-D hierarchical architecture with a smooth surface is achieved. However, further increase of the reaction temperature to 210 °C (Fig. 3-22d) results in random aggregates of nanoparticles with diameters of 90–100 nm, in which case self-assembly of the nanoparticles is not observed. This implies that the self-assembly process of the nanoparticles competes with the growth process of the nanoparticles, and that there is an optimum window of reaction temperature for the formation of 3-D FLS particles. The other parameter examined in this study is the reaction pressure. Since the precursors were reacted in a sealed Teflon vessel, the increase in the reaction temperature was accompanied by the increase in the reaction pressure. To separate the effect of the reaction temperature from that of the reaction pressure, the reaction temperature was fixed at 180 °C and only the reaction pressure was controlled by varying the volume of the precursor solution inside a sealed Teflon reactor. SEM micrographs in Figure 3-23 show the change in the morphology of the reaction products as a function of the pressure. When the pressure in the reactor was below 0.2 MPa (Fig. 3.7a), well-structured hierarchical FLS particles were obtained. While, when the pressure was between 0.3 and 1 MPa (Fig. 3-23b), the petal-like plates consisting of the nanoparticles were observed. A part of the particles have the microstructure of stacked plates and a part of them show the 3-D FLS structure. When the pressure was higher than 1 MPa (Fig. 3-23c), the particles turned to large flakes. The change from the FLS structure to the flake structure is explained by the role of urea. In the EG-mediated reaction of FeCl_3 , HCl is produced as a byproduct [286]. However, an

increase in HCl concentration decreases pH and prohibits further conversion of FeCl₃ to the iron alkoxide. This, in turn, decreases the yield of the EG-mediated reaction. To prevent the side effect of HCl, urea is added to the precursor solution as a neutralizing agent that is decomposed to provide counter ions, OH⁻. In the previous study, Chen et al. suggested that the decomposition of urea is sensitive to the pressure of a reaction solution [287],



As described in eqn (3.8) and (3.9), the decomposition of urea releases CO₂ gas as well as OH⁻ ions. Therefore, the increase in the reaction pressure restricts the decomposition of urea by preventing the release of CO₂ from the solution. The degree of urea decomposition begins to diminish beyond a pressure of 0.5 MPa. When the reaction pressure reaches 0.9 MPa, only a small portion of urea is decomposed. This indicates that the conversion of FeCl₃ to iron alkoxide is negligible at high pressure and the amount of primary nanoparticles from iron alkoxide is not large enough to develop the 3-D hierarchical superstructure. As a result, only 2-D flake type particles are produced in the high pressure environment.

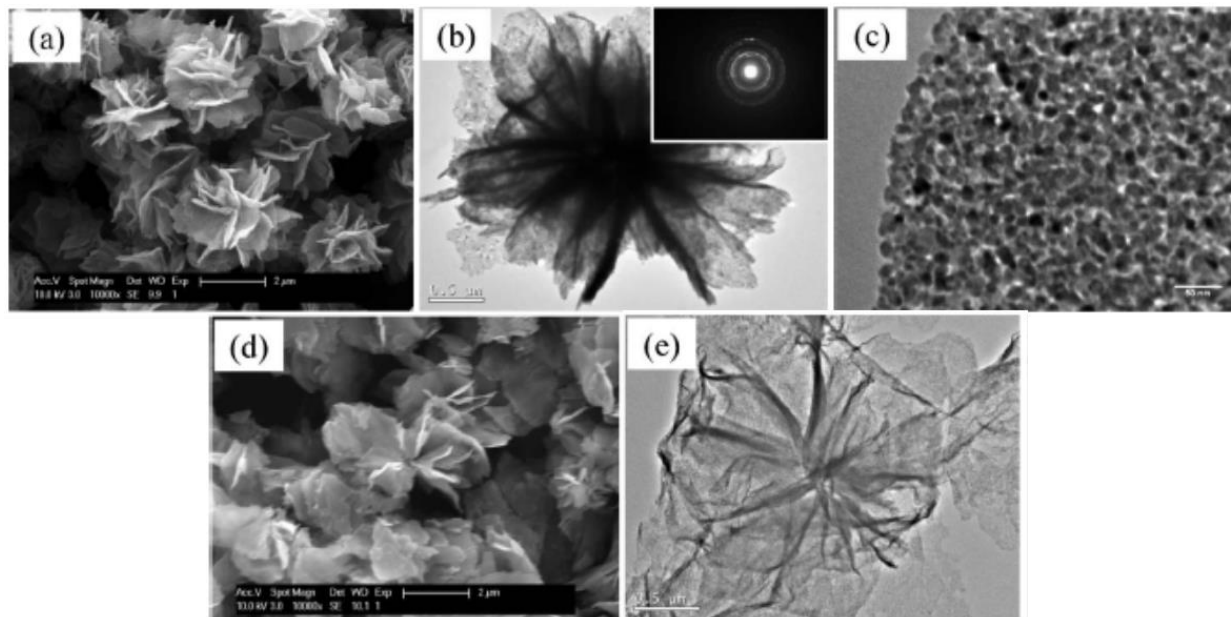


**Figure 3-21 SEM and TEM micrographs of (a), (b), (c) FLS-Fe₃O₄ and (d), (e) FLS-Fe particles.
(Inset: selected area diffraction (SAD) patterns of FLS-Fe₃O₄ particles)**

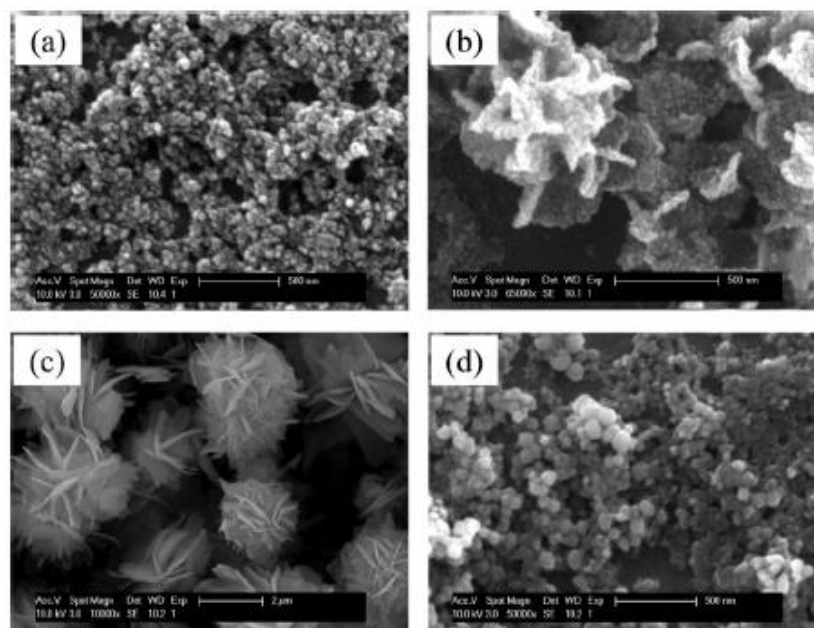


**Figure 3-22 SEM micrographs of the as-grown particles obtained at different reaction temperatures:
(a) 120 °C, (b) 150 °C, (c) 180 °C, and (d) 210 °C**

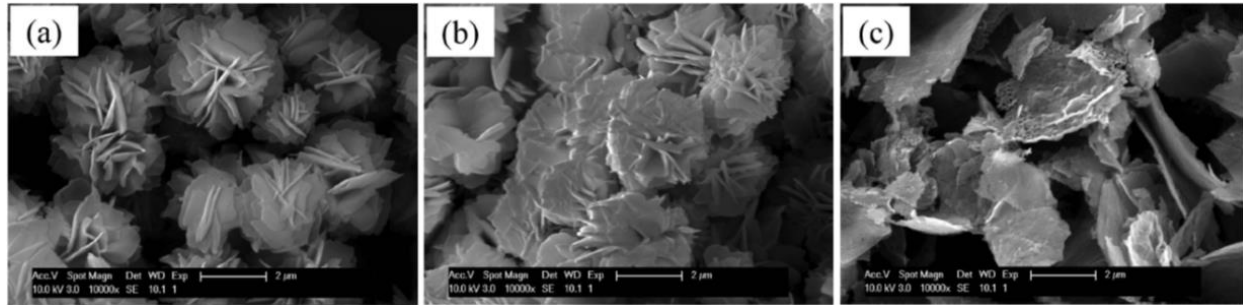


Figure 3-23 Change in the morphology of the reaction products as a function of the pressure: (a) ~0.2 MPa, (b) 0.3 ~ 1 MPa, and (c) 1MPa

3.3.2.4 Mechanism of the self-assembly of 3-D FLS particles

To understand the self-assembly process of 3-D FLS particles, the reaction process was monitored as a function of reaction time. As seen in Figure 3-24(a), the product at the early stage of the reaction, at 180 °C, and below 0.2 MPa, was nanoparticles with a diameter of about 50 nm. A large amount of the nanoparticles was formed within 20 s in the precursor solution. After the microwave-assisted reaction continued for 1 min (Fig. 3-24b), a small portion of the nanoparticle gathered to form microspheres with a diameter of 1-2 μm. The microspheres coexist with the nanoparticles. As the reaction proceeded (Fig. 3-24c), most of the nanoparticles is consumed to form the microspheres. Simultaneously, 3-D hierarchical structures started to appear. When the reaction time continued for 5 min, all nanoparticles turn to fully developed FLS particles, as shown in Figure 3-24(d). From this point, the morphology and size of FLS particles were maintained. It is worth noting that the growth of fully developed FLS particles under the

microwave irradiation was completed within 5 min, which is much faster than conventional methods. This means that the ‘hot-spots’ effects induced by the microwave irradiation may create an environment suitable for the fast nucleation of nanoparticles and their accelerated growth to FLS-precursor particles [288]. On the basis of experimental observations in the above, a three-step growth mechanism is proposed. This is composed of i) a fast nucleation of amorphous primary nanoparticles, ii) an aggregation of nanoparticles into the microspheres with rough surface, and iii) the self-assembly of thin plates onto the microspheres [289-291]. Oriented assembly of the nanoparticles has been considered as being a key step in producing the hierarchical superstructure [292]. Various factors influence the oriented assembly of the nanoparticles, such as surface energy, electrostatic and dipolar fields, van der Waals forces, hydrophobic interactions, and hydrogen bonds. Given that the surfactants are not added to the precursor solution in this study, the surface energy is speculated to play a major role in the formation of FLS particles. Penn et al. and Li et al. propose that a main driving force to develop such hierarchical particles is a tendency to reduce the high surface energy via self-assembly of adjacent particles [293,294]. In addition, the chelating ability of EG may contribute to the formation of FLS particles. Li et al. suggests that the generation of self-assembly of nanosheets is caused by the anchored polyol molecules. The strong chelating ability of the EG with iron ions makes it anchor to the surface and edges of nanosheets [295]. This gives rise to edge-to-edge attachment and edge-to-surface conjunction among the nanoparticles, leading to the formation of hierarchical FLS superstructure.

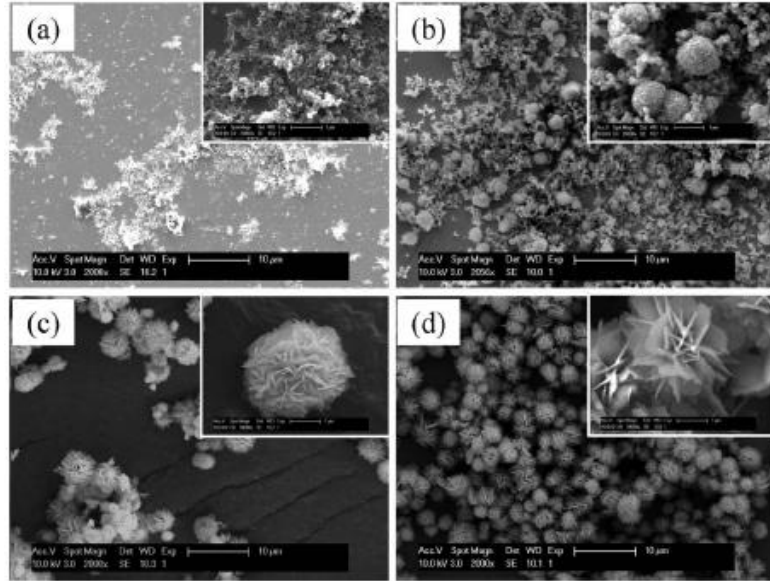


Figure 3-24 SEM micrographs of as-grown particles as a function of reaction time; (a) 20 s, (b) 60 s, (c) 2 min, and (d) 5 min (a scale bar in the inset is 1µm)

3.3.2.5 Surface characteristics

Figure 3-25 shows the nitrogen adsorption–desorption isotherms and corresponding pore size distribution of as-grown particles, Fe_3O_4 and Fe particles, respectively. The Brunauer–Emmett–Teller (BET) surface area of as-grown FLS particles (Fig. 3-25a) was $15.7 \text{ m}^2 \text{ g}^{-1}$, while the FLS– Fe_3O_4 (Fig. 3-25b) and FLS–Fe (Fig. 3-25c) particles had specific surface areas of $71.1 \text{ m}^2 \text{ g}^{-1}$ and $41.9 \text{ m}^2 \text{ g}^{-1}$, respectively. The increased surface area of thermally-annealed FLS particles is attributed to the formation of internal pores. The adsorption and desorption isotherms of the as-grown particles in Figure 3-25(a) are close to type II isotherms that do not show the hysteresis loop. Given that the type II isotherm is typical for non-porous or macroporous

materials, the isotherms in Figure 3-25(a) indicate that the as-grown FLS particles do not have mesopores [296]. In contrast, the isotherms of thermally annealed FLS particles (Fe_3O_4 and Fe) exhibit the hysteresis loops that results from different adsorption and desorption in the mesopores. The isotherm of FLS- Fe_3O_4 displays the features of H3 type hysteresis loops. This indicates that both slit-like mesopores and micropores are formed during the annealing. The coexistence of mesopores and micropores is confirmed in the pore size distribution curve, shown in the inset of Figure 3-25(b). Though the hysteresis loop is also observed, the isotherm curve of FLS-Fe particles is close to H4 type hysteresis loop in that the adsorption and desorption branches remain nearly horizontal over a wide range of p/p_0 . This H4 type hysteresis loop shows that the phase transition to metallic Fe during the annealing in reducing environment develops the slit-like mesopores with a well-defined size and shape. The results of the BET analysis are consistent with TEM micrographs of Figure 3-21, showing that the decomposition of iron alkoxide and $\alpha\text{-FeOOH}$ and the removal of organic species during the thermal annealing create mesopores in the FLS- Fe_3O_4 and FLS-Fe particles. The large surface area of thermally-annealed FLS particles suggests that these hierarchical structured particles would be utilized as efficient catalysts and absorbents.

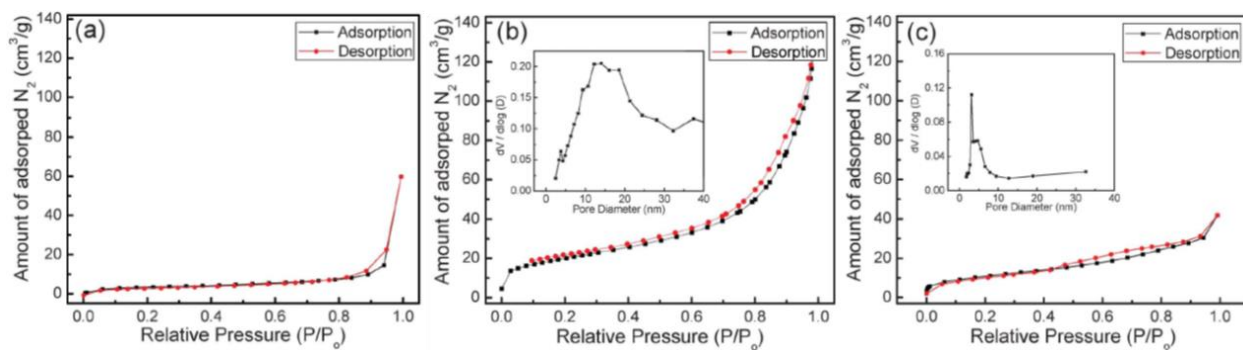


Figure 3-25 Nitrogen adsorption-desorption isotherms and pore size distribution curves of (a) as-grown FLS-precursor, (b) FLS-Fe₃O₄, and (c) FLS-Fe particles. (Inset: pore size distribution curve)

3.3.2.6 Application to water treatment

Hydrogen sulfide (H₂S) has been reported as a malodorous toxic gas which could spread out through water [297]. To remove H₂S from water, several sorbents containing metal elements such as Fe, Zn, Ti, V, and Al, have been intensively explored [214,298-300]. In this study, we tested the capability of FLS particles to remove H₂S from water. To simulate H₂S dissolved in water, Na₂S was added to water. When sodium sulfide (Na₂S) is exposed to a moist environment, Na₂S and its hydrates emit hydrogen sulfide. In the solution, as summarized in eqn (3.10), the dianion S²⁻ does not exist in perceivable amounts in water since S²⁻ is an excessively strong base which may not be favorable for coexistence with water. Dissolution of Na₂S in the water is expressed as follow:



After FLS particles were added to the solution, the relative concentration of HS^- in water was examined by measuring the electrical conductivity of the solution. Figure 3-26 shows the concentration of sulfur ion as a function of reaction time. Both FLS- Fe_3O_4 and Fe removed most of the sulfur ions from the solution within 10 min. When the aqueous solution of 3000 ppm Na_2S was reacted for 50 min, less than 2% of the sulfur ions were left in solution. It is known that the reaction between Fe and S gives FeS_2 or Fe_3S_4 , depending on their thermodynamic stability in the reaction conditions. Fast removal of H_2S , shown in Figure 3-26, indicates that the large surface areas of the FLS-Fe and FLS- Fe_3O_4 particles provide plenty of active sites for the sulfidation reaction. Almost similar HS^- removal rates by FLS-Fe and FLS- Fe_3O_4 particles imply that the activation energy for the reaction with HS^- may be lower for Fe than for Fe_3O_4 and that the different reaction kinetics may compensate for the difference in surface area.

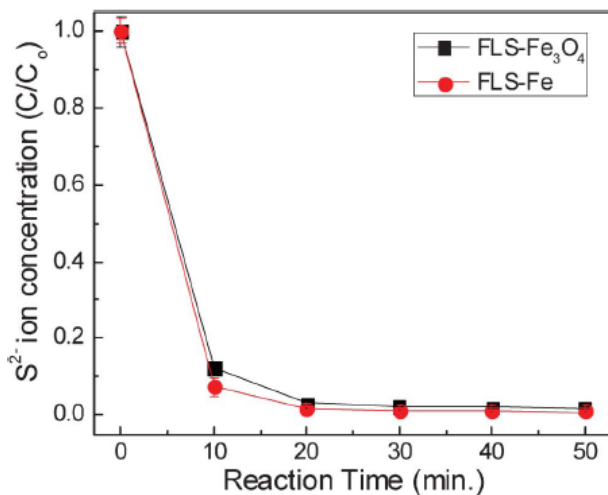


Figure 3-26 Concentration of residual sulfur ions as a function of reaction time

3.4 MAGNETORHEOLOGY OF MR FLUID WITH FLS IRON OXIDE

3.4.1 Results and discussions

3.4.1.1 Magnetic property of FLS Fe₃O₄ particle

Magnetization is one of the important parameters to evaluate the structure and property of Fe-based materials. To investigate the magnetic properties of the FLS-Fe₃O₄ particles, the magnetic properties of the particles were measured at room temperature using VSM. M-H curves are shown in Figure 3-27. The saturation magnetization (M_s) of the FLS-Fe₃O₄ particles was 45.0 emu g⁻¹. The inset of Fig.3-27 shows that the coercivity (H_c) for the Fe₃O₄ was 23.6 Oe. The M_s value for FLS-Fe₃O₄ was lower than the value of bulk Fe₃O₄ (92 emu g⁻¹).

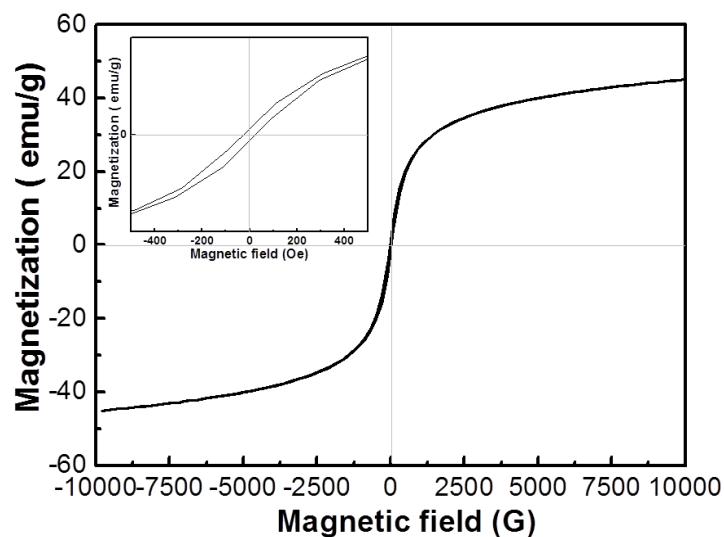


Figure 3-27 M-H curves of FLS-Fe₃O₄ particles (inset: hysteresis loop of FLS-Fe₃O₄)

3.4.1.2 Viscoelastic properties of the fluids containing FLS-Fe₃O₄ particles

To understand an influence of hierarchical morphology of FLS-Fe₃O₄ particles on the rheology of the fluids containing magnetic particles, we carried out a magnetorheological analysis in a strain amplitude sweep mode using rheometer (MCR-301, Anton Paar) with magnetorheological devices. Figure 3-28 shows the plot of the storage modulus versus the strain amplitude in the fluids containing a different amount of FLS-Fe₃O₄ particles. The storage modulus increases dramatically as the content of FLS-Fe₃O₄ particles increased from 5 to 40 wt %.

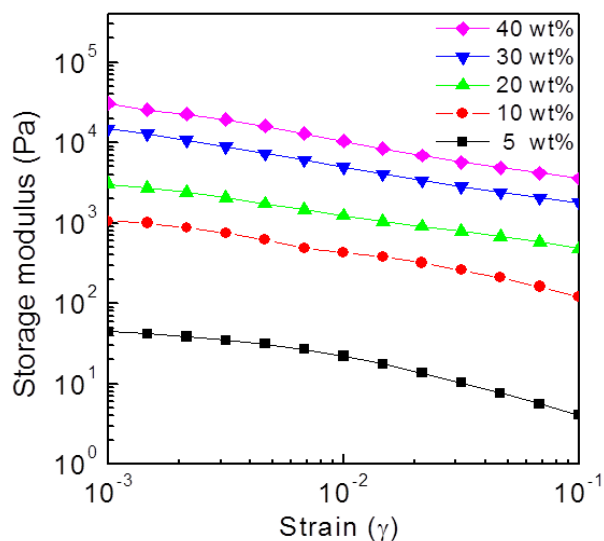


Figure 3-28 (a) M-H curves of FLS-Fe₃O₄ particles, and (b) storage modulus vs. strain amplitude curves of the fluids containing different amount of FLS-Fe₃O₄ particles when the magnetic field of 0.38 T is applied

3.4.1.3 Viscoelastic properties of the fluids containing FLS-Fe₃O₄ particles under applied magnetic field

Figure 3-29(a) shows an increment of the storage modulus in a 10 wt % fluid as a function of magnetic field. When a magnetic field of 0.38 T was applied, the storage modulus of the fluid containing the FLS-Fe₃O₄ particles increased by more than two orders of the magnitude, compared to zero magnetic field. As a control sample, we also prepared a fluid containing spherical γ -Fe₂O₃ particles with an average diameter of 30 nm. Their saturated magnetization

was about 80 emu/g, which is very similar to that of FLS-Fe₃O₄ particles. The stability of the fluid containing 10 wt % γ -Fe₂O₃ nanoparticles is similar to that of the FLS-Fe₃O₄ particle fluid due to the nanosize of γ -Fe₂O₃ particles. Same analysis was performed using the fluids of spherical γ -Fe₂O₃ particles to examine the effect of the surface morphology. Though the saturated magnetizations of γ -Fe₂O₃ and FLS-Fe₃O₄ particles are almost same, their storage moduli are very different. When 10 wt % of the spherical particles were added, there is a moderate increase in the storage modulus under the magnetic field, which is demonstrated in previous studies [301,302]. At the same solid content and magnetic field, as shown in Figure 3-29(b), the storage modulus of FLS-Fe₃O₄ fluids is two times as large as that of the spherical particles. A comparison of two fluids indicates that a unique morphology of FLS-Fe₃O₄ particles increases interparticle interaction at the surface, leading to larger friction between the particles and an enhanced dependency on the magnetic field.

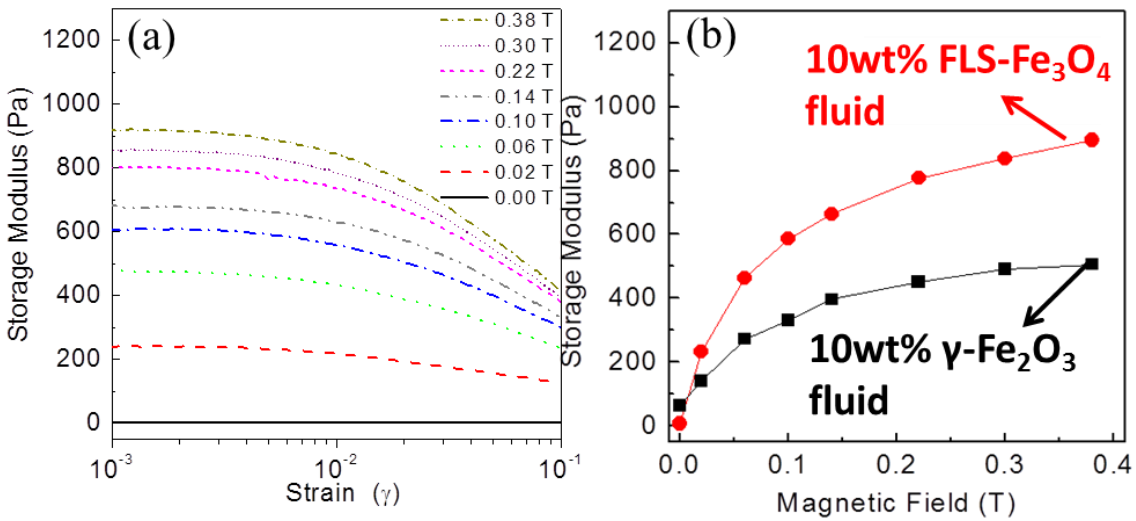


Figure 3-29 (a) Storage modulus vs. strain amplitude curves of the fluids containing 10 wt% FLS- Fe_3O_4 particles under magnetic field (0-0.38 T), (b) a change in the storage modulus of the fluids containing 10 wt% FLS- Fe_3O_4 or spherical $\gamma\text{-Fe}_2\text{O}_3$ particles

3.4.1.4 Interparticle interaction and particle association of fluid containing FLS- Fe_3O_4 particles under applied magnetic field

The strength of the interparticle interaction and the particle networks in the fluids can be evaluated by monitoring the transition of the fluids from a solid-like status to a liquid-like status. Therefore, we forced two different fluids (10 wt% FLS- Fe_3O_4 particle fluid and 10 wt % spherical $\gamma\text{-Fe}_2\text{O}_3$ particle fluid) to be subject to incremental oscillatory motion and compared their loss moduli to their storage moduli as functions of oscillatory strain. Figure 3-30(a) shows the change in the storage (G') and loss modulus (G'') obtained from the oscillatory measurement

at a constant magnetic field of 0.38 T. As the amplitude of the oscillatory strain increases, the network of the magnetic particles is shaken and the strength of interparticle connection is weakened. When the oscillatory strain reaches a critical strain, the breakdown of the particle network begins and G' starts to fall significantly. At the same critical strain, G'' exhibits a maximum value due to the out-of-phase motion of the particle network in the fluids. These changes in G' and G'' at a critical point represent yield of fluids over applied strain. As the oscillatory strain becomes larger than critical strain (γ_y), the fluids show a transition from solid-like state to liquid-like state [303,304]. The strength of the magnetic particle network is estimated by comparing the critical strain (γ_y) and effective yield stress (τ_y) of colloidal fluids. G' corresponding to the critical strain is G_y' . By using τ_y and G_y' , we estimate the effective yield stress which induces a viscous flow that is indicative of a liquid-like state,

$$\tau_y = \gamma_y G_y'$$

$$\tau_i = \gamma_i G' (\gamma \rightarrow 0)$$

In addition, G' in the low strain region, $G'(\gamma \rightarrow 0)$ and initial strain (γ_i) show the stress (τ_i) that is required for the initial breakdown of the colloidal network. The initial strain is defined as a strain of a point where the linear viscoelastic region ends. Then, τ_i represents the strength of the particle network in the solid-like state. Table 3-1 shows values of rheological parameters to estimate the strength of colloidal network at 0.38 T. The value τ_y , stress of self-assembled particle is about five times stronger than that of spherical Fe_2O_3 particles, attesting that rugged surface of the self-assembled particles increases interparticle friction when they are aligned and neighbored by the external magnetic field. This is schematically explained in Figure 3-30(b). The

values of τ_i , show that the self-assembled particles and the spherical particles begin to break the network structure over 4.53 and 2.84 Pa. These results are consistent with the previous explanation that FLS-Fe₃O₄ particles are more rigid to strain amplitude. Therefore, it is more difficult to make a transition to the liquid like state which exhibits viscous flow under oscillatory motion, leading to a larger effective yield stress of the FLS-Fe₃O₄ particle fluid.

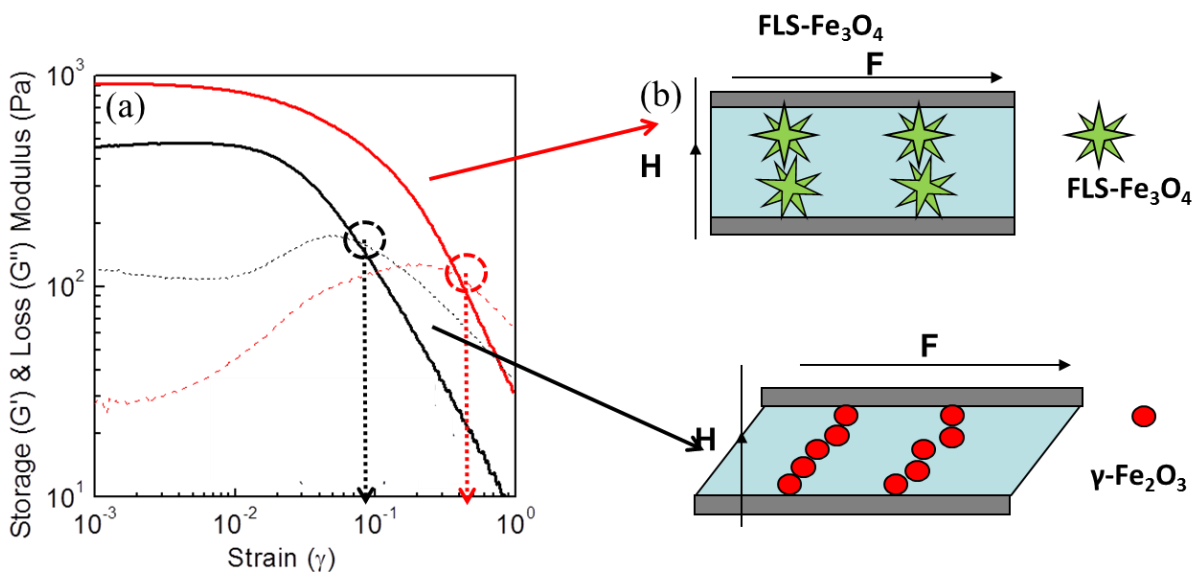


Figure 3-30 (a) Storage (G') and Loss (G'') modulus for FLS-Fe₃O₄ ferrofluid and spherical γ -Fe₂O₃ at 0.38 T, (b) Scheme for increasing stress to break the rows of aligned particles by the rugged surface of FLS-Fe₃O₄

Table 3-3 Rheological parameters of FLS-Fe₃O₄ and spherical γ -Fe₂O₃ particle fluids at a constant magnetic field of 0.38 T

Fluid	G'_y/Pa	γ_y	τ_y/Pa	$G'_{(y \rightarrow 0)}/\text{Pa}$	γ_i	τ_i/Pa
10 wt% FLS-Fe ₃ O ₄	254	0.21	53.34	906	0.005	4.53
10 wt% γ -Fe ₂ O ₃	186	0.052	9.67	473	0.006	2.84

4.0 CONCLUSIONS AND FUTURE WORK

4.1 CONCLUSIONS

Research topics discussed in this dissertation have covered the rational design and synthesis of the clay hybrids including nanoparticles embedded clay hybrid particles and nanoparticles decorated organoclay hybrid and 3D self-assembled flower-like shaped (FLS) particles through microwave-assisted reaction, and their applications in the control of rheological behavior of the clay based fluid system and catalytic performance in the waste-water treatment, respectively. In addition, these particles are employed in the magneto rheology control to instigate the change in network formation of the particles under an applied magnetic field. Detailed conclusions are summarized as following.

As tackled in the Chapter 2, in the first part, two different types of the nanoparticle – clay hybrid particles were synthesized and their effect on the rheological properties of aqueous bentonite fluids was investigated. In 5B-0.5ICH fluid, individual particles cross-link to develop a relatively well-oriented porous structure. The formation of the rigid gel structure makes a noticeable increase in the viscosity, yield stress, storage modulus, and flow stress of the fluids. The strengthening of the gel structure by the addition of ICH particles results from the development of net positively charged edge surfaces in ICH. The role of ASCH particles on the clay platelets association in the bentonite fluids is sensitive to the change in pH. At high pH, the

addition of ASCH into the bentonite suspension gives rise to the collapse of the pre-existing clay network and prevents the E-F type association of the platelets, leading to the decrease in the viscosity, yield stress, storage modulus, and flow stress. As pH of the fluid containing ASCH additives decreases, the clay in the suspension become flocculated and the rheological properties of the ASCH added fluid get close to those of the ICH added fluids. A correlation between the net surface charge of the hybrid additives and the rheological properties of the fluids indicates that the embedded nanoparticles within the interlayer space control the variable charge of the edge surfaces of the platelets and determine the association modes of the clay constituents in the fluids.

In the second part of Chapter 2, a stable fluid containing a composite of OA-treated iron oxide and CTAB-treated clay was investigated. When plate-type montmorillonite and magnetite nanoparticles were treated with alkyl amine and oleic acid, the hydrophobic attraction led to the attachment of magnetite nanoparticles to the surface of montmorillonite. The magnetite nanoparticle decorated clay was well dispersed in organic media and the rheological properties of the fluid were controlled by applying a magnetic field.

In Chapter 3 describing microwave-assisted synthesis of FLS particles and their application for waste-water treatment, the formation mechanism of the Fe_3O_4 and Fe particles with 3D advanced architecture and the role of critical reaction parameters including temperature and pressure in the development of such a hierarchical superstructure were discussed. Hierarchical precursor particles have been successfully prepared by a microwave-assisted reaction of $\text{FeCl}_3 \cdot 6\text{H}_2\text{O}$, TBAB, urea, and EG at 180°C for 30 min. FLS particles with a hierarchical structure are formed through the self-assembly of iron alkoxide, $\alpha\text{-Fe}_2\text{O}_3$ and FeOOH nanoparticles. The appearance of FLS particles is sensitive to reaction temperature and

reaction pressure. Due to the competition between the self-assembly process and growth process of the nanoparticles, there is an optimum window of the reaction temperature for the formation of 3-D FLS particles. Also, the combined use of FeCl_3 , EG, and urea as raw materials makes the reaction of FLS particles strongly dependent on the pressure. Since urea is not decomposed well at high pressure (>1 MPa), FLS particles are synthesized at pressures lower than 1 MPa. The surface area of the as-grown FLS particles is $15.7 \text{ m}^2 \text{ g}^{-1}$, while the FLS- Fe_3O_4 and FLS-Fe particles exhibit specific surface areas of $71.1 \text{ m}^2 \text{ g}^{-1}$ and $41.9 \text{ m}^2 \text{ g}^{-1}$, respectively. The decomposition of iron alkoxide, $\alpha\text{-FeOOH}$ and the removal of organic species during the thermal-annealing leaves micro- and mesopores in the FLS particles. Because of their high specific surface area, mesoporosity, and intrinsic reactivity, FLS- Fe_3O_4 and Fe particles exhibit an excellent ability to remove sulfur ions from aqueous solution. 0.1 g of both FLS- Fe_3O_4 and Fe remove most of the sulfur ions ($\sim 90\%$) in 12.5 mM Na_2S aqueous solution within 10 min. This suggests that the FLS particles are good absorbers of toxic H_2S in aqueous solution.

The results of the magneto rheology of the aqueous fluid containing the FLS- Fe_3O_4 particles exhibited that self-assembled FLS- Fe_3O_4 particles with rough surface provide enhanced controllability and increased colloidal network strength under applied magnetic field. FLS- Fe_3O_4 fluids demonstrate higher modulus strength and effective yield stress than spherical particle fluids. This suggests that hierarchical surfaces of FLS- Fe_3O_4 particles interlock under magnetic field and form a strong network structure.

4.2 FUTURE WORK

TiO₂ nanoparticle-based dye sensitized solar cells (DSSCs) have attracted a significant amount of interest, due to their possession of certain inherent advantages [305]. In DSSCs, a series of redox reactions occur via electrolyte, which works as an electron-transfer mediator. For continuous operation, photoexcited dye molecules need to be reduced by oxidizing the redox couple in the electrolyte. Then, the oxidized ions in the electrolyte diffuse from the photoanode to the counter electrode, and electrons are collected for the next redox reaction at the photoanode [306]. While many redox couples including I⁻/I₃⁻, Br⁻/Br₃⁻, cobalt (II/III), disulfide/thiolate, and ferrocene/ferrocenium redox mediator have been investigated, a pair of I⁻/I₃⁻ is still widely used for high performance DSSCs [307-310]. Due to the fast dye regeneration capability and the slow recombination of I₃⁻ with electrons in TiO₂, the iodine based redox couple increases the energy conversion efficiency of DSSCs to ~12% [311,312].

In spite of its outstanding electrochemical performance, the liquid electrolyte containing the redox couple of I⁻/I₃⁻ poses a problem regarding the long-term stability of DSSCs. One main limitation of the liquid electrolyte is that the volatile solvent can leak and evaporate under the dual stresses of heat and light [313]. To avoid a tradeoff between long-term stability and energy conversion efficiency, several groups have studied quasi-solid electrolyte, where nanoparticles, cross-linked gelators, or polymeric materials are added to the liquid electrolyte [314-318]. The additives form a network in the electrolyte and increase its viscosity. This solid network suppresses leakage of the electrolyte, and the liquid solvent inside the network supports the superior functioning of the redox couple. However, due to its viscosity, it is not easy to completely fill the nanopores of the mesoporous electrode with the quasi-solid electrolyte.

Unfilled pores become a source of the recombination of photogenerated electrons with oxidized sensitizers, leading to a reduction in photocurrent [319].

As mentioned above, due to the electrostatic forces between the faces and edges of the clay platelets, a unique network forms in the fluid and turns the liquid to gel [320]. When a network of nanolayers is formed, the solvent can be retained in the gel through physical and chemical interactions between the solvent and the nanolayers [321,322]. The most intriguing properties of the clay based gel are its thixotropic and shear thinning behaviors. They indicate that the gelation of the clay-based fluid occurs gradually over time, and that the transition of the clay-based fluid to the gel is reversibly controlled by applying a shear force. Nanoclay particles are also used as a gelator in fabricating the quasi-solid electrolyte of DSSCs [323,324].

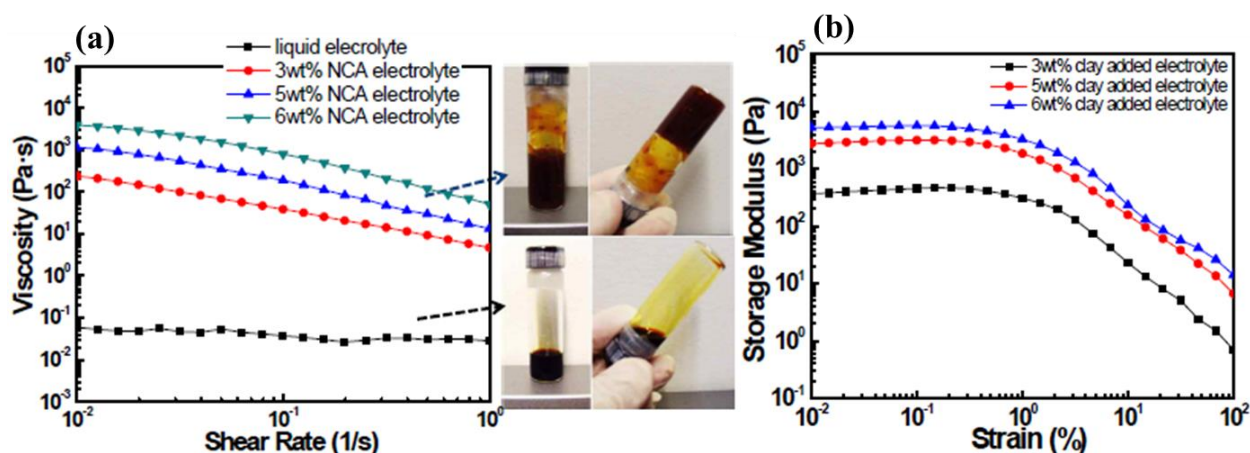


Figure 4-1 (a) Viscosity vs. shear rate curve of normal liquid electrolyte and nanoclay added electrolyte, and (b) storage modulus vs. strain amplitude curve at a fixed angular frequency of 10rad/s as a function of clay content

Figure 4-1(a) shows a shear rate-viscosity correlation of nanoclay added (NCA) electrolyte at room temperature. In comparison with a liquid electrolyte, the viscosity of NCA electrolyte dramatically increases by a 4~5 order of magnitude. As represented in the photo of the samples, the NCA electrolyte exhibit quasi-solid behavior in a static state. This observation suggests that the addition of 3~6 wt% nanoclay to the liquid electrolyte forms a strong network structure.

The viscoelastic behavior of the NCA electrolyte fluids is measured by a small amplitude oscillatory test at a fixed angular frequency of 10 rad/s. The investigation of the viscoelastic behavior of fluid systems affords to identify the inter-particle interaction which can be estimated by linear viscoelastic region (LVR), representing the stability of the quasi-solid state. As shown in Figure 4-1(b), All NCA electrolytes exhibit LVR, demonstrating evidence of separable elastic response and stress relaxation.

The preliminary experimental results on the quasi-solid electrolyte modified by nanoclay indicate its possibility to further enhance the performance and the long-term stability of the DSSC device based upon the following concepts: i) superior chemical and physical abilities of the nanoclay to retain liquid solvent ii) the formation of rigid network of nanoclay makes the electrolyte stable, and iii) promoting the function of a redox couple through grotthuss-type charge transport on the cross-linked nano clay network. Hence, the utilization of nanoclay in quasi-solid state electrolyte will be promising approach to improve both the electron transport rate and the long-term stability of the DSSC device.

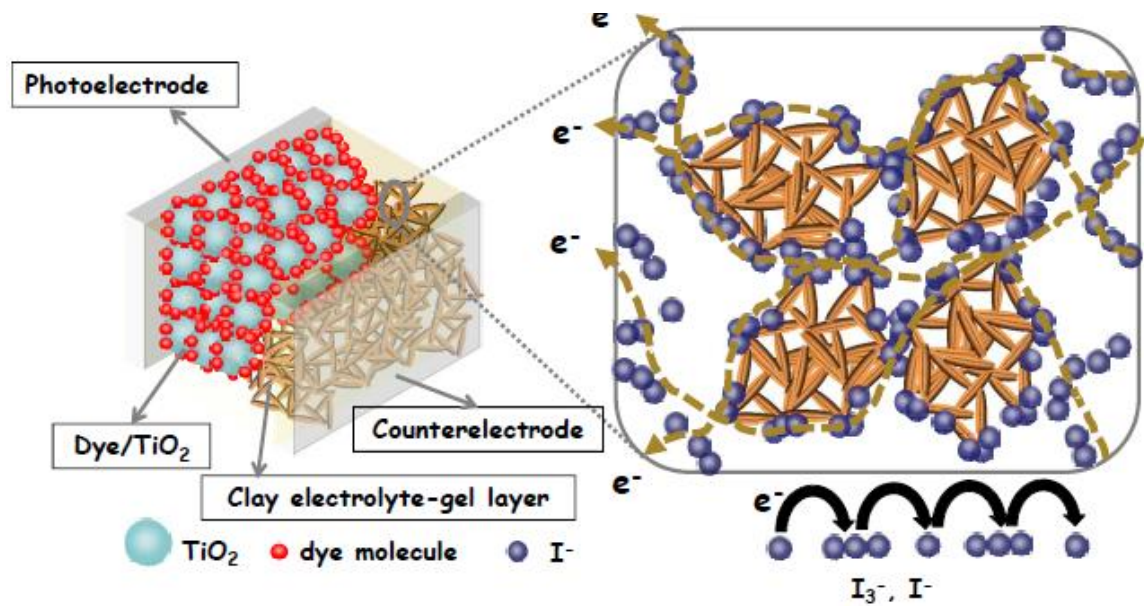


Figure 4-2 Schematic illustration representing proposed mechanism on the Grotthuss like charge transport

BIBLIOGRAPHY

- [1] C. B. Murray, D. J. Norris, M. G. Bawendi, *J. Am. Chem. Soc.*, **1993**, 115, 8706.
- [2] H. Zeng, J. Li, J. P. Liu, J. L. Wang, S. Sun, *Nature*, **2002**, 420, 395.
- [3] A. P. Alivisatos, *Science*, **1996**, 271, 933.
- [4] M. A. El-Sayed, *Acc. Chem. Res.*, **2004**, 37, 326.
- [5] V. F. Puntes, K. M. Krishnan, A. P. Alivisatos, *Science*, **2001**, 291, 2115.
- [6] J. -I. Park, J. Cheon, *J. Am. Chem. Soc.*, 2001, 123, 5743.
- [7] L. E. Brus, *J. Chem. Phys.*, 1984, 80, 4403.
- [8] N. Chestnoy, R. Hull, L. E. Brus, *J. Chem. Phys.*, **1986**, 85, 2237.
- [9] M. Steigerwald, L. E. Brus, *Acc. Chem. Res.*, 1990, 23, 183.
- [10] G. Markovich, C. P. Collier, S. E. Henrichs, F. Remacle, R. D. Levine, J. R. Heath, *Acc. Chem. Res.*, **1999**, 32, 415.
- [11] C. L. Cleveland, W. D. Luedtke, U. Landman, *Phys. Rev. B*, **1999**, 60, 5065.
- [12] A. L. Efros, A. L. Efros, *Semiconductors*, **1982**, 16, 1209.
- [13] D. J. Norris, A. L. Efros, M. Rosen, M. G. Bawendi, *Phys. Rev. B*, **1996**, 53, 16347.
- [14] L. Li, J. Hu, W. Yang, A. O. Alivisatos, *Nano Lett.*, **2001**, 1, 349.
- [15] J. Hu, L. Li, W. Yang, L. Manna, L. Wang, A. P. Alivisatos, *Science*, **2001**, 292, 2060.
- [16] A. Demortière, P. Panissod, B. P. Pichon, G. Pourroy, D. Guillon, B. Donnio, S. Bégin-Colin, *Nanoscale*, **2011**, 3, 225.
- [17] Y. Xiong, H. Cai, B. J. Wiley, J. Wang, M. J. Kim, Y. Xia, *J. Am. Chem. Soc.*, 2007, **129**, 3665.
- [18] C. Zhang, Y. Zhu, *Chem. Mater.*, **2005**, 17, 3537.

- [19] L. -S. Zhong, J. -S. Hu, H. -Pu. Liang, A. -Min. Cao, W. -G. Song, L. -J. Wan, *Adv. Mater.*, **2006**, 18, 2426.
- [20] M. P. Pileni, *Catal. Today*, **2000**, 58, 151.
- [21] M. L. Steigerwald, A. P. Alivisatos, J. M. Gibson, T. D. Harris, R. Kortan, A. J. Muller, A. M. Thayer, T. M. Duncan, D. C. Douglass, L. E. Brus, *J. Am. Chem. Soc.*, **1988**, 110, 3046.
- [22] B. A. Simmons, S. Li, V. T. John, G. L. Mcpherson, A. Bose, W. Zhou, J. He, *Nano Lett.*, **2002**, 2, 263.
- [23] D. -F. Zhang, L. -D. Sun, J. -L. Yin, C. -H. Yan, *Adv. Mater.*, **2003**, 15, 1022.
- [24] Y. Lee, J. Lee, C. J. Bae, J. -G. Park, H. -J. Noh, J. -H. Park, T. Hyeon, *Adv. Funct. Mater.*, **2005**, 15, 503.
- [25] Y. Xia, P. Yang, Y. Sun, Y. Wu, B. Mayers, B. Gates, Y. Yin, F. Kim, H. Yan, *Adv. Mater.*, **2003**, 15, 353.
- [26] E. P. A. M. Bakkers, M. A. Verheijen, *J. Am. Chem. Soc.*, 2003, 125, 3440.
- [27] Z. W. Pan, Z. R. Dai, Z. L. Wang, *Science*, **2001**, 291, 1947.
- [28] Y. Saito, T. Matsumoto, *Nature*, **1998**, 392, 237.
- [29] J. Goldberger, R. He, Y. Zhang, S. Lee, H. Yan, H. -J. Choi, P. Yang, *Nature*, **2003**, 422, 599.
- [30] W. Y. Kong, Y. Ding, R. S. Yang, Z. L. Wang, *Science*, **2004**, 303, 1348.
- [31] Z. W. Pan, Z. R. Dai, L. Xu, S. T. Lee, Z. L. Wang, *J. Phys. Chem., B*, **2001**, 105, 2507.
- [32] C. Ma, Y. Ding, D. Moore, X. Wang, Z. L. Wang, *J. Am. Chem. Soc.*, **2004**, 126, 708.
- [33] Y. Zhang, L. Wang, X. Liu, Y. Yan, C. Chen, J. Zhu, *J. Phys. Chem. B*, **2005**, 109, 13091.
- [34] R. Elghanian, J. J. Storhoff, R. C. Mucic, R. L. Letsinger, C. A. Mirkin, *Science*, **1997**, 277, 1078.
- [35] G. Schmid, Y. P. Liu, *Nano Lett.*, **2001**, 1, 405.
- [36] W. Lu, Z. Q. Ji, L. Pfeiffer, K. W. West, A. J. Rimberg, *Nature*, **2003**, 423, 422.
- [37] C. T. Black, C. B. Murray, R. L. Sandstrom, S. Sun, *Science*, **2000**, 290, 1131.
- [38] S. Sun, C. B. Murray, D. Weller, L. Folks, A. Moser, *Science*, **2000**, 287, 1989.

- [39] T. J. Trentler, K. M. Hickman, S. C. Goel, A. M. Viano, P. C. Gibbons, W. E. Buhro, *Science*, **1995**, 270, 1791.
- [40] W. E. Buhro, K. M. Hickman, T. J. Trentler, *Adv. Mater.*, **1996**, 8, 8.
- [41] R. A. Laudise, *The Growth of Single Crystals*, Prentice-Hall, Englewood Cliffs, NJ, **1970**, 86.
- [42] F. Rodríguez-Reinoso, J. Narciso, *Adv. Mater.*, **1995**, 7, 209.
- [43] M. Yazawa, M. Koguchi, A. Muto, K. Hiruma, *Adv. Mater.*, **1993**, 5, 577.
- [44] F. Wang, A. Dong, J. Sun, R. Tang, H. Yu, W. E. Buhro, *Inorg. Chem.*, **2006**, 45, 7511.
- [45] R. L. Penn, J. F. Banfield, *Science*, **1998**, 281, 969.
- [46] C. Pacholski, A. Kornowski, H. Weller, *Angew. Chem. Int. Ed.*, **2002**, 41, 1188.
- [47] X. W. Lou, H. C. Zeng, *J. Am. Chem. Soc.*, **2003**, 125, 2697.
- [48] B. Liu, H. C. Zeng, *J. Am. Chem. Soc.*, **2003**, 125, 4430.
- [49] B. Liu, H. C. Zeng, *J. Am. Chem. Soc.*, **2004**, 126, 8124.
- [50] T. Sugimoto, *Adv. Colloid Interface Sci.*, **1987**, 28, 65.
- [51] J. W. Mullin, *Crystallization* (3rd Edition), Butterworth-Heinemann, Stoneham, MA, **1997**.
- [52] H. L. Zhu, R. S. Averback, *Philos. Mag. Lett.*, **1996**, 73, 27.
- [53] M. Yeadon, M. Ghaly, J. C. Yang, R. S. Averback, J. M. Gibson, *Appl. Phys. Lett.*, **1998**, 73, 3208.
- [54] H. Zhang, F. Huang, B. Gilbert, J. F. Banfield, *J. Phys. Chem. B*, **2003**, 107, 13051.
- [55] Y. Jun, M. F. Casula, J. -H. Sim, S. Y. Kim, J. Cheon, A. P. Alivisatos, *J. Am. Chem. Soc.*, **2003**, 125, 15981.
- [56] P. D. Cozzoli, A. Kornowski, H. Weller, *J. Am. Chem. Soc.*, **2003**, 125, 14539.
- [57] L. Manna, E. C. Scher, A. P. Alivisatos, *J. Am. Chem. Soc.*, **2000**, 122, 12700.
- [58] A. Ghezelbash, B. A. Korgel, *Langmuir*, **2005**, 21, 9451.
- [59] M. B. Sigman, Jr., A. Ghezelbash, T. Hanrath, A. E. Saunders, F. Lee, B. A. Korgel, *J. Am. Chem. Soc.*, **2003**, 125, 16050.
- [60] A. Ghezelbash, M. B. Sigman, Jr., B. A. Korgel, *Nano Lett.*, **2004**, 4, 537.

- [61] Y. Jun, S. –M. Lee, N. –J. Kang, J. Cheon, *J. Am. Chem. Soc.*, **2001**, 123, 5150.
- [62] Y. Jun, Y. Jung, J. Cheon, *J. Am. Chem. Soc.*, **2002**, 124, 615.
- [63] Y. –H. Kim, Y. Jun, B. –H. Jun, S. –M. Lee, J. Cheon, *J. Am. Chem. Soc.*, **2002**, 124, 12656.
- [64] K. L. Hull, J. W. Grebinski, T. H. Kosel, M. Kuno, *Chem. Mater.*, **2005**, 17, 4416.
- [65] J. Lu, P. Qi, Y. Peng, Z. Yang, W. Yu, Y. Qian, *Chem. Mater.*, **2001**, 13, 2169.
- [66] O. Zwlaya-Angel, J. J. Alvaradi-Gel, R. Loxada-Morales, H. Vargas, A. R. Silva, *Phys. Lett.*, **1994**, 64, 291.
- [67] A. Corma, *Chem. Rev.*, **1997**, 97, 2373.
- [68] T. J. Pinnavaia, *ACS Ad. Chem. Ser.*, **1995**, 245, 283.
- [69] P. T. Tanev, J. –R. Butruille, T. J. Pinnavaia, In: Interrante L V, Hampden-Smith M J (eds.) *Chemistry of Advanced Materials*: Wiley-VCH, NY, **1998**, 329.
- [70] A. Vaccari, *Appli. Clay Sci.*, **1999**, 14, 161.
- [71] R. F. Giese, Jr., *Clays Clay Miner.*, **1975**, 23, 165.
- [72] Z. Ding, J. T. Klopogge, R. L. Frost, G. Q. Lu, H. Y. Zhu, *J. Porous Mater.*, **2001**, 273.
- [73] R. S. Varma, *Tetrahedron*, **2002**, 58, 1235.
- [74] X. Fan, C. Xia, R. C. Advincula, *Langmur*, **2005**, 21, 2537.
- [75] G. Bossis, O. Volkova, S. Lacis, A. Meunier, Magnetorheology: Fluids, Structures and Rheology, in: S. Odenbach (Ed) *Ferrofluids. Magnetically controllable fluids and their applications* (Lecture Notes in Physics; 594; Springer-Verlag 2002), 202.
- [76] C. –H. Lee, M. –G. Jang, *Sensors*, **2011**, 11, 2845.
- [77] D. J. Klingenberg, *AIChE J.*, 2001, 47, 246.
- [78] B. N. Reinecke, J. W. Shan, K. K. Suabedissen, A. S. Cherkasova, *J. Appl. Phys.*, **2008**, 104, 023507.
- [79] J. Liu, G. A. Flores, R. Sheng, *J. Magn. Magn. Mater.*, **2001**, 225, 209.
- [80] W. Kordonski, D. Golini, *J. Intell. Mater. Syst. Struct.*, **2002**, 13, 401.
- [81] F. Donado, J. L. Carrillo, M. E. Mendoza, *J. Phys.: Condens. Matter.*, **2002**, 14, 2153.
- [82] D. H. Read, J. E. Martin, *Anal. Chem.*, **2010**, 82, 2150.

- [83] A. T. Skjeltorp, *Phys. Rev. Lett.*, **1983**, 51, 2306.
- [84] R. E. Rosensweig, *Ferrohydrodynamics*, dover, NY, **1997**.
- [85] B. J. de Gans, N. J. Duin, D. van den Ende, J. Mellema, *J. Chem. Phys.*, **2002**, 113, 2032.
- [86] R. Saldivar-Guerrero, R. Richter, I. Rehberg, N. Aksel, L. Heymann, O. S. Rodriguez-Fernández, *J. Chem. Phys.*, **2006**, 125, 084907.
- [87] A. P. Gast, C. F. Zukoski, *Adv. Colloid Interface Sci.*, **1989**, 30, 153.
- [88] J. Bibette, *J. Magn. Magn. Mater.*, **1993**, 122, 37.
- [89] M. Zrinyi, *Colloid Polym. Sci.*, **2000**, 278, 98.
- [90] W. H. Li, Y. Zhou, T. F. Tian, *Rheol. Acta*, **2010**, 49, 733.
- [91] J. H. E. Promislow, A. P. Gast, M. Fermigier, *J. Chem. Phys.*, **1995**, 102, 5492.
- [92] E. M. Furst, A. P. Gast, *Phys. Rev. Lett.*, **1999**, 82, 4130.
- [93] J. F. Brady, G. Bossis, *Ann. Rev. Fluid. Mech.*, **1988**, 10, 111.
- [94] R. T. Bonnecaze, J. F. Brady, *J. Rheol.*, **1992**, 36, 73.
- [95] H. Heller, R. Keren, *Clays Clay Miner.*, **2001**, 49, 286.
- [96] M. M. Ramos-Tehada, F. J. Arrovo, R. Peren, J. D. G. Duran, *J. Colloid Interface Sci.*, **2001**, 235, 251.
- [97] E. Tombácz, M. Szekeres, *Appl. Clay Sci.*, **2004**, 27, 75.
- [98] S. Laribi, J. M. Fleureua, J. L. Grossiord, N. kbir-Ariguib, *Clays Clay Miner.*, **2006**, 54, 29.
- [99] T. Missana, A. J. Adell, *J. Colloid Interface Sci.*, **2000**, 230, 150.
- [100] S. Abend, G. Lagaly, *Appl. Clay Sci.*, **2000**, 16, 201.
- [101] G. Lagaly, S. Ziesmer, *Adv. Colloid Interface Sci.*, **2003**, 100, 105.
- [102] H. Schott, *J. Colloid Interface Sci.*, **1968**, 26, 133.
- [103] L. E. Kuznetsova, N. N. Serb-Serbina, *Kolloidn. Zh.*, **1968**, 30, 853.
- [104] D. Heath, Th. F. Tadros, *J. Colloid Interface Sci.*, **1983**, 83, 307.
- [105] P. Liu, *Appl. Clay Sci.*, **2007**, 38, 64.

- [106]M. Manitiu, S. Horsch, E. Gulari, R. M. Kannan, *Polymer*, **2009**, 50, 3786.
- [107]L. M. C. Dykes, J. M. Torkelson, W. R. Burghardt, R. Krishnamoorti, *Polymer*, **2010**, 51, 4916.
- [108]J. C. Baird, J. Y. Walz, *J. Colloid Interface Sci.*, **2007**, 306, 411.
- [109]E. Tombácz, C. Csanaky, E. Illés, *Colloid Polym. Sci.*, **2001**, 279, 484.
- [110]Y. –H. Son, J. –K. Lee, Y. Soong, D. Martello, M. Chyu, *Chem. Mater.*, **2010**, 22, 2226.
- [111]J. –H. Choy, S. –Y. Kwak, S. –Y. Han, B. –W. Kim, *Mater. Lett.*, **1997**, 33, 143.
- [112]A. Walcarius, M. Etienne, C. Delacote, *Anal. Chim. Acta*, **2004**, 508, 87.
- [113]L. Bois, A. Bonhommé, A. Ribes, B. Pais, G. Raffin, F. Tessier, *Colloids Surf., A*, **2003**, 221, 221.
- [114]A. B. Bourlinos, D. D. Chowdhury, Y. –U. An, Q. Zhang, L. A. Archer, E. P. Giannelis, *Small*, **2005**, 1, 80.
- [115]M. L. Occelli, *J. Mol. Catal.*, **1986**, 35, 377.
- [116]M. L. Occelli, In proceedings of the international Clay Conference; Denver, 1985; Clay Minerals Society: Chantilly, VA, **1985**, 319.
- [117]E. G. Rightor, M. –S. Tzou, T. J. Pinnavaia, *J. Catal.*, **1991**, 130, 29.
- [118]S. H. Xu, S. A. Boyd, *Adv. Agron.*, **1997**, 59, 25.
- [119]J. Breu, C. R. A. Catlow, *Inorg. Chem.*, **1995**, 34, 4504.
- [120]Z. Ai, K. Deng, Q. Wan, L. Zhang, S. Lee, *J. Phys. Chem. C*, **2010**, 114, 6237.
- [121]R. E. Grim, *Clay Mineralogy*, 2nd ed.; McGraw-Hill: NY, **1968**, 596.
- [122]L. Fowden, R. M. Barrer, P. B. Tinker, *Clay Minerals; Their Structure, Behaviour and Use*; Royal Society Chemistry, London, 1984.
- [123]S. H. Hu, T. Y. Liu, H. Y. Huang, D. M. Liu, S. Y. Chen, *Langmuir*, **2008**, 24, 239.
- [124]F. Y. Cheng, C. H. Su, Y. S. Yang, C. S. Yeh, C. Y. Tsai, C. L. Wu, M. T. Wu, D. B. Shieh, *Biomaterials*, **2005**, 26, 729.
- [125]C. L. Lin, C. F. Lee, W. Y. Chiu, *J. Colloid Interface Sci.*, **2005**, 291, 411.
- [126]L. C. A. Oliveira, D. I. Petkowicz, A. Smaniottob, S. B. C. Pergherb, *Water Res.*, **2004**, 38, 3699.

- [127]L. C. A. Oliveira, R. V. R. A. Rios, J. D. Fabris, K. Sapag, V. K. Garg, R. M. Lago, *Appl. Clay Sci.*, **2003**, 22, 169.
- [128]N. A. Booker, D. Keir, A. J. Priestley, C. B. Ritchie, D. L. Sudarmana, M. A. Woods, *Water Sci. Technol.*, **1991**, 23, 1703.
- [129]J. D. Orbell, L. Godhino, S. W. Bigger, T. M. Nguyen, L. N. Ngeh, *J. Chem. Educ.*, **1997**, 74, 1446.
- [130]R. –S. Hsu, W. –H. Chang, J. –J. Lin, *ACS Appl. Mater. Interfaces*, **2010**, 2, 1349.
- [131]S. Laribi, J. –M. Fleureau, J. –L. Grossiord, N. Kbir-Ariguib, *Clay Clay Miner.*, 2006, 54, 29.
- [132]L. Fowden, R. M. Barrer, P. B. Tinker, *Clay Minerals*, The Royal Society, London, **1984**.
- [133]P. F. Luckham, S. Rossi, *Adv. Colloid Interface Sci.*, **1999**, 82, 43.
- [134]A. Tomlinson, *J. Porous Mater.*, **1998**, 5, 259.
- [135]R. E. Grim, *Clay Mineralogy*, 2nd edition, McGraw-Hill, NY, 596, **1968**.
- [136]C. E. Marchall, Z. Kristallogr, *Mineral*, **1935**, 91, 433.
- [137]C. T. Johnston, E. Tombácz, Soil Science Society of America, Madison, WI, 37, **2002**.
- [138]E. C. Bingham, *Fluidity and Plasticity*, McGraw-Hill, **1922**.
- [139]N. Casson, in: C. C. Mills (Ed), *Rheology of Disperse Systems*, **1959**, 84.
- [140]W. Hershel, J. Buckley, *Proc. Am. Soc. Test of Materials*, **1926**, 26, 621.
- [141]N. J. Alderman, A. Gavignet, D. Guillot, G. C. Maitland, SPE 18035, 63rd, Ann. Tech. Conf., Houston, **1988**, 99, 187.
- [142]A. Gil, M. A. Vicente, S. A. Korili, *J. Catal.*, **2005**, 229, 119.
- [143]A. Gil, L. M. Gandia, *Chem. Eng. Sci.*, **2003**, 58, 3059.
- [144]Y. –S. Jung, D. –W. Kim, Y. –S. Kim, E. –K. Park, S. –H. Baeck, *J. Phys. Chem. Solids*, **2008**, 69, 1464.
- [145]G. C. Bye, G. T. Simpkin, *J. Am. Ceram. Soc.*, **1974**, 8, 367.
- [146]Y. S. Lin, *J. Mater. Sci.*, **1991**, 26, 715.
- [147]V. Gunay, In proceedings of the Third Euro-Ceramics Society Conference; Madrid, Spain; European Ceramics Society: Bologna, Italy, **1993**, 267.

- [148]M. Kumagi, G. L. Messing, *J. Am. Ceram. Soc.*, **1984**, C-230-C231.
- [149]H. Van Olphen, *Introduction to Clay Colloid Chemistry*, 2nd ed., Wiley & Sons, NY, 1977.
- [150]L. –M. Zhang, C. Jahns, B. S. Hsiao, B. Chu, *Colloid Interface Sci.*, **2003**, 266, 339.
- [151]B. Niraula, T. C. King, M. Misran, *Colloids Surf. A*, **2004**, 251, 59.
- [152]J. Zhao, A. B. Morgan, J. D. Harris, *Polymer*, **2005**, 46, 8641.
- [153]J. W. Mullin, *Crystallization*, 4th ed., Butterworth Heinemann, Boston, **2001**.
- [154]L. Manna, E. C. Scher, A. P. Alivisatos, *J. Am. Chem. Soc.*, **2000**, 122, 12700.
- [155]B. J. Briscoe, P. F. Luckham, S. R. Ren, *Trans. R. Soc. London, Ser. A*, **1994**, 348, 179.
- [156]H. Van Olphen, Proceedings of the Fourth National Conference on Clays and Clay Minerals; University Park, PA, 1955; National Academy of Sciences: Washington, D. C., 1956, 9, 204.
- [157]N. J. Alderman, A. Gavignet, D. Guillot, G. C. Maitland, SPE 63rd Annual Technical Conference and Exhibition; Houston, TX, 1988; Society of Petroleum Engineers: Richardson, TX, 1988, 187.
- [158]O. Duman, S. Tunc, *Microporous Mesoporous Mater.*, **2009**, 117, 331.
- [159]V. M. Gun'ko, V. L. Zarko, R. Leboda, E. Chibowski, *Adv. Colloid Interface Sci.*, **2001**, 91,1.
- [160]H. Van Olphen, *J. Colloid Interface Sci.*, **1964**, 19, 313.
- [161]W. W. Yu, J. C. Falkner, C. T. Yavuz, V. L. Covin, *Chem. Commun.*, **2004**, 2306.
- [162]J. J. Lin, I. J. Cheng, C. C. Chou, *Macromol. Rapid Commun.*, **2003**, 24, 492.
- [163]S. Sun, H. Zeng, *J. Am. Chem. Soc.*, **2002**, 124, 8204.
- [164]J. Park, E. Lee, N. –M. Hwang, M. Kang, S. C. Kim, Y. Hwang, J. –G. Park, H. –J. Noh, J. –Y. Kim, J. –H. Park, T. Hyeon, *Angew. Chem. Int. Ed.*, **2005**, 44, 2872.
- [165]Y. –H. Son, J. –K. Lee, Y. Soong, D. Martello, M. Chyu, *Appl. Phys. Lett.*, **2010**, 96, 121905.
- [166]Y. Jung, Y. –H. Son, J. –K. Lee, *RSC Advances*, **2012**, 2, 5877.
- [167]Y. Jung, Y. –H. Son, J. –K. Lee, *ACS Appl. Mater. Interfaces*, **2011**, 3, 3515.
- [168]L. –M. Zhang, C. Jahns, B. S. Hsiao, B. Chu, *J. Colloid Interface Sci.*, **2003**, 266, 339.

- [169]B. Niraula, T. C. King, M. Misran, *Colloids Surf., A*, **2004**, 251, 59.
- [170]X. Song, L. Gao, *J. Phys. Chem. C*, **2008**, 112, 15299.
- [171]X. Fu, H. Feng, K. Ng, *Nanotechnology*, **2009**, 20, 375601.
- [172]S. K. Mohapatra, S. E. John, S. Banerjee, M. Misra, *Chem. Mater.*, **2009**, 21, 3048.
- [173]S. Liu, R. Xing, F. Lu, R. Rana, J. Zhu, *J. Phys. Chem. C*, **2009**, 113, 21042.
- [174]S. Guo, L. Wang, E. Wang, *Chem. Commun.*, **2007**, 3163.
- [175]B. Liu, H. C. Zeng, *J. Am. Chem. Soc.*, **2004**, 126, 8124.
- [176]B. B. Kale, J. O. Baeg, S. M. Lee, H. Chang, S. J. Moon, C. W. Lee, *Adv. Funct. Mater.*, **2006**, 16, 1349.
- [177]Y. Hou, H. Kongdoh, T. Ohta, *Chem. Mater.*, **2005**, 17, 3994.
- [178]L. S. Zhong, J. S. Hu, H. P. Liang, A. M. Cao, W. G. Song, L. J. Wan, *Adv. Mater.*, **2006**, 18, 2426.
- [179]X. M. Sun, J. F. Liu, Y. D. Li, *Chem. –Eur. J.*, **2006**, 12, 2036.
- [180]J. Zhang, S. Wang, M. Xu, Y. Wang, B. Zhu, S. Zhang, W. Huang, S. Wu, *Cryst. Growth Des.*, **2009**, 9, 3532.
- [181]X. Yin, C. Li, M. Zhang, Q. Hao, S. Liu, Q. Li, L. Chen, T. Wang, *Nanotechnology*, **2009**, 20, 455503.
- [182]C. Li, L. Li, Z. Du, H. Yu, Y. Xiang, Y. Li, Y. Cai, T. Wang, *Nanotechnology*, **2008**, 19, 35501.
- [183]F. Zhang, H. Yang, X. Xie, L. Li, L. Zhang, J. Yu, H. Zhao, B. Liu, *Sens. Actuators, B*, **2009**, 141, 381.
- [184]F. Song, H. Su, J. Han, D. Zhang, Z. Chen, *Nanotechnology*, **2009**, 20, 495502.
- [185]L. –S. Zhong, J. –S. Hu, H. –P. Liang, A. –M. Cao, W. –G. Song, L. –J. Wan, *Adv. Mater.*, **2006**, 18, 2426.
- [186]M. Cao, T. Liu, S. Gao, G. Sun, X. Wu, C. Hu, Z. Wang, *Angew. Chem., Int. Ed.*, **2005**, 44, 4197.
- [187]J. Gu, S. Li, E. Wang, Q. Li, G. Sun, R. Xu, H. J. Zhang, *J. Solid State Chem.*, **2009**, 182, 1265.
- [188]G. Shen, Y. Bando, C. Tang, D. Golberg, *J. Phys. Chem. B*, **2006**, 110, 7199.

- [189]Y. Huang, K. Yu, Z. Zhu, *Curr. Appl. Phys.*, **2007**, 7, 702.
- [190]F. Zhou, X. Zhao, C. Yuan, L. Li, *Cryst. Growth Des.*, **2008**, 8, 723.
- [191]S. -W. Cao, Y. -J. Zhu, M. -Y. Ma, L. Li, L. Zhang, *J. Phys. Chem. C*, **2008**, 112, 1851.
- [192]R. G. Deshmukh, S. S. Badadhe, I. S. Mulla, *Mater. Res. Bull.*, **2009**, 44, 1179.
- [193]X. Hu, J. C. Yu, J. Gong, *J. Phys. Chem. C*, **2007**, 111, 11180.
- [194]B. Hu, S. B. Wang, K. Wang, M. Zhang, S. H. Yu, *J. Phys. Chem. C*, **2008**, 112, 11169.
- [195]G. Xi, Y. He, Q. Zhang, H. Xiao, X. Wang, C. Wang, *J. Phys. Chem. C*, **2008**, 112, 11645.
- [196]L. Xu, Y.-S. Ding, C.-H. Chen, L. Zhao, C. Rimkus, R. Joesten, S. L. Suib, *Chem. Mater.*, **2008**, 20, 308.
- [197]A. L. Washington, G. F. Strouse, II, *J. Am. Chem. Soc.*, **2008**, 130, 8916.
- [198]X. Cao, C. Zhao, X. Lan, G. Gao, W. Qian, Y. Guo, *J. Phys. Chem. C*, **2007**, 111, 6658.
- [199]Z. Li, B. Tan, M. Allix, A. I. Cooper, M. J. Rosseinsky, *Small*, **2008**, 4, 231.
- [200]F. Caruso, M. Spasova, A. Sussha, M. Giersig, R. A. Caruso, *Chem. Mater.*, **2001**, 13, 109.
- [201]T. Hyeon, S. S. Lee, J. Park, Y. Chung, H. B. Na, *J. Am. Chem. Soc.*, **2001**, 123, 12798.
- [202]S. Yu, M. Yoshimur, *Adv. Funct. Mater.*, **2002**, 12, 9.
- [203]G. Zou, K. Xiong, C. Jiang, H. Li, T. Li, J. Du, Y. Qian, *J. Phys. Chem. B*, **2005**, 109, 18356.
- [204]D. Yu, X. Sun, J. Zou, Z. Wang, F. Wang, K. Tang, *J. Phys. Chem. B*, **2006**, 110, 21667.
- [205]Z. Sun, H. Yuan, Z. Liu, B. Han, Z. Zhang, *Adv. Mater.*, **2005**, 17, 2993.
- [206]D. Zhang, Z. Liu, S. Han, C. Li, B. Lei, M. P. Stewart, J. M. Tour, C. Zhou, *Nano Lett.*, **2004**, 4, 2151.
- [207]R. Abu-Reziq, H. Alper, D. Wang, M. L. Post, *J. Am. Chem. Soc.*, **2006**, 128, 5279.
- [208]G. Lv, F. He, X. Wang, F. Gao, G. Zhang, T. Wang, H. Jiang, C. Wu, D. Guo, X. Li, B. Chen, Z. Gu, *Langmuir*, **2008**, 24, 2151.
- [209]Z. Liu, J. Wang, D. H. Xie, G. Chen, *Small*, **2008**, 4, 462.

- [210] A. L. Kohl, F. S. Riesenfeld, *Gas Purification*, Gulf Publishing Co., Houston, 4th edn, 1985, Chp. 4, 278.
- [211] B. G. Cox, P. F. Clarke, B. B. Pruden, *Int. J. Hydrogen Energy*, **1998**, 23, 531.
- [212] L. M. Al-Shamma, S. A. Naman, *Int. J. Hydrogen Energy*, **1989**, 14, 173.
- [213] F. Bandermann, K. -B. Harder, *Int. J. Hydrogen Energy*, **1982**, 7, 471.
- [214] M. Yumura, E. Furimsky, *Appl. Catal.*, **1985**, 16, 157.
- [215] A. Davydov, K. T. Chuang, A. R. Sanger, *J. Phys. Chem. B*, **1998**, 102, 4745.
- [216] J. Wieckowska, *Catal. Today*, **1995**, 24, 405.
- [217] L. Zhang, S. Z. Qiao, Y. G. Jin, H. G. Yang, S. Budihartono, F. Stahr, Z. F. Yan, X. L. Wang, Z. P. Hao, G. Q. Lu, *Adv. Funct. Mater.*, **2008**, 18, 3203.
- [218] M. Mikhaylova, D. K. Kim, C. C. Berry, A. Zagorodni, M. Toprak, A. S. G. Curtis, M. Muhammed, *Chem. Mater.*, **2004**, 16, 2344.
- [219] T. J. Daou, G. Pourroy, S. Bégin-Colin, J. M. Grenéche, C. Ulhaq-Bouillet, P. Legaré, P. Bernhardt, C. Leuvrey, G. Rogez, *Chem. Mater.*, **2006**, 18, 4399.
- [220] Y. Lee, J. Lee, C. J. Bae, J.-G. Park, H.-J. Noh, J.-H. Park, T. Hyeon, *Adv. Funct. Mater.*, **2005**, 15, 503.
- [221] Z. B. Huang, Y. Q. Zhang, F. Q. Tang, *Chem. Commun.*, **2005**, 342.
- [222] Ch. R. Strauss, R. W. Trainor, *Aust. J. Chem.*, **1995**, 48, 1665.
- [223] C. O. Kappe, *Angew. Chem., Int. Ed.*, **2004**, 43, 6250.
- [224] C. O. Kappe, D. Dallinger, S. S. Murphree, *Practical Microwave Synthesis for Organic Chemists*, Wiley-VCH: Weinheim, 2009.
- [225] B. L. Hayes, *Microwave Synthesis: Chemistry at the Speed of Light*, CEM Publishing, Matthews, 2002.
- [226] I. Bilecka, M. Niederberger, *Nanoscale*, **2010**, 2, 1358.
- [227] D. M. P. Mingos, D. R. Baghurst, *Chem. Soc. Rev.*, **1991**, 20, 1.
- [228] C. Gabriel, S. Gabriel, E. H. Grant, B. S. J. Halstead, D. M. P. Mingos, *Chem. Soc. Rev.*, **1998**, 27, 213.
- [229] W. A. Herrmann, V. P. H. Bohm, C. P. Reisinger, *J. Organomet. Chem.*, **1999**, 576, 23.

- [230] Y. Wada, H. Kuramoto, J. Anand, T. Kitamura, T. Sakata, H. Mori, S. Yanagida, *J. Mater. Chem.*, **2001**, 11, 1936.
- [231] A. Hoz, A. Díaz-Ortiz, A. Moreno, *Chem. Soc. Rev.*, **2005**, 34, 164.
- [232] J. S. Schanche, *Mol. Diversity*, **2003**, 7, 291.
- [233] X. Zhu, Q. Zhang, Y. Li, H. Wang, *J. Mater. Chem.*, **2010**, 20, 1766.
- [234] D. Dallinger, M. Irfan, A. Suljanovic, C. O. Kappe, *J. Org. Chem.*, **2010**, 75, 5278.
- [235] X. Zhang, D. O. Hayward, D. M. P. Mingos, *Catal. Lett.*, **2003**, 88, 33.
- [236] K. J. Rao, B. Vaidhyathan, M. Ganguli, P. A. Ramakrishnan, *Chem. Mater.*, **1999**, 11, 882.
- [237] W. C. Conner, G. A. Tompsett, *J. Phys. Chem. B*, **2008**, 112, 2110.
- [238] S. J. Vallee, W. C. Conner, *J. Phys. Chem. B*, **2006**, 110, 15459.
- [239] X. Hu, J. C. Yu, J. Gong, Q. Li, G. Li, *Adv. Mater.*, **2007**, 19, 2324.
- [240] X. Hu, J. C. Yu, *Adv. Funct. Mater.*, **2008**, 18, 880.
- [241] C. de Mello Donegà, P. Liljeroth, D. Vanmaekelbergh, *Small*, **2005**, 1, 1152.
- [242] P. Periyat, N. Leyland, D. E. McCormack, J. Colreavy, D. Corr, S. C. Pillai, *J. Mater. Chem.*, **2010**, 20, 3650.
- [243] T. Yamamoto, Y. Wada, H. Yin, T. Sakata, H. Mori, S. Yanagida, *Chem. Lett.*, **2002**, 964.
- [244] V. G. Pol, Y. Langzam, A. Zaban, *Langmuir*, **2007**, 23, 11211.
- [245] M. Z. C. Hu, M. T. Harris, C. H. Byers, *J. Colloid Interface Sci.*, **1998**, 198, 87.
- [246] C. O. Kappe, D. Dallinger, S. S. Murphree, *Practical Microwave Synthesis for Organic Chemists – Strategies, Instruments, and Protocols*, Wiley-VCH, Weinheim, **2009**.
- [247] C. O. Kappe, *Chem. Soc. Rev.*, **2008**, 37, 1127.
- [248] P. Lidström, J. Tierney, B. Wathey, J. Westman, *Tetrahedron*, **2001**, 57, 9225.
- [249] J. Berlan, P. Giboreau, S. Lefeuvre, C. Marchand, *Tetrahedron Lett.*, **1991**, 32, 2363.
- [250] M. Godinho, C. Ribeiro, E. Longo, E. R. Leite, *Cryst. Growth Des.*, **2008**, 8, 384.
- [251] I. Bilecka, I. Djerdj, M. Niederberger, *Chem. Commun.*, **2008**, 886.

- [252]E. Caponetti, L. Pedone, R. Massa, *Mater. Res. Innovations*, **2004**, 8, 44.
- [253]E. K. Nyutu, C. –H. Chen, P. K. Dutta, S. L. Suib, *J. Phys. Chem. C*, **2008**, 112, 9659.
- [254]J. Geng, W. –H. Hou, Y. –N. Lv, J. –J. Zhu, H. –Y. Chen, *Inorg. Chem.*, **2005**, 44, 8503.
- [255]R. L. Penn, G. Oskam, T. J. Strathmann, P. C. Searson, A. T. Stone, D. R. Veblen, *J. Phys. Chem. B*, **2001**, 105, 2177.
- [256]Z. A. Peng, X. G. Peng, *J. Am. Chem. Soc.*, **2001**, 123, 1389.
- [257]L. Vayssieres, *Adv. Mater.*, **2003**, 15, 464.
- [258]Z. Liu, Z. Hu, J. Liang, S. Li, Y. Yang, S. Peng, Y. Qian, *Langmuir*, **2004**, 20, 214.
- [259]A. Le’austic, F. Bahonneau, J. Livage, *Chem. Mater.*, **1989**, 1, 248.
- [260]X. Jiang, Y. Wang, T. Herricks, Y. Xia, *J. Mater. Chem.*, **2004**, 14, 695.
- [261]A. Ghezelbash, B. A. Korgel, *Langmuir*, **2005**, 21, 9451.
- [262]A. Ghezelbash, M. B. Sigman, Jr., B. A. Korgel, *Nano Lett.*, **2004**, 4, 537.
- [263]Y. P. Zhao, D. X. Ye, G. C. Wang, T. M. Lu, *Nano Lett.*, **2002**, 2, 351.
- [264]Y. Politi, T. Arad, E. Klein, S. Weiner, L. Addadi, *Science*, **2004**, 306, 1161.
- [265]G. Wei, W. Qin, W. Han, W. Yang, F. Gao, G. Jing, R. Kim, D. Zhang, K. Zheng, L. Wang, L. Liu, *J. Phys. Chem. C*, **2009**, 113, 19432.
- [266]S. Zeng, K. Tang, T. Li, Z. Liang, D. Wang, Y. Wang, Y. Qi, W. Zhou, *J. Phys. Chem. C*, **2008**, 112, 4836.
- [267]W. K. Burton, N. Cabrera, F. C. Frack, *Philos. Trans. R. Soc. A*, **1951**, 243, 299.
- [268]X. Wang, J. J. Zhuang, K. Chen, B. Zhou, Y. D. Li, *Angew. Chem. Int. Ed.*, **2004**, 43, 2017.
- [269]M. –L. Li, Q. –Z. Yao, G. –T. Zhou, S. –Q. Fu, *CrystEngComm*, **2010**, 12, 3138.
- [270]A. M. Cao, J. S. Hu, H. P. Liang, L. J. Wan, *Angew. Chem., Int. Ed.*, **2005**, 44, 4391.
- [271]Y. L. Wang, X. C. Jiang, Y. N. Xia, *J. Am. Chem. Soc.*, **2003**, 125, 16176.
- [272]X. C. Jiang, Y. L. Wang, T. Herricks, Y. N. Xia, *J. Mater. Chem.*, **2004**, 14, 695.
- [273]N. Kijima, M. Yoshinaga, J. Awaka, J. Akimoto, *Solid State Ionics*, **2011**, 192, 293.

- [274] V. M. Aroutiounian, V. M. Arakelyan, G. E. Shahnazaryan, H. R. Hovhannisyan, J. A. Turner, *Sol. Energy*, **2007**, 81, 1369.
- [275] M. Zhu, G. Diao, *J. Phys. Chem. C*, **2011**, 115, 18923.
- [276] E. K. Nyutu, W. C. Conner, S. M. Auerbach, C. -H. Chen, S. L. Suib, *J. Phys. Chem. C*, **2008**, 112, 1407.
- [277] L. Chen, X. Yang, J. Chen, J. Liu, H. Wu, H. Zhan, C. Liang, M. Wu, *Inorg. Chem.*, **2010**, 49, 8411.
- [278] X. Su, C. Yu, C. Qiang, *Appl. Surf. Sci.*, **2011**, 257, 9014.
- [279] D. L. A. de Faria, S. Venâncio Silva, M. T. de Oliveira, *J. Raman Spectrosc.*, **1997**, 28, 873.
- [280] N. Pinna, S. Grancharov, P. Beato, P. Bonville, M. Antonietti, M. Niederberger, *Chem. Mater.*, **2005**, 17, 3044.
- [281] T. Fan, D. Pan, H. Zhang, *Ind. Eng. Chem. Res.*, **2011**, 50, 9009.
- [282] D. Larcher, G. Sudant, R. Patrice, J. M. Tarascon, *Chem. Mater.*, **2003**, 15, 3543.
- [283] D. Wang, T. Xie, Y. Li, *Nano Res.*, **2009**, 2, 30.
- [284] X. Hu, J. Yu, *Adv. Funct. Mater.*, **2008**, 18, 880.
- [285] M. Casula, Y. Jun, D. Zaziski, E. Chan, A. Corrias and A. Alivisatos, *J. Am. Chem. Soc.*, **2006**, 128, 1675.
- [286] G. Zhang, M. Liu, *J. Mater. Sci.*, **1999**, 34, 3213.
- [287] C. Chen, Z. Huang, W. Yuan, J. Li, X. Cheng, R. Chi, *CrystEngComm*, **2011**, 13, 1632.
- [288] Z. Ai, K. Deng, Q. Wan, L. Zhang, S. Lee, *J. Phys. Chem. C*, **2010**, 114, 6237.
- [289] Y. Cheng, Y. S. Wang, Y. H. Zheng, Y. Qin, *J. Phys. Chem. B*, **2005**, 109, 11548.
- [290] R. L. Penn, *J. Phys. Chem. B*, **2004**, 108, 12707.
- [291] J. Park, V. Privman, E. Matijevic, *J. Phys. Chem. B*, **2001**, 105, 11630.
- [292] Y. Cheng, Y. Wang, D. Chen, F. Bao, *J. Phys. Chem. B*, **2005**, 109, 794.
- [293] R. L. Penn, J. F. Banfield, *Science*, **1998**, 281, 969.
- [294] M.-L. Li, Q.-Z. Yao, G.-T. Zhou, X.-F. Qu, C.-F. Mu, S.-Q. Fu, *CrystEngComm*, **2011**, 13, 5936.

- [295] M.-L. Li, Q.-Z. Yao, G.-T. Zhou, S.-Q. Fu, *CrystEngComm*, **2010**, 12, 3138.
- [296] K. S. W. Sing, D. H. Everett, R. A. W. Haul, L. Moscou, R. A. Pierotti, J. Rouquerol, T. Siemieniewska, *Pure Appl. Chem.*, **1985**, 57, 603.
- [297] W. H. Tao, C. H. Tsai, *Sens. Actuators, B*, **2002**, 81, 237.
- [298] M. A. Sayyadnejad, H. R. Ghaffarian and M. Saeidi, *Int. J. Environ. Sci. Tech.*, **2008**, 5, 565.
- [299] L. Li, D. L. King, *Catal. Today*, **2006**, 116, 537.
- [300] M. M. Husein, L. Patruyo, P. Pereira-Almao, N. N. Nassar, *J. Colloid Interface Sci.*, **2010**, 342, 253.
- [301] P. D. Shima, J. Philip, B. Raj, *Appl. Phys. Lett.*, **2009**, 95, 133112.
- [302] J. de Vicente, J. P. Segovia-Gutiérrez, E. Andablo-Reyes, F. Vereda, R. Hidalgo-Álvarez, *J. Chem. Phys.*, **2009**, 131, 194902.
- [303] J. Claracq, J. Sarrazin, J. Montfor, *Rheol. Acta*, **2004**, 43, 38.
- [304] A. J. W. ten Brinke, L. Bailey, H. N. W. Lekkerkerker, G. C. Maitland, *Soft Mater.*, **2007**, 3, 1145. C.
- [305] B. O'Regan, M. Grätzel, *Nature*, **1991**, 353, 737.
- [306] M. Grätzel, *J. Photochem. Photobiol. A*, **2004**, 164, 3.
- [307] C. Teng, X. C. Yang, C. Z. Yuan, C. Y. Li, R. K. Chen, H. N. Tian, S. F. Li, A. Hagfeldt, L. C. Sun, *Org. Lett.*, **2009**, 11, 5542.
- [308] S. A. Sapp, C. M. Elliott, C. Contado, S. Caramori, C. A. Bignozzi, *J. Am. Chem. Soc.*, **2002**, 124, 11215.
- [309] M. K. Wang, N. Chamberland, L. Breau, J. E. Moser, R. H. Baker, B. Marsan, S. M. Zakeeruddin, M. Grätzel, *Nat. Chem.*, **2010**, 2, 385.
- [310] T. Daeneke, T. H. Kwon, A. B. Holmes, N. W. Duffy, U. Bach, L. Spiccia, *Nat. Chem.*, **2011**, 3, 211.
- [311] C. Y. Chen, M. K. Wang, J. Y. Li, N. Pootrakulchote, L. Alibabaei, C. Ngoc-le, J. D. Decoppet, J. H. Tsai, C. Grätzel, C. G. Wu, S. M. Zakeeruddin, M. Grätzel, *ACS Nano*, **2009**, 3, 3103.
- [312] G. Boschloo, A. Hagfeldt, *Acc. Chem. Res.*, **2009**, 42, 1819.
- [313] Y. Bai, Y. M. Cao, J. Zhang, M. K. Wang, R. Z. Li, P. Wang, S. M. Zakeeruddin, M. Grätzel, *Nat. Mater.*, **2008**, 7, 626.

- [314]P. Wang, S. M. Zakeeruddin, P. Comte, I. Exnar, M. Grätzel, *J. Am. Chem. Soc.*, **2003**, 125, 1166.
- [315]M. Berginc, M. Hocevar, U. O. Krasovec, A. Hinsch, R. Sastrawan, M. Topic, *Thin Solid Film*, **2008**, 516, 4645.
- [316]L. Wang, S. B. Fang, Y. Lin, X. W. Zhou, M. Y. Li, *Chem. Comm.*, **2005**, 41, 5687.
- [317]J. H. Kim, M. S. Kang, Y. J. Kim, J. Won, N. G. Park, Y. S. Kang, *Chem. Comm.*, **2004**, 40, 1662.
- [318]T. Stergiopoulos, I. M. Arabatzis, G. Katsaros, P. Falaras, *Nano Lett.*, **2002**, 2, 1259.
- [319]J. N. D. Freitas, A. F. Nogueira, M. A. D. Paoli, *J. Mater. Chem.*, **2009**, 19, 5279.
- [320]S. S. Ray, M. Okamoto, *Prog. Polym. Sci.*, **2003**, 28, 1539.
- [321]S. R. Scully, M. T. Lloyd, R. Herrera, E. P. Giannelis, G. G. Malliaras, *Synth. Met.*, **2004**, 144, 291.
- [322]Y. Jung, Y. -H. Son, J. -K. Lee, T. X. Phuoc, Y. Soong, M. K. Chyu, *ACS Appl. Mater. Interfaces*, **2011**, 3, 3515.
- [323]M. C. Tsui, Y. L. Tuang, S. Y. Tsai, C. W. Lan, *J. Sol. Energ. Eng.*, **2011**, 133, 011002-1.
- [324]T. Inoue, S. Uchida, T. Kubo, H. Segawa, *Mater. Res. Soc. Symp. Proc.*, **2010**, 1211-R09-04.